warwick.ac.uk/lib-publications

Solid State Nuclear Magnetic Resonance on Quadrupolar Nuclei in Disordered Catalysis Based Materials

by

Thomas James Nelson Hooper

Thesis

submitted to the University of Warwick

for the degree of

Doctor of Philosophy

Department of Physics

September 2017

Contents

List of Tables

List of Figures

List of Abbreviations

wt%	percentage by weight
OAc	acetate; $[O_2C_2H_3]^-$
acac	acetylacetone; $C_5H_8O_2$
CS	Chemical Shielding
CT	Central Transition
DFT	Density Functional Theory
DOR	DOuble Rotation
EFG	Electric Field Gradient
EM	ElectroMagnetic
fcc	Face Centred Cubic
FWHM	Full-Width at Half-Maximum
GGA	Generalized Gradient Approximation
GIPAW	Gauge Including Projector Augmented Waves
iso	isotropic
IUPAC	International Union of Pure and Applied Chemistry
MAS	Magic Angle Spinning
MPMS	Magnetic Property Measurement System
MQMAS	Multiple Quantum Magic Angle Spinning
NMR	Nuclear Magnetic Resonance
PAS	Principle Axis System
P-C-T	Pressure-Composition-Temperature
PDF	Pair Distribution Function
PGAA	Prompt Gamma neutron Activation Analysis
ppm	Parts Per Million
PVP	polyvinylpyrrolidone
RF	Radio Frequency
SATRAS	SAtellite TRAnsition Spectroscopy
SEM	Scanning Electron Microscopy

SNR	Signal to Noise Ratio
ST	Satellite Transition
SQUID	Superconducting QUantum Interference Device
TEM	Transmission Electron Microscopy
TGA	Thermogravimetric Analysis
THF	tetrahydrofuran; $(CH_2)_4O$
QIS	Quadrupole Interaction Shift
VOCS	Variable Offset Cumulative Spectroscopy
XRD	X-Ray Diffraction
YAG	Yttrium Aluminium Garnet

Acknowledgements

Finally, I recognise that this research would not have been possible without financial backing from Johnson Matthey, the Engineering and Physical Science Research Council (EPRSC) and the University of Warwick.

Thomas J. N. Hooper

Declarations

I hereby declare that this thesis entitled **Solid State Nuclear Magnetic Resonance on Quadrupolar Nuclei in Disordered Catalysis Based Materials** is an original work and has not been submitted for a degree, or any other qualification, at any other university.

Results from other authors are referenced in the usual manner throughout the text. All collaborative results are indicated in the text along with the nature and extent of the collaborator's contribution. A summary of the contributions is given here:

- Dr Gregory Rees (University of Warwick) undertook the GIPAW-DFT calculations and Dr Dean Keeble (Diamond Light Source) performed the PDF XRD analysis in Chapter 4.4.
- Dr Ieuan Ellis (University of Oxford) synthesized the boron and lithium doped palladium nanoparticles examined in Chapter 4.7
- Drs Kirill Okhotnikov and Thibault Charpentier (CEA Saclay) undertook the *supercell* structure generation and GIPAW-DFT calculations in Chapter 5.
- Dr Hanna Lührs (Universität Bremen) synthesized the mullite powders in Chapter 5.
- Dr Kristin Hoffman (Universität Bremen) synthesized the aluminoborate powders in Chapter 6.

The rest of the material contained within this thesis is original research performed by the author.

Abstract

The behaviour of a catalyst is intrinsically linked to its structure and, therefore, accurate structural refinements are desired to tune their overall function. Higher functional demands on catalysts systems, require more complex disordered materials which are inherently difficult to characterise with conventional analytical techniques. Solid state NMR is an excellent probe of local order and, hence, is utilised in this thesis for the structural determination of several catalytic related materials.

The first direct ^{105}Pd solid state NMR measurements of diamagnetic (K_2PdCl_6, $(NH_4)_2PdCl_6$ and K_2PdBr_6) complexes is reported, thereby introducing an effective ^{105}Pd chemical shift ranges with respect to the newly proposed ^{105}Pd chemical shift reference (0.33 M $H_2PdCl_{6(aq)}$). The enormous ^{105}Pd quadrupolar moment, makes the interaction very sensitive to small structural distortions as demonstrated by the measurable quadrupolar parameters for the three complexes, despite the high symmetry octahedral Pd coordination. The detected deviation from a cubic symmetry, was corroborated by XRD PDF analysis. The ^{105}Pd quadrupolar parameters are shown to be more sensitive to minute disorder than conventional XRD and other quadrupolar nuclei NMR. Ambient temperature ^{105}Pd NMR observations of Pd metal determined the Knight shift as $K = -3.205 \pm 0.006$ %, where variations in the ^{105}Pd Knight shift allowed for detection of defects in the cubic metal structure and for differentiation of Pd nanoparticle sizes. The developed ^{105}Pd NMR methodology was then applied in a multi-technique structural investigation of doped Pd catalysts, that confirmed the interstitial location of the dopants.

The use of the newly developed structure-generation software, *supercell*, in combination with GIPAW-DFT calculations and solid state NMR, is shown to be a thorough tool for structural determination of disordered materials. The methodology is applied to two phases of the aluminosilicate mullite (3:2 mullite and 2:1 mullite), and provides complete assignment of the ^{17}O, ^{27}Al and ^{29}Si NMR spectra. The distribution of AlO_4/SiO_4 sites in the mullite structure is shown to be random, proving the presence of SiO_4 moieties in the tri-tetrahedral (T_3O) environments. The observation of said moieties directly contradicts Loewenstein's avoidance principle. Additionally, a quasi-tetrahedral site with an additional long bond (($(Al/Si)O_{4+1}$) is discovered and a vacancy adjacent three-coordinated Al site ($AlO_3\square$) is proposed. The findings from this investigation are then applied to the ^{27}Al MQMAS study of boron doped mullites, providing additional evidence for the $AlO_3\square$ motif.

A thorough ^{11}B and ^{27}Al solid state NMR investigation was undertaken on three series of aluminium borate phases (A9B2, A2B and metastable $Al_{6-x}B_xO_9$ (where $1 \leq x \leq 3$)) with varying Al/B ratios. A solid solution of AlO_4 and BO_4 tetrahedra was discovered in all three phases (to varying extents), justifying the conflicting compositional/structural reports present in the literature. Differences in the crystallinity of commercially available, sol-gel synthesized, and solid state synthesised A9B2 samples were documented. The solid state NMR study of the disordered phases, A2B and metastable $Al_{6-x}B_xO_9$, utilised multiple fields and MQMAS measurements to constrain the simulation of the 1D spectra, which allowed for complete assignment of the structure and corrected previous erroneous reports. An AlO_{4+1} site, analogous to the discovered mullite environment, is found in both disordered phases.

1

Solid State NMR Theory

1.1. Spin Angular Momentum

Fundamental particles possess the intrinsic property of spin angular momentum (S). Spin angular momentum is quantised; particles with spin S have $2S + 1$ degenerate spin sublevels. Therefore, protons and neutrons with spin $S = {}^1/_2$ have 2 spin sublevels: spin "up" $m = +{}^1/_2$ and spin "down" $m = -{}^1/_2$. The nuclear spin quantum number (I) is the sum of the spins of its constituent nucleons. Nucleons can be aligned in a parallel ($\pm{}^1/_2$, $\pm{}^1/_2$) or antiparallel ($\pm{}^1/_2$, $\mp{}^1/_2$) configuration and the nuclear spin of an isotope is decided by the ground state configuration of its nucleons' spins. Therefore, the nuclear spin quantum number, I, is either equal to integer or half-integer values (0, ${}^1/_2$, 1...). The spin angular momentum of a nucleus, I, produces a magnetic moment, μ, defined by

$$\hat{\mu} = \gamma\hbar\hat{I} \qquad 1.1$$

where γ is the gyromagnetic ratio, a characteristic parameter of each nucleus.[1]

1.2. The Zeeman Interaction

The degeneracy of a nuclear state is broken in an applied magnetic field producing $2I + 1$ energy levels, due to the different magnetic moment of each spin sublevel m (as shown in Figure 1.1). If the applied static magnetic field is defined in the z-axis giving $B = (0, 0, B_0)$ then the Zeeman Hamiltonian is given by

$$\hat{H}_Z = -\hat{\mu} \cdot \hat{B} = -\hat{\mu}_z B_0 = -\gamma\hbar\hat{I}_z B_0. \qquad 1.2$$

The energy difference created by the Zeeman "splitting" is then described by the Larmor frequency ω_0:

$$\omega_0 = -\gamma B_0. \qquad 1.3$$

Nuclear magnetic resonance (NMR) spectroscopy excites the transitions between the splittings using electromagnetic (EM) radiation and then detects the frequency of the
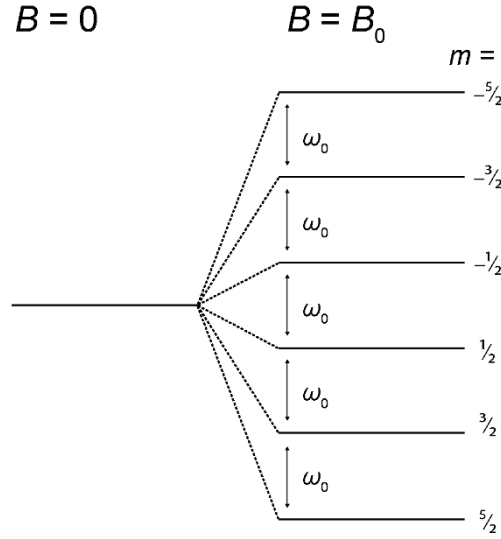
Figure 1.1 Diagram representing the Zeeman splitting of the spin states m of an $I = {}^5/_2$ nucleus.

transition on its return to equilibrium. Therefore, any isotope with a nuclear spin quantum number $I > 0$ is NMR active. The detected frequency, or resonance frequency, is then displayed as a peak on a frequency spectrum. The distinct Larmor frequency of each isotope, due to its characteristic gyromagnetic ratio γ, allows it to be distinguished by NMR.[1]

1.3. Internal Interactions

If the Zeeman interaction was the only phenomena affecting the nuclear spins, then NMR would not provide any information about the nuclear environment. In fact, there are multiple interactions which are all contained in the nuclear spin Hamiltonian:

$$\widehat{H} = \widehat{H}_Z + \widehat{H}_{CS} + \widehat{H}_J + \widehat{H}_D + \widehat{H}_Q + \widehat{H}_K + \cdots. \qquad 1.4$$

Each interaction alters the frequency of the transitions between the spin sublevels and, therefore, provides additional information to be detected by NMR. The interactions included above are the Zeeman interaction ($\widehat{H}_Z$; Chapter 1.2), the chemical shielding interaction ($\widehat{H}_{CS}$; Chapter 1.3.2), the dipolar interaction ($\widehat{H}_D$; Chapter 1.3.3), the quadrupolar interaction ($\widehat{H}_Q$; Chapter 1.3.4) and the Knight shift interaction ($\widehat{H}_K$; Chapter 1.3.5). In solids, the strength of the interactions generally follows the hierarchy of

$$\widehat{H}_Z > \widehat{H}_Q > \widehat{H}_K > \widehat{H}_{CS} > \widehat{H}_D > \widehat{H}_J \qquad 1.5$$

Other interactions, including the weak *J*-coupling interaction ($\hat{H}_J$), have not been discussed in this thesis due their limited relevance to the results achieved.[2] The relative strengths of the internal interactions, compared to the Zeeman interaction, allows them to be treated as perturbations to the Zeeman Hamiltonian.

1.3.1. Coordination Frames

Before the various NMR interactions are described, it is helpful to define the coordination frames used. Transformations between coordination frames are described by the Euler angles α, β, and γ as shown in Figure 1.2.
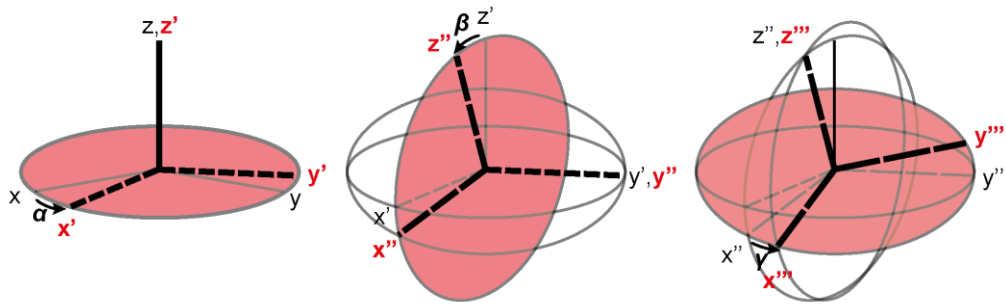
Figure 1.2 The definitions of the Euler angles that define coordination frame transformations.
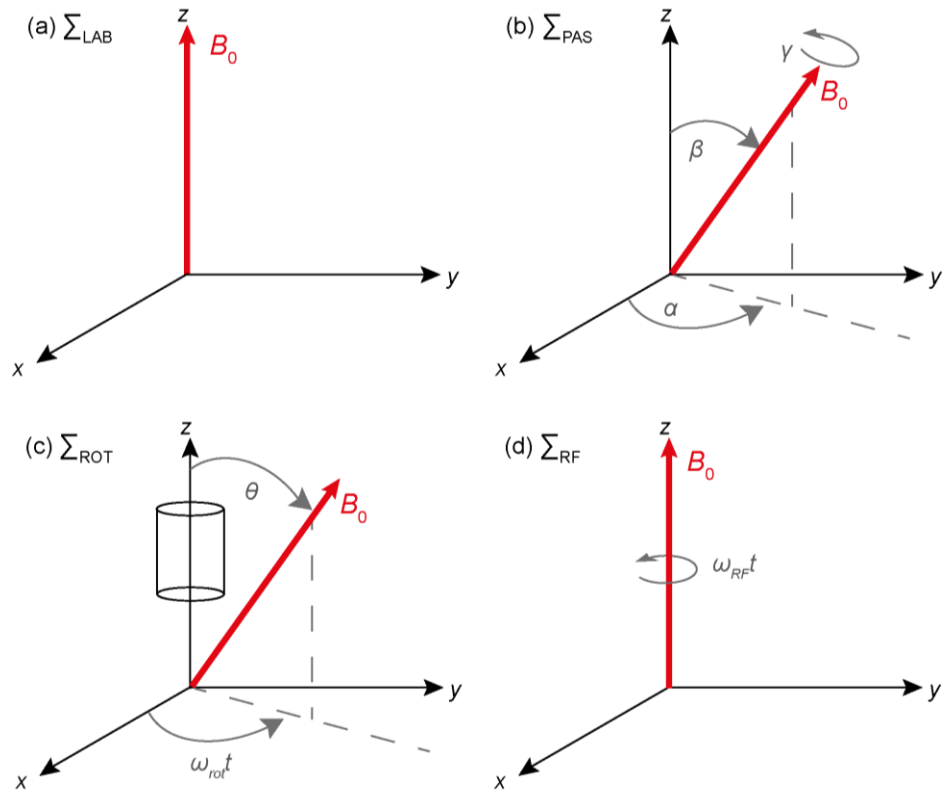
Figure 1.3 Diagrams representing (a) the laboratory coordination frame Σ^{LAB}, (b) the principal axis system coordination frame Σ^{PAS}, (c) the rotor coordination frame Σ^{ROT}, and (d) the RF coordination frame Σ^{RF}.

The following coordination frames are discussed in this thesis: the laboratory coordination frame Σ^{LAB} (Figure 1.3(a)) describes the B_0 vector in the z-direction; the principal axis system coordination frame Σ^{PAS} (Figure 1.3(b)) describes the frame in which the interaction tensor is diagonalized with Euler angles α, β, and γ detailing the direction of the B_0 vector; the rotor coordination frame Σ^{ROT} (Figure 1.3(c)) describes a rotation about the z-axis at a frequency of ω_{rot} with the angle θ detailing the direction of the B_0 vector; and the RF coordination frame Σ^{RF} (Figure 1.3(d)) describes a rotation about the z-axis at a frequency of ω_{RF} with the B_0 vector in the z-direction.

1.3.2. Chemical Shielding

Due to the magnetic properties of electrons, the resonance frequency of the nucleus will be affected by its local electronic environment. In diamagnetic materials, this effect is called chemical shielding, whereas in paramagnetic materials it is the paramagnetic shift and in metals it is the Knight shift (see Chapter 1.3.5).

Chemical shielding occurs because an applied magnetic field will induce currents in the electron clouds around a nucleus, which in turn will induce a small magnetic field. The nuclear spins sense the sum of the applied external field and the internal induced field. The direction of the induced field varies with the orientation of the electronic environment with respect to B_0. Therefore, the chemical shielding is described by a second rank tensor, $\boldsymbol{\sigma}$. In the principle axis system (Σ^{PAS}), $\boldsymbol{\sigma}$ is given by[3]

$$\boldsymbol{\sigma} = \begin{bmatrix} \sigma_{XX} & 0 & 0 \\ 0 & \sigma_{YY} & 0 \\ 0 & 0 & \sigma_{ZZ} \end{bmatrix} \qquad 1.6$$

where

$$|\sigma_{ZZ} - \sigma_{iso}| \geq |\sigma_{XX} - \sigma_{iso}| \geq |\sigma_{YY} - \sigma_{iso}| \qquad 1.7$$

and

$$\sigma_{iso} = \frac{\sigma_{XX} + \sigma_{YY} + \sigma_{ZZ}}{3}. \qquad 1.8$$

The chemical shielding Hamiltonian is then given by

$$\hat{H}_{\text{CS}} = \gamma \hbar \hat{I} \cdot \boldsymbol{\sigma} \cdot \hat{B} = \gamma \hbar B_0 \hat{I}_z \cdot \sigma_{ZZ} =$$

$$\gamma \hbar B_0 \hat{I}_Z \left(\sigma_{iso} + \sigma_{aniso} \left[\frac{(3\cos^2 \beta - 1) + \eta_{CS} \sin^2 \beta \cos 2\alpha}{2} \right] \right) \qquad 1.9$$

when transformed into the lab frame Σ^{LAB}. The σ_{aniso} term is given as

$$\sigma_{aniso} = \sigma_{ZZ} - \sigma_{iso} \qquad 1.10$$

and the η_{CS} term is defined as

$$\eta_{CS} = \frac{\sigma_{XX} - \sigma_{YY}}{\sigma_{aniso}}. \qquad 1.11$$

The derivation of the chemical shielding Hamiltonian summarised here is given in full by Mackenzie and Smith.[2] The chemical shielding Hamiltonian provides an additional shift to the spin energy levels, m, alongside the Zeeman interaction. Chemical shielding alters the resonance frequency between the spin energy levels by the frequency

$$\omega_{m-1,m} = \langle m-1|\hat{H}_{CS}|m-1\rangle - \langle m|\hat{H}_{CS}|m\rangle =$$

$$\gamma B_0 \left(\sigma_{iso} + \sigma_{aniso} \left[\frac{(3\cos^2 \beta - 1) + \eta_{CS} \sin^2 \beta \cos 2\alpha}{2} \right] \right). \qquad 1.12$$

From Equation 1.12, the isotropic chemical shielding is given as σ_{iso}, whereas the orientation dependent component is described by the reduced shielding anisotropy σ_{aniso} and the shielding asymmetry η_{CS}.[2-3] The use of these terms to describe the chemical shielding interaction follows the Haeberlen convention rather than the two other conventions in the literature: the Mehring convention and the Maryland convention.[4]

In the majority of solid state NMR experiments, the sample is in powder form (*i.e.* containing an isotropic distribution of crystallites). Thus, the Σ^{PAS} of the chemical shielding tensor is randomly orientated with respect to B_0 for each crystallite. Additionally, the chemical shielding frequency shifts (Equation 1.12) are dependent on the Euler angles α and β describing the orientation of B_0 in Σ^{PAS}. Therefore, the isotropic distribution of crystallites produces a distribution of resonance frequencies. The population distribution over the given frequency range, forms an NMR lineshape called a powder pattern. The chemical shift anisotropy (CSA) creates distinct powder patterns with a shape dependent on σ_{aniso} and η_{CS} $(0 < \eta_{\mathrm{CS}} < 1)$.[1] Examples of such powder patterns have been simulated with *dmfit*[5] and are given in Figure 1.4(a).
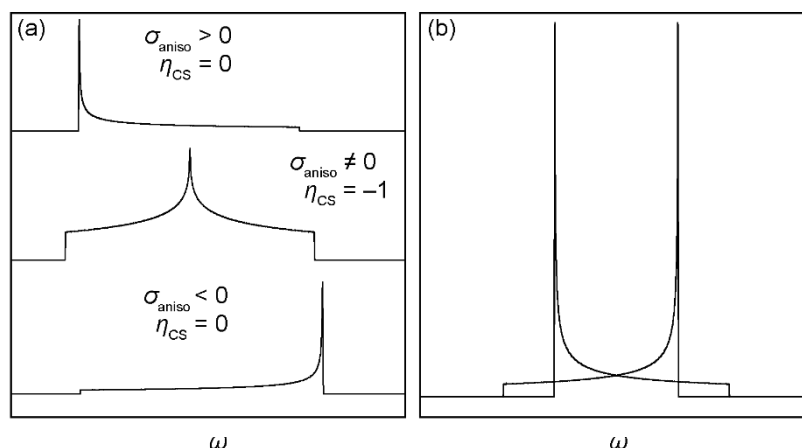
Figure 1.4 Representative powder patterns produced by the frequency shifts of: (a) CSA with varying shielding anisotropy σ_{aniso} and asymmetry η_{CS} values; and (b) Dipolar coupling (Pake powder pattern). The powder patterns were simulated with *dmfit*.

The centre of gravity of the chemical shielding frequencies (δ_{CSiso}) is given by the isotropic component. The combination of the Zeeman interaction and isotropic chemical shielding component produces a resonance frequency of

$$\omega = -\gamma B_0 (1 - \sigma_{iso}).$$
1. 13

The dependence of this frequency on the chemical shielding tensor, and hence the electronic environment of the nucleus, is what makes NMR a powerful analytical technique. The electronic environment of a nucleus varies from molecule to molecule due to its chemical environment and bonding. The chemical shielding adjusted frequency can therefore differentiate between nuclei in varying chemical environments.

As shown in Equation 1.13, the resonance frequency is dependent on the applied magnetic field B_0. To remove this factor, and to standardise NMR measurements, the resonance frequency is measured as the difference from a reference frequency, ω_{ref}, and is then normalised with respect to ω_{ref}, giving

$$\delta - \delta_{ref} = \frac{\omega - \omega_{ref}}{\omega_{ref}}.$$
1. 14

The result, δ, is called the chemical shift. The known frequency ω_{ref} is usually close to the Larmor frequency and provided by a chemical standard. The chemical shift of the reference, δ_{ref}, is typically chosen to be zero. The change in frequency due to the chemical shielding is small in comparison to the Larmor frequency so the chemical shift, δ, is multiplied by 10^6 and quoted in units of parts per million (ppm).[2-3] From Equations 1.13 and 1.14 the chemical shift can be related to the chemical shielding by[2]

$$\delta - \delta_{ref} = \frac{\sigma_{ref} - \sigma_{iso}}{1 - \sigma_{ref}}.$$ (1.15)

1.3.3. The Dipolar Interaction

The dipolar interaction is the through space coupling between the magnetic dipoles of two adjacent nuclear spins. The Hamiltonian of the dipolar interaction combines the classical formula for the energy of two magnetic dipoles with the nuclear spin magnetic moment (Equation 1.1). Once the dipolar Hamiltonian is transformed from the Σ^{PAS} to the Σ^{LAB} it can be described by

$$\hat{H}_D = -\frac{\mu_0}{4\pi} \frac{\hbar \gamma_I \gamma_S}{r^3} \left(\hat{I} \cdot \hat{S} - \frac{3(\hat{I} \cdot \hat{r})(\hat{I} \cdot \hat{r})}{r^2} \right) =$$

$$-\frac{\mu_0}{4\pi} \frac{\hbar \gamma_I \gamma_S}{r^3} f(\hat{I}_z, \hat{S}_z) \frac{(3\cos^2 \beta - 1)}{2}$$ (1.16)

where β is the angle between the vector joining the two spins and B_0. The dipolar coupling is a through space interaction dependent on the distance r between the two nuclear spins $\hat{I}$ and $\hat{S}$, as well as their respective gyromagnetic ratios γ_I and γ_S. The derivation of the dipolar Hamiltonian is summarised above and is given in full by Levitt.[1]

The resonance frequency of both coupled spins is altered by the dipolar interaction, which, like the CSA, is orientation dependent. In an isolated spin couple, the distribution of the orientation vector between the spins results in a pair of characteristic powder patterns that are superimposed, forming a Pake doublet lineshape (Figure 1.4(b)). However, in more complex spin systems the resultant powder pattern is broadened to a Gaussian/Lorentzian lineshape.[6]

1.3.4. The Quadrupolar Interaction

Nuclei with spin $I > {}^1/_2$ have a non-spherical charge distribution and, therefore, an electric quadrupole moment. The coupling between a nucleus' quadrupole moment and the internal inhomogeneous electric fields in its environment is the quadrupolar interaction. The electric field gradient (EFG) is described by V, a second-rank diagonal tensor in the principle axis system (Σ^{PAS}) given by

$$V = \begin{bmatrix} V_{XX} & 0 & 0 \\ 0 & V_{YY} & 0 \\ 0 & 0 & V_{ZZ} \end{bmatrix}$$ (1.17)

where $V_{XX} + V_{YY} + V_{ZZ} = 0$ and $|V_{XX}| \geq |V_{YY}| \geq |V_{ZZ}|$. Therefore, the EFG can be described by the two independent parameters:

$$eq = V_{ZZ} \qquad\qquad 1.18$$

and

$$\eta_Q = \frac{V_{XX} - V_{YY}}{V_{ZZ}}. \qquad\qquad 1.19$$

In axially symmetric structures the quadrupolar asymmetry parameter $\eta_Q = 0$, whereas in completely symmetrical structures the EFG is negligible and, hence, $eq = 0$ as well.

This EFG tensor leads to the expression of the Hamiltonian in the Σ^{PAS} as

$$\widehat{H}_Q = \frac{eQ}{2I(2I-1)\hbar} \hat{I} \cdot \boldsymbol{V} \cdot \hat{I} =$$
$$\frac{e^2 qQ}{4I(2I-1)\hbar} \left[3\hat{I}_z^2 - I(I+1) + \eta\left(\hat{I}_x^2 - \hat{I}_y^2\right) \right]. \qquad\qquad 1.20$$

By assuming the system is in a high field regime, $\hat{H}_Q$ can be treated as first ($\hat{H}_Q^{[1]}$) and second ($\hat{H}_Q^{[2]}$) order perturbations of the Zeeman interaction. The derivation of $\hat{H}_Q^{[1]}$ and $\hat{H}_Q^{[2]}$ from the expression for $\hat{H}_Q$ in the Σ^{PAS} involves a coordinate frame transformation to the Σ^{LAB} using the spherical components of the tensor $\boldsymbol{V}$. This derivation is described in thorough detail in the literature. The quadrupolar theory in this chapter is taken from the report by Man which should be read for further embellishment.[7] The first and second order quadrupolar Hamiltonians are given by

$$\widehat{H}_Q^{[1]} = \frac{e^2 qQ}{4I(2I-1)\hbar} \left[3\hat{I}_z^2 - I(I+1) \right] \left[\frac{(3\cos^2\beta - 1) + \eta_Q \sin^2\beta \cos 2\alpha}{2} \right] \qquad 1.21$$

and

$$\widehat{H}_Q^{[2]} = -\frac{1}{\omega_0} \left[\frac{eQ}{4I(2I-1)\hbar} \right]^2 \left\{ \begin{matrix} f(\alpha,\beta,\eta_Q)\hat{I}_z\left[4I(I+1) - 8\hat{I}_z^2 - 1\right] + \\ 2f'(\alpha,\beta,\eta_Q)\hat{I}_z\left[2I(I+1) - 2\hat{I}_z^2 - 1\right] \end{matrix} \right\}, \qquad 1.22$$

where

$$\hat{H}_Z \qquad\qquad \hat{H}_Q^{[1]} \qquad\qquad \hat{H}_Q^{[2]}$$

$\omega_0 \qquad +\omega^{[1]}_{-5/2,-3/2} \qquad +\omega^{[2]}_{-5/2,-3/2}$

$\omega_0 \qquad +\omega^{[1]}_{-3/2,-1/2} \qquad +\omega^{[2]}_{-3/2,-1/2}$

$\omega_0 \qquad +\omega^{[1]}_{-1/2,1/2} \qquad +\omega^{[2]}_{-1/2,1/2}$

$\omega_0 \qquad +\omega^{[1]}_{1/2,3/2} \qquad +\omega^{[2]}_{1/2,3/2}$

$\omega_0 \qquad +\omega^{[1]}_{3/2,5/2} \qquad +\omega^{[2]}_{3/2,5/2}$
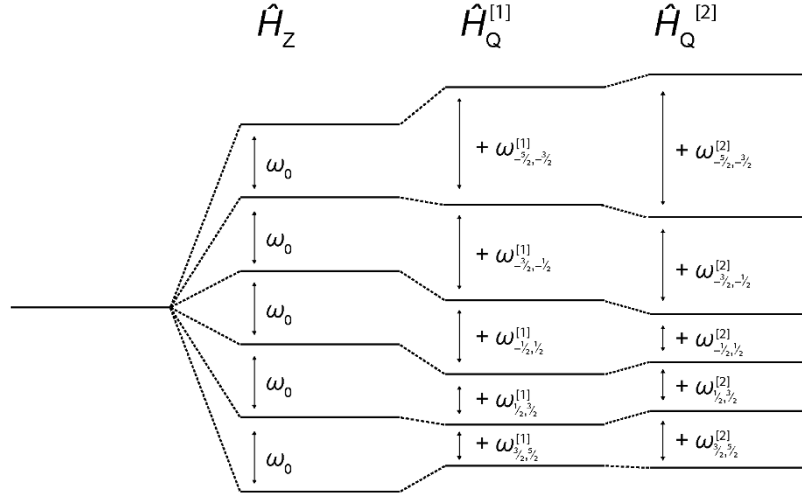
Figure 1.5 Diagram representing the first and second order quadrupolar perturbations of the Zeeman splitting of the spin states of an arbitrary $I = {}^5\!/_2$ nucleus.

$$f(\alpha,\beta,\eta) = -\frac{3}{2}e^2q^2 \left[\begin{array}{c} \left(-\frac{1}{3}\eta_Q{}^2 \cos^2 2\alpha + 2\eta_Q \cos 2\alpha - 3\right)\cos^4 \beta \\[2mm] +\left(\frac{2}{3}\eta_Q{}^2 \cos^2 2\alpha - 2\eta_Q \cos 2\alpha - \frac{1}{3}\eta_Q{}^2 + 3\right)\cos^2 \beta \\[2mm] +\frac{1}{3}\eta_Q{}^2(1-\cos^2 2\alpha) \end{array} \right] \qquad 1.23$$

and

$$f'(\alpha,\beta,\eta) = \frac{3}{2}e^2q^2 \left[\begin{array}{c} \left(\frac{1}{24}\eta_Q{}^2 \cos^2 2\alpha - \frac{1}{4}\eta_Q \cos 2\alpha + \frac{3}{8}\right)\cos^4 \beta \\[2mm] +\left(-\frac{1}{12}\eta_Q{}^2 \cos^2 2\alpha + \frac{1}{6}\eta_Q{}^2 - \frac{3}{4}\right)\cos^2 \beta \\[2mm] +\left(\frac{1}{24}\eta_Q{}^2 \cos^2 2\alpha + \frac{1}{4}\eta_Q \cos 2\alpha + \frac{3}{8}\right) \end{array} \right]. \qquad 1.24$$

The first and second order quadrupolar interactions shift the spin energy levels m (see Figure 1.5), resulting in a change in the resonance frequency. The corresponding frequency shifts for single transitions are given by

$$\omega^{[1]}_{m-1,m} = \langle m-1|\hat{H}_Q^{[1]}|m-1\rangle - \langle m|\hat{H}_Q^{[1]}|m\rangle =$$

$$\frac{3e^2qQ}{4I(2I-1)\hbar}\left[\frac{(3\cos^2 \beta - 1) + \eta \sin^2 \beta \cos 2\alpha}{2}\right](1-2m) \qquad 1.25$$

for the first order interaction and

$$\omega^{[2]}_{m-1,m} = \langle m-1|\hat{H}_Q^{[2]}|m-1\rangle - \langle m|\hat{H}_Q^{[2]}|m\rangle =$$

$$-\frac{1}{\omega_0}\left[\frac{eQ}{4I(2I-1)\hbar}\right]^2 \begin{pmatrix} f(\alpha,\beta,\eta_Q)[24m(m-1)-4I(I+1)+9] + \\ f'(\alpha,\beta,\eta_Q)[12m(m-1)-4I(I+1)+6] \end{pmatrix} \qquad 1.26$$

for the second order interaction. The quadrupole coupling constant, C_Q, and the quadrupolar frequency, ω_Q, are often used for simplicity where

$$C_Q = \frac{e^2qQ}{\hbar} \qquad 1.27$$

and

$$\omega_Q = \frac{3C_Q}{4I(2I-1)}. \qquad 1.28$$

The first order interaction creates $2I+1$ energy levels with $2I$ distinct transitions resulting in a multiplet in the NMR spectrum from the central transition (CT) ($m = {}^1/_2$) and the satellite transitions (STs). Similarly to the CSA and the dipolar interaction, the first order transition frequencies (Equation 1.25) are dependent on the Euler angles α and β, describing the orientation of Σ^{PAS}. Therefore, the first order quadrupole interaction produces a powder pattern. The number of peaks in the first order quadrupolar powder pattern is dependent on the nuclear spin I. The shape of the pattern depends on the asymmetry parameter η_Q, as demonstrated by the examples simulated in Figure 1.6(a).

The central transition ($m = {}^1/_2$) is unaffected by the first order shift ($\omega^{[1]}_{-1/2,1/2} = 0$; see Equation 1.25), whereas the second order quadrupolar interaction alters all the transitions. Due to the lack of a first order shift, most quadrupolar NMR focuses solely on the central transition. Additionally, the wide frequency range of the first order quadrupolar powder pattern, for moderate C_Q values, makes it difficult to observe in completeness. The second order quadrupole shift at the CT is given by $m = {}^1/_2$ in Equation 1.26:

$$\omega^{[2]}_{-\frac{1}{2},\frac{1}{2}} = -\frac{1}{6\omega_0}\left[\frac{3C_Q}{2I(2I-1)}\right]^2 \left[I(I+1)-\frac{3}{4}\right]\begin{bmatrix} A(\alpha,\eta_Q)\cos^4\beta \\ +B(\alpha,\eta_Q)\cos^2\beta \\ +C(\alpha,\eta_Q) \end{bmatrix} \qquad 1.29$$

$$A(\alpha,\eta) = -\frac{27}{8}+\frac{9}{4}\eta_Q\cos 2\alpha - \frac{3}{8}\eta_Q{}^2\cos^2 2\alpha$$

$$B(\alpha,\eta) = \frac{30}{8}-\frac{1}{2}\eta_Q{}^2 - 2\eta_Q\cos 2\alpha + \frac{3}{4}\eta_Q{}^2\cos^2 2\alpha$$

$$C(\alpha,\eta) = -\frac{3}{8}+\frac{1}{3}\eta_Q{}^2 - \frac{1}{4}\eta_Q\cos 2\alpha - \frac{3}{8}\eta_Q{}^2\cos^2 2\alpha.$$
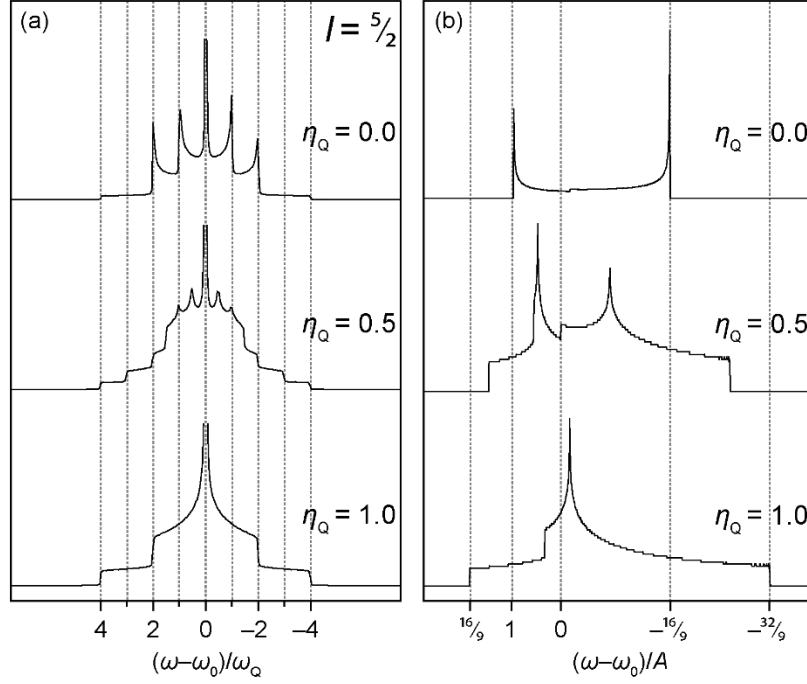
Figure 1.6 Powder patterns produced by (a) the first order quadrupolar frequency shift for $I = ^5/_2$ (where the intensity of the CT has been truncated) and (b) the second order frequency shift at the CT for varying values of η_Q. The powder patterns were simulated with *dmfit* and the parameter A is equal to

$$\frac{\omega_Q{}^2}{4\omega_0}\left[I(I+1) - \frac{3}{4}\right].$$

The second order shift at the central transition is also orientation dependent and therefore results in powder patterns as demonstrated by Figure 1.6(b). The breadth of the CT, determined from Equation 1.29, is given by[8]

$$\Delta\left(\omega_{-\frac{1}{2},\frac{1}{2}}^{[2]}\right) = \frac{25 + 22\eta_Q + \eta_Q{}^2}{144}\left(\frac{\omega_Q{}^2}{\omega_0}\right)\left[I(I+1) - \frac{3}{4}\right]. \qquad 1.30$$

1.3.5. The Knight Shift

In a conducting solid the nucleus is not only affected by the magnetism of electrons in its bonds (chemical shielding; Chapter 1.3.2), but also by the magnetism of the delocalised conduction electrons. The Knight shift is the relative shift, K, in a metallic environment compared to an equivalent non-metallic surrounding, first discovered by Knight.[9] Due to their similarities, the Knight shift can be described analogously to chemical shielding. The Knight shift tensor $\boldsymbol{K}$ in the principal axis system Σ^{PAS} is given by

$$K = \begin{bmatrix} K_{XX} & 0 & 0 \\ 0 & K_{YY} & 0 \\ 0 & 0 & K_{ZZ} \end{bmatrix}. \tag{1.31}$$

The frequency shift in Σ^{LAB} is then given by

$$\omega = -\gamma B_0 \left(K_{iso} + K_{aniso} \left[\frac{(3\cos^2\beta - 1) + \eta_K \sin^2\beta \cos 2\alpha}{2} \right] \right) \tag{1.32}$$

where

$$K_{iso} = \frac{K_{XX} + K_{YY} + K_{ZZ}}{3}, \tag{1.33}$$

$$K_{aniso} = K_{ZZ} - K_{iso}, \tag{1.34}$$

and

$$\eta_K = \frac{K_{XX} - K_{YY}}{K_{aniso}} \tag{1.35}$$

following the Haeberlen convention. Most metals are highly symmetrical and in a cubic environment $K_X = K_Y = K_Z$ leaving only the isotropic Knight shift K_{iso}.[2]

The total Knight shift consists of multiple components where[10]

$$K = K_p + K_{cp} + K_{orb} + \sigma. \tag{1.36}$$

The contact interaction contribution K_p results from the Pauli paramagnetic spin susceptibility χ_p of the conduction electrons. The conduction electrons occupy the electronic states from the lowest energy to the Fermi energy as spin "up" and spin "down" pairs as per the Pauli exclusion principle. In an applied magnetic field, spins aligned with the field become energetically favourable, resulting in an imbalance in the population of the electron spin states. Analogously to the Zeeman interaction, the difference in spin state population results in a net magnetisation, which is felt by the nucleus. The associated susceptibility of this magnetisation is the Pauli paramagnetic spin susceptibility χ_p. The K_p contribution can then be given as

$$K_p = \frac{8\pi}{3} V_0 P_F \chi_p \tag{1.37}$$

where V_0 is the volume per atom and P_F is the average value of the electron probability density at the nucleus. Due to the dependence of K_p on the electron density at the nucleus this effect is dominated by s-electrons.

The direct interaction of *d*-electron paramagnetism with the nucleus is minimal, but it has an indirect effect called core polarisation. The *d*-electron field induces polarisation of the *s*-electrons in closed shells, or paired *s*-electrons in conduction bands below the Fermi surface. The polarisation in turn produces a field which interacts with the nucleus. The core polarisation field can be comparable to the direct *s*-electron contact interaction and is represented by K_{cp}.

In addition to the above interactions from the Pauli paramagnetism of the conduction electrons, is a contribution from the orbital magnetic moment of the conduction electrons induced by an applied magnetic field. The orbital contribution K_{orb} is a second order effect, which results from the admixture of occupied and unoccupied orbitals in the same band due to the influence of the applied magnetic field. The mixing of these states results in a magnetisation analogous to the Van Vleck paramagnetism, which is defined by the susceptibility χ_v.[11]

The total Knight shift also includes a contribution from the chemical shielding (σ), as shown in Equation 1.36. The K_p component is predominant in light metals, whereas K_{cp} is a large contribution in heavier metals. Generally, the K_{orb} contribution is small, but it can be significant in transition metals. Both K_p and K_{orb} are always positive, whereas K_{cp} is negative. Like the chemical shift, the Knight shift is measured against a reference frequency:

$$K = \frac{\omega_{metal} - \omega_{ref}}{\omega_{ref}}.$$

1.38

The Knight shift can be expressed in ppm, however, due to the large frequency shifts produced by the Knight shift, it is often expressed as a percentage difference instead. For a full description of metallic NMR and the Knight shift, see the review by van der Klink and Brom.[12]

1.4. Magic Angle Spinning

Magic angle spinning (MAS) is a fundamental technique for enhancing spectral resolution in solid state NMR, which involves the mechanical spinning of powder samples at a specific angle to B_0. NMR resonances in liquid are significantly narrower than in solids due to rapid thermal tumbling. This motion is generally of a frequency much greater than that of the internal interactions and, therefore, it averages any angular dependencies to zero, leaving

only the isotropic parts of the interactions. Hence, the NMR lineshapes of liquid samples do not present as powder patterns (see Chapter 1.3). The MAS technique attempts to emulate the removal of the anisotropic components of the interactions by motional liquid environments, through rapid rotation of the solid samples. To derive the Hamiltonians describing each interaction under MAS they must be rotated from the Σ^{PAS} to the rotating coordinate frame Σ^{ROT} before converting to Σ^{LAB} (Figure 1.3).

The coordination frame transformation and its effect on the interaction Hamiltonian is discussed in full detail by Mackenzie and Smith.[2] In brief, Hamiltonians can be split into time-dependent and time-independent parts. The time-dependent component is averaged by the fast rotation, whereas the time-independent component is a modified version of the static Hamiltonian. Many interaction Hamiltonians can be described by a rank two tensor. In this case, the anisotropic component acquires a modulation factor equal to the second order Legendre polynomial $P_2(\cos\theta)$ given by

$$P_2(\cos\theta) = \frac{1}{2}(3\cos^2\theta - 1),$$

1.39

where θ is the angle between B_0 and the rotor axis. Hence, when the rotor axis is set at the "magic angle" of $\theta = 54.74°$, the anisotropic component of the Hamiltonian is reduced to zero ($P_2(\cos\theta) = 0$). Sufficiently high frequency MAS can, therefore, completely remove the broadening created by the anisotropic powder patterns of interactions which can be described by second rank tensors. Hence, both the CSA and dipolar broadening can be removed by MAS.

The complete removal of the anisotropic Hamiltonian components only occurs when the spinning frequency ω_r is greater than the static linewidth of the broadened resonance. The physical limitations on rotor spinning speeds mean this is often not the case. If ω_r is too small, then the time-dependent Hamiltonian component is not completely averaged. The time modulated Hamiltonian produces satellite components at integer values of ω_r from the isotropic shift. The satellite resonances in the NMR spectra are called spinning sidebands. As ω_r increases the spinning sidebands are shifted further from the isotropic shift and become weaker. A full description of the mathematics behind the spinning sidebands is given by Duer.[3]

1.4.1. Quadrupolar Interaction under MAS

The quadrupolar interaction has a more complex behaviour under MAS.[7] As shown in Equation 1.25, the first order quadrupolar frequency shift can be given by a second rank tensor, so upon transformation from the Σ^{ROT} coordination frame it is modulated by $^1/_2 (3\cos\theta - 1)$:

$$\omega_{m-1,m}^{[1]ROT} = \frac{1}{2}(1-2m)\omega_Q \left[\frac{(3\cos^2\beta - 1) + \eta_Q \sin^2\beta \cos 2\alpha}{2} \right] (3\cos\theta - 1). \qquad 1.40$$

Therefore, the first order quadrupole shift is reduced to zero under fast MAS ($\theta = 54.73°$).

However, the second order quadrupole shift (Equation 1.26) is more complex and cannot be described by a rank two tensor alone. The transformation from Σ^{ROT} gives the second order quadrupole shift as

$$\omega_{m-1,m}^{[2]ROT} = -\frac{4\omega_Q^2}{\omega_0} \left[\begin{array}{c} g(I,m,\eta_Q) + g'(I,m,\alpha,\beta,\eta_Q)P_2(\cos\theta) + \\ g^*(I,m,\alpha,\beta,\eta_Q)P_4(\cos\theta) \end{array} \right], \qquad 1.41$$

where the anisotropic components are now dependent on the second and fourth order Legendre polynomials given by Equation 1.39 and

$$P_4(\cos\theta) = \frac{1}{8}(35\cos^4\theta - 30\cos^2\theta + 3). \qquad 1.42$$

The magic angle is not a root of $P_4(\cos\theta)$ and no single angle reduces both the second and fourth order Legendre polynomials to zero. Therefore, the second order quadrupolar interaction cannot be fully removed by MAS and the resultant frequency shift of the CT is given by

$$\omega_{-\frac{1}{2},\frac{1}{2}}^{[2]MAS} = -\frac{1}{6\omega_0} \left[\frac{3C_Q}{2I(2I-1)} \right]^2 \left[I(I+1) - \frac{3}{4} \right] \left[\begin{array}{c} D(\alpha,\eta_Q)\cos^4\beta \\ +E(\alpha,\eta_Q)\cos^2\beta \\ +F(\alpha,\eta_Q) \end{array} \right] \qquad 1.43$$

where

$$D(\alpha,\eta) = \frac{21}{16} - \frac{7}{8}\eta_Q \cos 2\alpha + \frac{7}{48}\eta_Q^2 \cos^2 2\alpha,$$

$$E(\alpha,\eta) = -\frac{9}{8} + \frac{1}{12}\eta_Q^2 + \eta_Q \cos 2\alpha - \frac{7}{24}\eta_Q^2 \cos^2 2\alpha,$$

and

$$F(\alpha, \eta) = \frac{5}{16} - \frac{1}{8}\eta_Q \cos 2\alpha + \frac{7}{48}\eta_Q{}^2 \cos^2 2\alpha.$$

The orientation dependence of $\omega_{-1/2,1/2}^{[2]MAS}$ details the anisotropic powder patterns shown in Figure 1.7. Through simulation of the quadrupolar lineshapes, an NMR spectrum can be fitted allowing the experimental determination of the quadrupolar parameters C_Q and η_Q. As demonstrated by Equation 1.27 and 1.19, C_Q represents the magnitude of the quadrupolar interactions whereas η_Q is the asymmetry parameter for the EFG tensor. It is uncommon for an experimentally determined C_Q to be presented as an angular frequency, and is instead given as

$$C_Q = \frac{e^2 qQ}{h}. \qquad\qquad 1.44$$
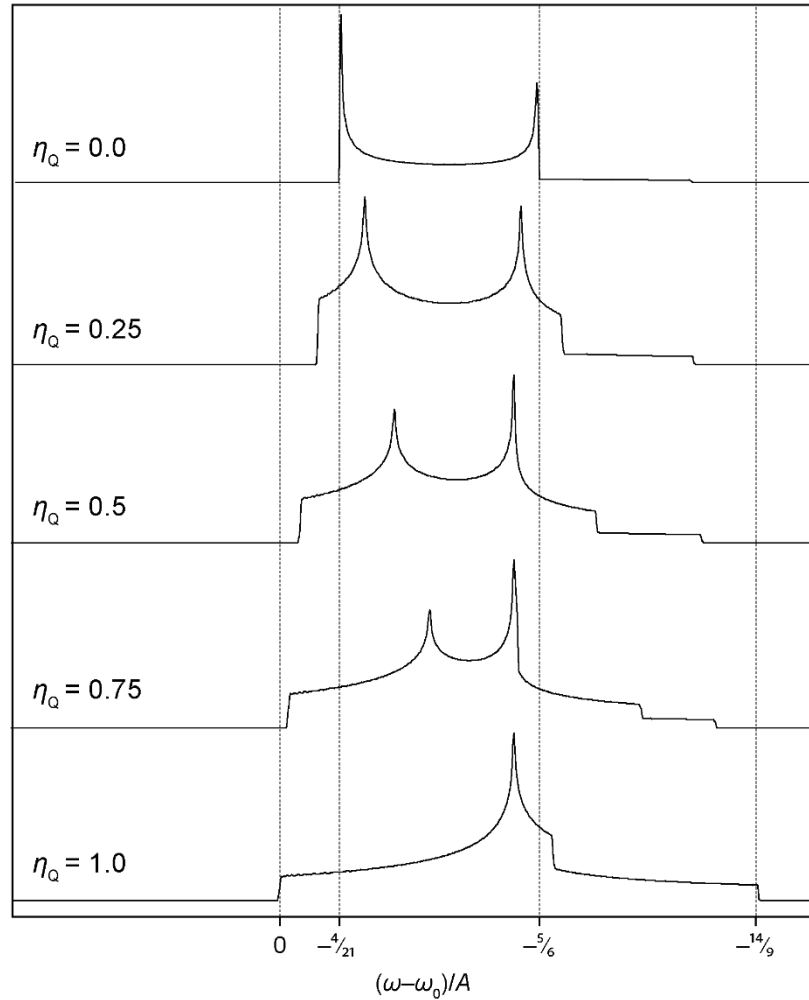
Figure 1.7 Powder patterns produced by the second order frequency shift at the CT in the fast MAS regime for varying values of η_Q. The powder patterns were simulated with *dmfit* and the parameter A is equal to

$$\frac{\omega_Q{}^2}{4\omega_0}\left[I(I+1) - \frac{3}{4}\right].$$

16

Although MAS cannot remove the orientation dependence of the CT, its quadrupolar lineshape is narrowed. The breadth of the CT powder pattern under fast MAS, determined from Equation 1.43, is given by

$$\Delta\left(\omega^{[2]}_{-\frac{1}{2},\frac{1}{2}}\right) = \frac{(6+\eta_Q)^2}{504}\left(\frac{\omega_Q^2}{\omega_0}\right)\left[I(I+1)-\frac{3}{4}\right].$$ 1.45

By comparing Equation 1.30 and 1.45, it can be shown that MAS narrows the CT lineshape by a factor of ~3. Additionally, the broadness of second order quadrupole lineshapes is inversely proportional to ω_0. Hence, higher B_0 field strengths can be used to provide better resolution of quadrupolar spectra.[8]

The centre of gravity of the second order quadrupole lineshapes of the CT (δ_{Qiso}) is given by

$$\delta_{Qiso} = \frac{1}{4\pi}\int_0^\pi d\beta \sin\beta \int_0^{2\pi} d\alpha\, \omega^{[2]MAS}_{-\frac{1}{2},\frac{1}{2}} \times \frac{10^6}{\omega_0} =$$

$$-\frac{3\left[I(I+1)-\frac{3}{4}\right]}{40I^2(2I-1)^2}\frac{C_Q^2}{\omega_0^2}\left(1+\frac{\eta_Q^2}{3}\right)\times 10^6.$$ 1.46

Furthermore, the experimental centre of gravity of the NMR resonance, δ_{CG}, is then given by

$$\delta_{CG} = \delta_{iso} + \delta_{Qiso} = \delta_{iso} + \left(\frac{P_Q}{\omega_0}\right)^2$$ 1.47

where δ_{iso} is the isotropic chemical shift and P_Q is

$$P_Q = C_Q\left(1+\frac{\eta_Q^2}{3}\right)^{\frac{1}{2}}.$$ 1.48

Similarly, to the quadrupole broadening, the δ_{CG} of a quadrupolar lineshape is dependent on B_0 via ω_0.[7]

The simulated powder patterns presented so far, are in practice only observed in perfectly crystalline materials. Many of the systems observed in this thesis, are characterised by local disorder. Such disorder creates a distribution of quadrupolar parameters over the nuclei sites in the material. The overlapping quadrupolar powder patterns for each site sum into an amorphous lineshape devoid of the sharp quadrupolar features. However, the disordered quadrupolar pattern retains a characteristic asymmetric lineshape. A Gaussian distribution of C_Q leads to the lineshapes shown in Figure 1.8, which were simulated using *QuadFit*.[13]
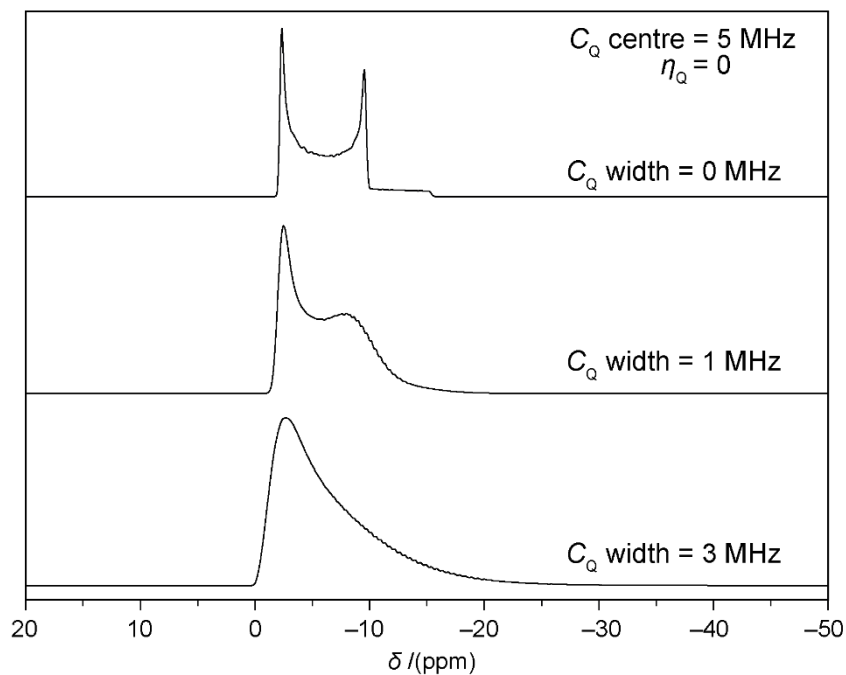
Figure 1.8 Simulated NMR lineshapes of the second order quadrupolar broadened CT of an $I = ^5/_2$ nucleus with $v_0 = 156.34$ MHz and $\eta_Q = 0$. Each lineshape has a Gaussian distribution of C_Q defined by a centre and width parameter. The lineshapes were simulated with *QuadFit*.

As the width of the C_Q distribution increases the lineshape broadens, presenting with a steep flank on the high frequency side and a long tail to lower frequencies.[14] A distribution of η_Q, results in more subtle differences in the lineshape, that are hidden by a large C_Q distribution.

2

The NMR Experiment

2.1. Net Magnetisation

The magnetic moment, $\hat{\mu}$, of a nuclear spin precesses around the direction of the applied field B_0 at the Larmor frequency (ω_0) with only the Zeeman interaction in effect. Without an applied magnetic field, a group of nuclei will have an isotropic distribution of magnetic moments. However, due to the Zeeman interaction in an applied field B_0 (Chapter 1.2), magnetic moments aligned with the field have lower energy than those aligned against. This results in a slight net alignment of moments parallel to B_0, and therefore a net magnetisation M_0 in the z-direction as shown in Figure 2.1.

Therefore, the probability of a nucleus' magnetic moment being aligned parallel to the magnetic field is dependent on the energy difference between the two-spin state. It also depends on the thermal energy of the system, due to thermal motion hindering the alignment of the spins. In the high-temperature limit when $\gamma\hbar B_0 \ll k_B T$ (which is appropriate for most NMR experiments), the average z-component of the magnetic moment is given by

$$\langle \hat{\mu}_z \rangle = \frac{(\gamma\hbar)^2 B_0 I(I+1)}{3k_B T} \qquad 2.1$$

where k_B is the Boltzmann constant and T is the temperature. The net magnetisation from the spin system is then defined as
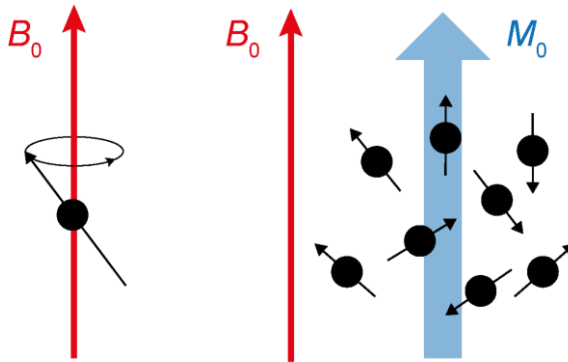
Figure 2.1 Representation of a nuclear magnetic moment precessing about B_0 and the resulting net magnetisation.

$$M_0 = N\langle \hat{\mu}_z \rangle \qquad 2.2$$

where N is the total population of nuclei.[2]

2.2. Radiofrequency Pulses

An EM wave includes a time dependent oscillating magnetic field $B(t)$. If the magnetic field is along the x-axis with a magnitude of $2B_1$ and oscillating at the frequency ω_{RF} then it is given by

$$B(t) = 2B_1 \cos(\omega_{RF}t) \, \hat{x}. \qquad 2.3$$

Following from the Zeeman Hamiltonian in Equation 1.2, the Hamiltonian for a nuclear spin, I, under the effect of an oscillating field ($\hat{H}_{RF}$) is given by

$$\hat{H}_{RF} = -\gamma \hbar \hat{I}_x (2B_1 \cos(\omega_{RF}t)). \qquad 2.4$$

If an oscillating magnetic field is introduced to the nuclear spin system under an applied magnetic field B_0, then the spin Hamiltonian is a combination of $\hat{H}_Z$ and $\hat{H}_{RF}$:

$$\hat{H} = \hat{H}_Z + \hat{H}_{RF} = -\gamma \hbar \left(B_0 \hat{I}_z + 2B_1 \cos(\omega_{RF}t)\hat{I}_x \right). \qquad 2.5$$

It is convenient to think of the oscillating magnetic field as two counter-rotating fields about the z-axis with magnitude B_1 and frequencies of ω_{RF} and $-\omega_{RF}$. Then by transforming the Hamiltonian into a frame rotating about the z-axis at a rate of ω_{RF} (Σ^{RF}), only the component rotating in phase with the magnetisation has an effect and the time dependent part of the Hamiltonian can be removed giving

$$\hat{H} = (-\gamma B_0 - \omega_{RF})\hbar \hat{I}_z - \gamma \hbar B_1 \hat{I}_x = (\omega_0 - \omega_{RF})\hbar \hat{I}_z - \gamma \hbar B_1 \hat{I}_x. \qquad 2.6$$

If the frequency of the oscillating magnetic field is made equal to the Larmor frequency ($\omega_{RF} = \omega_0$), then the Hamiltonian in the frame rotating at ω_0 is in the same form as the Zeeman Hamiltonian in the lab frame:

$$\hat{H} = -\gamma \hbar B_1 \hat{I}_x. \qquad 2.7$$

As described in Chapter 2.1, the Zeeman Hamiltonian results in a magnetisation that precesses around B_0. In the described rotating frame, the effective field is B_1 and, therefore, the magnetisation precesses around the x-axis. This precession is called nutation and the nutation frequency ω_{nut} is given by

$$\omega_{nut} = -\gamma B_1. \qquad 2.8$$
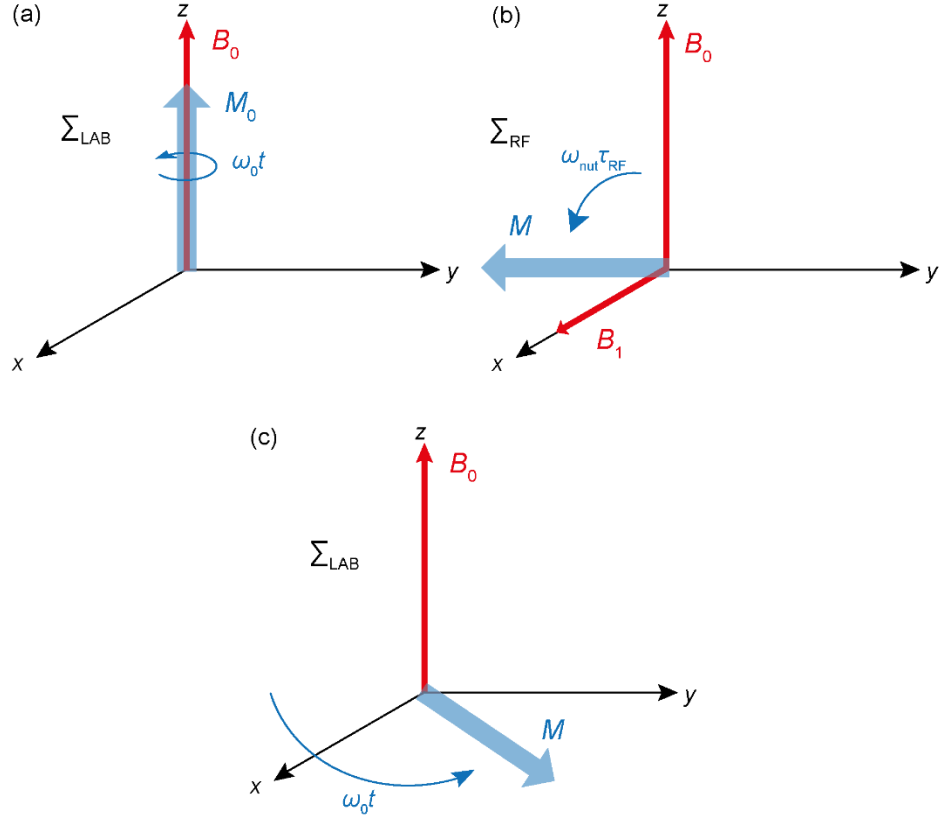
Figure 2.2 Representation of (a) the equilibrium net magnetisation precessing about B_0 in Σ^{LAB}, (b) the creating of transverse magnetisation by an RF pulse magnetisation in Σ^{RF}, and (c) the precession of the transverse magnetisation about B_0 in Σ^{LAB}.

The magnetisation is nutated by an angle θ_{nut}, called the flip angle, during the time τ_{RF}:

$$\theta_{nut} = \omega_{nut}\tau_{RF}. \hspace{3cm} 2.9$$

Therefore, a pulse of EM radiation along the x-axis at the frequency ω_0, with the correct amplitude B_1 and duration τ_{RF}, can rotate the magnetisation to be along the $-y$-axis ($\theta_{\text{nut}} = \pi/_2$); this is shown in Figure 2.2. Back in the laboratory frame Σ^{LAB}, the magnetisation still precesses around B_0 in the x-y plane at ω_0.

The Larmor frequencies ω_0 at the B_0 fields used in NMR, fall within the radiofrequency range. Hence, the pulses of EM radiation used in NMR are referred to as radiofrequency (RF) pulses. The RF pulse is a fundamental component of the NMR experiment, because by flipping the magnetisation into the x-y plane, its precession about B_0 can be measured (see Chapter 2.4.1).[1, 15]

2.2.1. Excitation

The determination of the nutation frequency above, assumes the presence of only the Larmor interaction and, therefore, only one precession frequency (ω_0) for the RF frequency (ω_{RF}) to match. However, the multiple internal interactions, described in Chapter 1.3, all cause shifts to the precession frequency based on the nuclear environment. Hence, each magnetic moment has its own effective precession frequency, or resonance. The RF pulse is required to cover the resonance frequencies of all the nuclear spins in the system to ensure the complete transition of magnetisation into transverse magnetisation. This "excitation" of a small frequency range can be achieved due to the excitation bandwidth of the pulse.

Due to the difference between the effective precession frequency and the RF frequency, it is useful to define a frequency offset, Ω, as

$$\Omega = \omega - \omega_{RF}. \tag{2.10}$$

The frequency domain function $A(\omega)$ corresponding to a rectangular RF pulse of frequency ω_{RF} and duration τ_{RF} is a sinc function (*i.e.* the Fourier transform of a rectangular function is a sinc function):

$$A(\omega) = \frac{sin(\Omega\tau_{RF})}{\Omega\tau_{RF}}. \tag{2.11}$$

Due to the sinc wave nature of the frequency domain, a range of frequencies are excited by the RF pulse. The excitation is > 90% of the maximum for frequency offsets within a range defined by

$$|\Omega\tau_{RF}| < \frac{\pi}{4}. \tag{2.12}$$

Hence, a uniform excitation bandwidth, Δf, is generally defined as

$$\Delta f = \frac{2|\Omega|}{2\pi} = \frac{1}{4\tau_{RF}}. \tag{2.13}$$
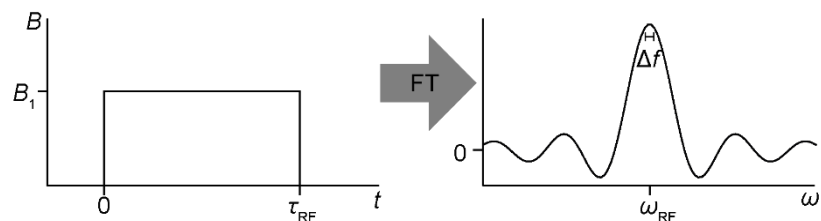
Figure 2.3 Graphical representation of a rectangular RF pulse that upon Fourier transformation becomes a sinc frequency spectrum with bandwidth Δf.

A representation of a rectangular RF pulse and the resulting excitation bandwidth is shown in Figure 2.3.

Therefore, by using an RF pulse with a minimal duration, τ_{RF}, the excitation bandwidth, Δf, can be maximised. From Equation 2.9, an RF pulse with a short τ_{RF}, requires a large B_1 amplitude to achieve the desired flip angle. Such short, high power pulses are termed hard pulses and are commonly used in solid state NMR experiments.[2]

2.2.2. Quadrupolar Nutation

Another issue with the determination of the nutation frequency (Chapter 2.2), occurs due to the assumption that the RF pulse Hamiltonian, $\hat{H}_{RF}$, overwhelms the internal spin interactions. However, the quadrupolar interaction can often be on par with, or even larger than that of the RF pulse.

When $\hat{H}_{RF} \gg \hat{H}_Q$, a hard pulse, or "non-selective" pulse, can excite the entire quadrupole frequency range. In this case the nutation frequency remains as described in Equation 2.8

$$\omega_{nut}^{ns} = -\gamma B_1.$$

2.14

When $\hat{H}_{RF} \approx \hat{H}_Q$, only part of the frequency range can be excited by the "selective" pulse, usually chosen to be the CT. In this case, the quadrupolar Hamiltonian cannot be ignored, so the spin Hamiltonian given in Equation 2.5 becomes[16]

$$\hat{H} = \hat{H}_Z + \hat{H}_{RF} + \hat{H}_Q.$$

2.15

This obviously complicates the derivation of the nutation frequency, which is given in full in the review by Freude and Haase.[17] However, the result is fairly simple; the nutation frequency of the CT during a selective pulse ($\omega_{nut}^{s,CT}$) is given by

$$\omega_{nut}^{s,CT} = \left(I + \frac{1}{2}\right)\omega_{nut}^{ns} = -\gamma B_1 \left(I + \frac{1}{2}\right).$$

2.16

Hence, a selective excitation of the CT quadrupolar resonance causes a faster nutation of magnetisation than the excitation of a non-quadrupolar ($C_Q = 0$) resonance. Furthermore, if the RF amplitude B_1 is identical for both cases, then the duration of the pulse required to achieve the same flip angle is

$$\tau_{RF}^{ns} = \left(I + \frac{1}{2}\right)\tau_{RF}^{s,CT}.$$

2.17

This relationship is important for the calibration of RF pulses in quadrupolar NMR experiments.

Furthermore, the magnitude of the magnetisation in the *x-y* plane (transverse magnetisation) after an RF pulse of amplitude B_1 and duration τ_{RF} for both a non-quadrupolar resonance and a quadrupolar CT resonance is given by

$$M_t^{ns} = M_0 \sin \omega_{nut}^{ns} \tau_{RF} \qquad\qquad 2.18$$

and

$$M_t^{s,CT} = \frac{M_0}{\left(I + \frac{1}{2}\right)} \sin\left[\left(I + \frac{1}{2}\right) \omega_{nut}^{ns} \tau_{RF}\right] \qquad\qquad 2.19$$

respectively.[18] If the duration τ_{RF} is chosen so that $\omega_{nut}^{ns}\tau_{RF} \ll \pi$, then via the small angle approximation

$$M_t^{s,CT} \approx M_t^{ns}. \qquad\qquad 2.20$$

This leads to the uniform excitement condition for quadrupolar nuclei

$$\left(I + \frac{1}{2}\right)\omega_{nut}^{ns}\tau_{RF} \leq \frac{\pi}{6} \qquad\qquad 2.21$$

which results in < 5% difference in the transverse magnetisation of the two resonances. Therefore, small flip angles are preferred in the selective excitation of quadrupolar nuclei to allow quantitative interpretations of NMR data.[19] However, a smaller flip angle will not produce maximal transverse magnetisation, resulting in a weaker NMR signal (see Chapter 2.4.1). Hence, the choice of flip angle in an NMR experiment on a quadrupolar nucleus is a compromise between quantitative results and signal strength.

2.3. Relaxation

The net magnetisation after an RF pulse does not remain in the *x-y* plane indefinitely. Over time, the magnetisation will relax back to its equilibrium position parallel to B_0. The recovery of the *z*-component of the equilibrium magnetisation is called longitudinal (T_1) relaxation. The loss of magnetisation in the *x-y* plane is called transverse (T_2) relaxation.

2.3.1. Longitudinal Relaxation

As explained in Chapter 2.1, the net magnetisation is the sum of all the spin magnetic moments in the system. Immediately after the application of the static field B_0, the magnetic moments in the system are randomly orientated. Each magnetic moment precesses around B_0, forming a "cone of precession" depending on its orientation. In a perfectly isolated spin system, the orientation of the cone of precession around B_0 would remain constant for each spin magnetic moment. However, in real systems the nuclear spin is affected by additional small magnetic fields produced by the surrounding electrons and nuclei. These local fields are the cause of the internal spin interactions discussed in Chapter 1.3. They also act to create an effective field at the nucleus whose orientation slightly differs from B_0. Due to thermal agitation of the surroundings, the effective field has a slight fluctuation in direction and magnitude. Therefore, the effective field felt by any one nuclear spin is slightly different at any point in time. Hence, the orientation of the precession cone of each nuclear spin magnetic moment also fluctuates. This causes a "wandering" motion of the nuclear spin precession cones, which over time allow each nuclear magnetic moment to sample every possible orientation (Figure 2.4).

Also explained in Chapter 2.1, is the preferred alignment of the nuclear spin magnetic moments with B_0. The wandering thermal motion of the magnetic moments, allows the slight majority of spins aligned with B_0 to form, creating the equilibrium net magnetisation. The same process occurs immediately after an RF pulse. As discussed in Chapter 2.2, an RF pulse along the x-axis with $\theta_{\text{nut}} = {}^\pi/_2$ rotates the magnetic polarisation to be in the $-y$ direction (*i.e.* there is a slight majority of magnetic moments aligned with the $-y$-axis). The wandering
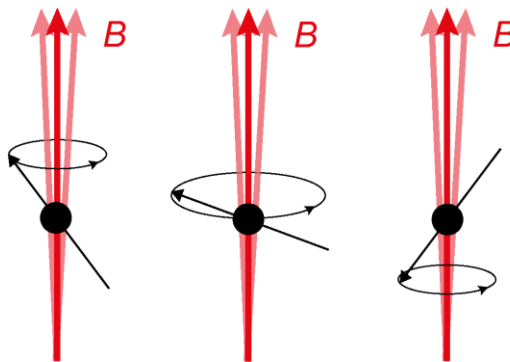
Figure 2.4 Representation of the fluctuating field *B* felt by a nuclear magnetic moment resulting in a wandering precession cone.

thermal motion of the magnetic moments slowly brings them back to equilibrium with the B_0 field. The return of the magnetisation's z-component is approximately exponential and can, therefore, be expressed as

$$M_z(t) = M_0 \left(1 - e^{-\frac{t}{T_1}}\right).$$

2.22

The rate of the longitudinal relaxation is then described by the characteristic relaxation time T_1.[1]

In more complex cases the longitudinal relaxation can be described by a bi-exponential or a stretched-exponential function. A bi-exponential function is appropriate when nuclei in two different environments have similar frequencies but substantially different relaxation rates. The transverse relaxation is then given by

$$M_z(t) = M_0' \left(1 - e^{-\frac{t}{T_1'}}\right) + M_0'' \left(1 - e^{-\frac{t}{T_1''}}\right)$$

2.23

where T_1' and T_1'' are the characteristic relaxation times of the two environments, and M_0' and M_0'' are the initial magnetisations. Bi-exponential relaxation can also occur in the magnetisation recovery of the CT of a strongly quadrupolar nuclear site. The non-exponential relaxation is due to the incomplete excitation of the complete quadrupolar lineshape (CT and STs).[20]

When multiple environments have similar frequencies and separate, but similar, relaxation rates, it can be convenient to describe the range of relaxation rates as a probability distribution. In such cases the observed longitudinal relaxation can be modelled by a stretched exponential function given by

$$M_z(t) = M_0 \left(1 - e^{-\left(\frac{t}{T_1^*}\right)^x}\right).$$

2.24

where the probability distribution of relaxation rates is defined by the parameters T_1^* and x (where $0 < x \leq 1$). For example, a low x provides a broad distribution of relaxation rates centred about T_1^*, whereas $x = 1$ provides a single relaxation rate (*i.e.* the single exponential function with $T_1 = T_1^*$). Stretched exponential functions have been found to accurately describe the longitudinal relaxation in several disordered systems (such as a system with an inhomogeneous distribution of paramagnetic impurities) and the parameter x tends to fall within a defined range of $0.5 < x < 1$. [21]

2.3.2. Transverse Relaxation

As the longitudinal magnetisation returns to its equilibrium position via the wandering thermal motion of the magnetic moments, there is a concurrent loss of transverse magnetisation called non-secular transverse relaxation. Hence, any longitudinal relaxation results in an equivalent non-secular transverse relaxation, and therefore their rates are equal.

However, there is an additional way in which the transverse magnetisation is lost. The effective precession frequency of a nuclear spin magnetic moment about B_0, is actually the combination of the Larmor frequency and the small frequency shifts caused by the internal spin interactions (Chapter 1.3). The thermal agitation of the surroundings, creates small variations in the frequency shifts in time. Hence, the effective precession frequency of each magnetic moment will fluctuate slightly. Over time, the precession of the individual magnetic moments will become out of phase with each other as shown in Figure 2.5. The net transverse magnetisation, which results from the slight alignment of the magnetic moments, will be reduced by this "dephasing". This loss of transverse relaxation by dephasing of the individual precession frequencies, rather than the fluctuating direction of the precession cones, is the secular transverse relaxation contribution.

Analogous to the longitudinal relaxation, the loss of transverse magnetisation can be represented as

$$M_t(t) = M_0\left(e^{-\frac{t}{T_2}}\right). \qquad 2.25$$

The rate of the transverse relaxation is then described by the characteristic relaxation time T_2.[15]
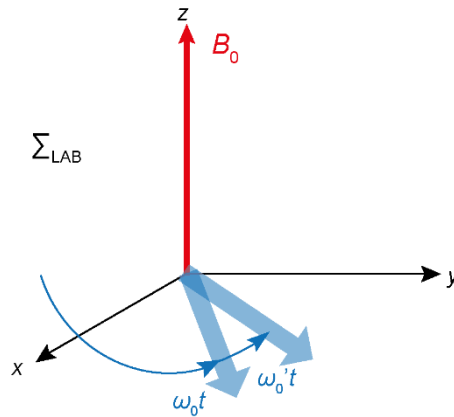
Figure 2.5 Representation of two transverse magnetisation components with effective precession frequencies ω_0 and ω_0' becoming out of phase with each other.

2.4. Signal Detection

2.4.1. Free Induction Decay

The transverse magnetisation immediately after a $^\pi/_2$ pulse along the x-axis is given as

$$M_y = -M_0 \qquad\qquad 2.26$$

if measured in the rotating frame Σ^{RF}. The transverse magnetisation precesses around the z-axis at the frequency offset Ω of its effective precession frequency (Equation 2.10) and relaxes following Equation 2.25. Therefore, the transverse magnetisation, in its x and y components, is given by

$$M_y = -M_0 \cos \Omega t \left(e^{-\frac{t}{T_2}}\right); \; M_x = -M_0 \sin \Omega t \left(e^{-\frac{t}{T_2}}\right). \qquad 2.27$$

The oscillating magnetic field induces a current in the detection apparatus creating a signal for both magnetisation components. It is convenient to combine the two generated signal components into a complex signal of the form

$$S(t) = S_x + iS_y = S_0 e^{i\Omega t} e^{-\frac{t}{T_2}}. \qquad\qquad 2.28$$

This time-domain signal is called the free induction decay (FID).[15] The single pulse NMR experiment described so far, and the resulting FID is schematically represented in Figure 2.6.

2.4.2. Fourier Transform

By Fourier transforming the time-domain signal a frequency domain signal (or frequency spectrum) is produced. The Fourier transform of Equation 2.28 gives
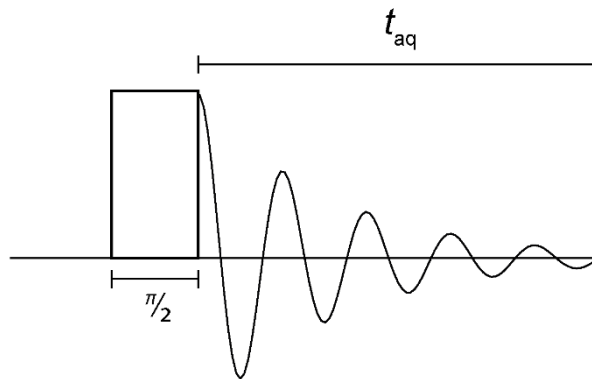
Figure 2.6 A schematic pulse sequence diagram of a single pulse NMR experiment which includes a $^\pi/_2$ pulse and the acquisition time $t_{aq.}$

$$S(\omega) = A(\omega) + iD(\omega) \qquad\qquad 2.29$$

where

$$A(\omega) = \frac{\left(\frac{1}{T_2}\right)}{\left(\frac{1}{T_2}\right)^2 + (\omega - \Omega)^2} \qquad\qquad 2.30$$

and

$$D(\omega) = \frac{-(\omega - \Omega)}{\left(\frac{1}{T_2}\right)^2 + (\omega - \Omega)^2}. \qquad\qquad 2.31$$

The real part of the signal (Equation 2.30) gives an absorption Lorentzian centred at Ω. Multiple components with different frequencies Ω in the time-domain signal will result in multiple Lorentzian lineshapes in the frequency-domain signal. This provides the desired result of a frequency spectrum with resonances whose positions are related to the effective precession frequencies of different chemical environments.

So far, the direction of the RF pulse has been assumed to be along the x-axis. However, the pulse can be along any direction in the x-y plane. The direction of the pulse is described by the phase φ, which affects the resultant magnetisation producing

$$M(t) = M_0 e^{i\Omega t} e^{i\varphi} e^{-\frac{t}{T_2}}. \qquad\qquad 2.32$$

If the measurement of the signal does not occur in the same phase as the magnetisation then an arbitrary phase φ' is carried into the time-domain signal

$$S(t) = S_0 e^{i\Omega t} e^{i\varphi'} e^{-\frac{t}{T_2}}. \qquad\qquad 2.33$$

This results in the real part of the frequency-domain becoming a mixture of the absorption and dispersion lineshapes $A(\omega)$ and $D(\omega)$. To rationalise this a correction phase (φ_{corr}) can be added post detection to remove the arbitrary phase φ' if

$$e^{i\varphi'} e^{icorr} = 0. \qquad\qquad 2.34$$

This process is called phasing.[15]

2.4.3. Phases and Coherences

The phase of the signal added by the RF pulse can be used advantageously by applying a technique called phase cycling. To describe phase cycling, it is first necessary to introduce

the concept of coherences. As described in Chapter 2.1, a spin system at equilibrium with an applied magnetic field will be polarized due to the difference in populations of the two spin states. Once the net magnetisation is rotated into the x-y plane by an RF pulse, the polarisation is now perpendicular to the external field. The transverse synchronisation of the magnetic moments resulting from the polarisation between the two spin states is called a coherence. It is useful to define a coherence with the quantum number coherence order, p. For a non-interacting $I = \frac{1}{2}$ spin system there are two spin states $m = \pm\frac{1}{2}$. Hence, there are three possible coherence orders: $p = 0$ for longitudinal magnetisation and $p = \pm 1$ for transverse magnetisation. The RF pulse, therefore, alters the coherence order by $\Delta p = \pm 1$. The $p = \pm 1$ coherences (single quantum coherence) are the only coherences that can produce a directly observable signal.

In more complicated spin systems, like for a quadrupolar system, there are multiple spin states. Therefore, there are higher order coherences (multiple quantum coherences) with coherence order of $p = \pm2, \pm3$, etc. An RF pulse will excite all coherences but only the single quantum coherence can be detected. However, if a sequence of pulses is applied then these multiple quantum coherences can affect the observable single quantum coherence and be indirectly detected.

A coherence order pathway describes the evolution of the coherences during a specific pulse sequence. Each pulse produces a change in coherence order of Δp. The change of phase produced by the pulse $\Delta\varphi$, results in a coherence phase shift of $\Delta p \cdot \Delta\varphi$. Therefore, by varying the phase of the pulses a distinct phase shift can be applied to a desired coherence order pathway. By matching the phase of detection to the appropriate coherence phase shift, the desired coherence order pathway can be detected, while the other coherence order pathways are ignored.

The use of phase shifts to select a desired coherence pathway is called phase cycling. It allows NMR experiments to manipulate the multiple quantum coherences, which can provide further details about the interactions in the system. This has led to the development of increasingly complex NMR techniques with multiple pulse sequences. A full description of coherences, and therefore phase cycling, requires knowledge of the density matrix formalism of spin systems, which is described in detail by Duer.[3]

2.5. Solid State NMR Instrumentation

The NMR experiment detailed so far requires a basic set of equipment that make up the NMR spectrometer. These components include: a magnet to provide the static B_0 field; an NMR probe to place the sample into the B_0 field, apply RF pulses to the sample, measure the resultant transverse magnetisation and to spin the sample at the MAS frequency; a transmitter to generate RF pulses; a receiver to record the NMR signal; and a computer to store the digital signal and Fourier transform it into a frequency spectrum.

The NMR signal strength and resolution are improved by higher B_0 fields, which has led to increasing strengths of NMR magnets. The highest commercially available NMR magnet at the time of writing is 24 T.[22] The high B_0 fields used in most modern NMR spectrometers is provided by a superconducting solenoidal magnet. The solenoid coil sits in a liquid helium bath to maintain the necessary temperature for superconduction. To conserve helium, temperature losses must be minimised. This is achieved via an enclosing sacrificial liquid nitrogen reservoir, vacuum chamber layers and heat shields. Magnet uniformity is improved through multiple smaller cryo-shimming coils which apply gradient fields to correct for inhomogeneity.

Modern MAS NMR probes use high pressure gas to spin cylindrical sample containers with fluted caps, called rotors. Smaller rotors can be spun very fast (up to 111 KHz),[22] and can therefore achieve great resolution. However, this is a trade off with the weaker NMR signal provided by the small volume of sample. To survive the high spinning speeds, the rotors themselves must have a high strength-to-mass ratio while preferably being relatively NMR inactive. Partially stabilised zirconia is the generally preferred material for NMR rotors. The probe contains a solenoidal coil that acts to transmit the RF pulse and receive the NMR signal. The probe circuitry must be finely tuned to ensure efficient transmission and reception of the desired Larmor frequency. Different probes cover select frequency ranges and are designed for a specific rotor size. Specialised probes can also offer other features, such as variable temperature or multi-resonance acquisition. Therefore, choosing the correct probe for one's experimental needs is a key part of the NMR experiment.

The console contains the rest of the electronics involved in the NMR experiment. The transmitter must be able to provide all the possible Larmor frequencies for the field strength of its magnet. A frequency synthesizer produces the desired frequency which is then amplified to the correct B_1 field strength. The RF signal is then gated to produce the RF

pulses. The receiver must amplify the weak NMR signal before detection. Great care must be taken to ensure the high power transmitted frequencies do not damage the sensitive receiver electronics. The pre-amplification at the receiver adds noise to the signal as an unwanted side effect. The signal is then digitized to be stored by the computer. The computer Fourier transforms the NMR signal to produce the frequency spectrum, alongside additional processing such as phasing.[2]

A very important gauge of the NMR experiment is the signal-to-noise ratio (SNR) of the NMR signal. Naturally, it is effected by the instrumentation used. The SNR is defined as the peak signal voltage V_{signal} over the root mean square of the noise voltage V_{noise} which can be roughly calculated using

$$SNR = \frac{V_{signal}}{V_{noise}} = N_T^{\frac{1}{2}} \frac{M_0 \omega_0 V_s}{\left(k_B T (R_s + R_c)\right)^{\frac{1}{2}} \Delta f^{\frac{1}{2}}} \left(\frac{B_1}{i}\right) \qquad 2.35$$

where M_0 is the equilibrium magnetisation (Equation 2.2); ω_0 is the Larmor frequency (Equation 1.3); V_s is the sample volume; B_1/i is the strength of the RF field per unit current which gives the sensitivity of the coil; k_B is the Boltzmann constant; T is the temperature of the sample/coil; R_s and R_c are the resistances of the sample and coil respectively; and Δf is the frequency bandwidth. An NMR signal is naturally quite insensitive, so in most NMR experiments multiple repeated NMR signals, or transients, are acquired and then averaged. This averaging increases the SNR by the square root of the number of transients (N_T) averaged over. From Equation 2.35, it is of interest to note that the SNR is proportional to the cube of the gyromagnetic ratio of the observed nucleus.[23]

3

Analytical Techniques

3.1. NMR Techniques

The single pulse NMR experiment described in Chapter 2, provides an excellent analytical technique by itself. However, by using a sequence of multiple pulses the spin system and its interactions can be manipulated further. These pulse sequences can assist in the acquisition of the NMR signal, extract additional information about the nuclear spins or suppress specific internal interactions. In addition to single pulse NMR experiments this thesis makes use of the following pulse sequence NMR techniques.

3.1.1. The Spin Echo Experiment

Chapter 2.3.2 assumes a perfectly homogenous B_0 field where transverse relaxation is only caused by differences in the local field. In reality, the applied field B_0 is spatially inhomogeneous. The variations in the applied field felt by each nuclear spin result in transverse magnetisation loss just as the variations in the local fields do. Therefore, the observed transverse relaxation is a combination of both the "homogenous" and "inhomogeneous" contributions. The transverse magnetisation decay is then given by

$$M_t(t) = M_0 \left(e^{-\frac{t}{T_2^*}} \right)$$
3.1

where

$$\frac{1}{T_2^*} = \frac{1}{T_2} + \frac{1}{T_2'}.$$
3.2

The rates of the observed transverse relaxation and the homogenous and inhomogeneous transverse relaxation contributions are given by the characteristic relaxation times T_2^*, T_2 and T_2' respectively.

The homogenous relaxation is the result of the time-dependent local fields from the internal interactions (see Chapter 2.3.2). The inhomogeneous relaxation is instead caused by spatial variations in the static field, and as such the produced differences in the precession
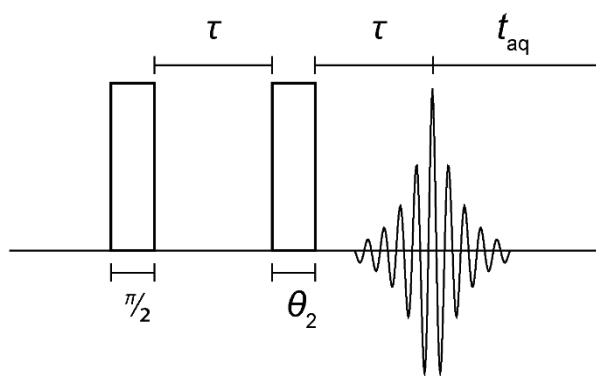
Figure 3.1 A schematic pulse sequence of a spin echo NMR experiment which includes: a $\pi/2$ pulse, the delay τ, a refocusing pulse θ_2 and the acquisition time $t_{aq.}$

frequencies of the individual nuclear spins are time independent. Therefore, the inhomogeneous relaxation can be reversed. The reversal of inhomogeneous relaxation is used advantageously in a spin echo experiment, which consists of two pulses separated by a time delay τ as shown in Figure 3.1. The first pulse ($\pi/2$) creates the transverse magnetisation that dephases over time τ. In a Hahn echo pulse sequence, the second pulse (π) rotates the dephased magnetisation components 180° around the pulse axis. The order of precession of the dephased components is now reversed allowing faster precessing components to catch up to the slower ones. Therefore, the magnetisation refocuses after a further delay of τ. Hence, the time domain signal then consists of a signal 'echo' at τ which then decays normally.

Echo techniques are useful due to the delayed appearance of the echo signal. The RF pulse in a strong magnetic field can induce mechanical oscillations in the structure of the probe, especially at low frequencies. These acoustic vibrations can in turn generate a signal that is detected by the NMR experiment. The detected "acoustic ringing" in the NMR signal decays rapidly but can overshadow fast relaxing components. The delay in measurement, post an RF pulse in spin echo experiments, allows for the ringing to be avoided.

The Hahn echo ($\pi/2$)-τ-(π) sequence is used for relaxation caused by first order interactions (*i.e.* those described by a second rank tensor; see Chapter 1.4). However, the refocusing of relaxation due to the quadrupolar interaction (which cannot be described by a second rank tensor alone) is more complex.[3]

For non-selective excitation of an entire quadrupolar lineshape ($\hat{H}_{RF} \gg \hat{H}_Q$), the echo pulse sequence must refocus the magnetisation from the central and satellite transitions created by the first order quadrupolar interaction (see Figure 1.5). Due to the complex evolution of the

34

multiple quantum coherences, the magnetisation from each transition is maximally refocused by a second pulse with a different flip angle. For the full derivation of the echo amplitudes please refer to the review by Freude and Haase.[17] The total echo produced by the sequence is therefore a combination of the refocused magnetisation of the separate transitions. The total echo is maximal when using a $(\pi/2)$-τ-$(\pi/2)$ sequence, where the two pulses are $\pi/2$ out of phase with each other. Such a pulse sequence is referred to as a solid (or quadrupolar) echo. It is most commonly used for static measurements of quadrupolar nuclei. An additional advantage of using a solid echo, rather than a Hahn echo, for broad quadrupolar lineshapes is the larger uniform excitation bandwidth provided by using a shorter second pulse.

For selective excitation of a quadrupolar lineshape ($\hat{H}_{RF} \approx \hat{H}_{Q}$) only the central transition needs to be refocused by an echo pulse sequence. The excitement of the single transition can be imagined as the excitement of a fictitious spin $1/2$ system and, therefore, the Hahn echo sequence, using selective pulse durations (see Chapter 2.2.2), provides the most efficient refocusing of the magnetisation. Smaller flip angles can also be incorporated into a Hahn echo pulse sequence to ensure quantitative results from quadrupolar nuclei, analogously to a single pulse experiment.[24]

3.1.2. The Saturation Recovery Experiment

The rate of the longitudinal relaxation of an NMR resonance can be useful for determining its environment, due to its relation to the behaviour of the surrounding electrons and nuclei. The saturation recovery experiment is used to find the characteristic relaxation time T_1 of an NMR resonance, which describes the rate of the longitudinal relaxation (see Chapter 2.3.1). The basic principle behind this sequence is to apply a $\pi/2$ pulse to remove any longitudinal magnetisation. The longitudinal magnetisation is then allowed to recover for time t_1. Then a second $\pi/2$ pulse rotates the recovered longitudinal magnetisation into the *x-y* plane where it is detected. By varying the time t_1 and measuring the intensity of the resultant NMR resonances, the recovery of the longitudinal magnetisation can be followed. The plotted results of the saturation recovery will give a function which can be fitted to Equation 2.22 and, therefore, the characteristic relaxation time T_1 can be determined.

With this basic experiment, the magnetisation must be allowed to completely return to equilibrium prior to repetition with a different t_1 delay. In a system with long T_1, this can
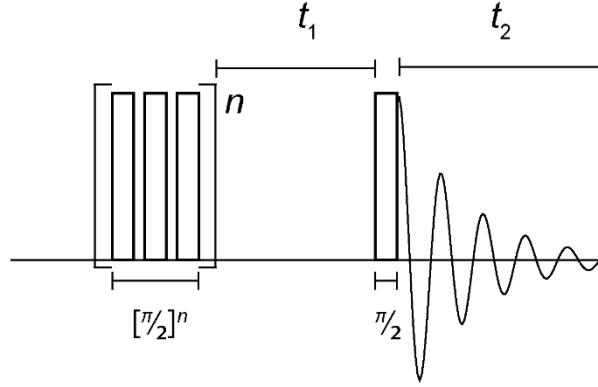
Figure 3.2 The pulse sequence diagram of the saturation recovery NMR experiment which includes: a saturation comb of n $^{\pi}/_2$ pulses, a variable delay t_1, a final $^{\pi}/_2$ pulse and the acquisition time t_2.

cause excessive experimental times and requires some *a priori* knowledge of T_1. In actuality, a chain of $^{\pi}/_2$ pulses are rapidly applied with separation times τ (where $T_2 < \tau \ll T_1$), in place of the singular initial pulse, as shown in Figure 3.2. This ensures the destruction of all net magnetisation due to the complete saturation of the spin system. The recovery profile of the longitudinal magnetisation remains the same, but experiments can be repeated without a delay, as the saturation pulse train removes any remaining magnetisation.[25]

3.1.3. The Multiple Quantum MAS Experiment

Frydman and Harwood developed a 2D MAS NMR experiment that manipulates the undetectable multiple-quantum (MQ) transitions to remove the anisotropic components of the second order quadrupole interaction (see Chapter 1.4.1), called MQMAS.[26] The frequency shift in the fast MAS regime of the symmetric $\frac{p}{2} \leftrightarrow -\frac{p}{2}$ transitions, which are not affected by the first order interaction, can be separated into isotropic and anisotropic components as described by Freude:[18]

$$\omega^{[2]MAS}_{\frac{p}{2},-\frac{p}{2}} = \frac{p\omega_Q{}^2}{\omega_0}\left(\frac{2\left(1+\frac{\eta_Q{}^2}{3}\right)}{15}\left[I(I+1)-\frac{3}{4}p^2\right] - \frac{h(\alpha,\beta,\eta_Q)}{3240}[36I(I+1)-17p^2-10] \right).\qquad 3.3$$

The phase development $\varphi(t)$ of the multiple-quantum coherence p is described by

$$\frac{\varphi(t)}{t} = \omega p + \omega^{[2]MAS}_{\frac{p}{2},-\frac{p}{2}}.\qquad 3.4$$

The sign of the phase development at the multiple-quantum coherence p is inverted for the observable coherence $p = -1$. Therefore, the anisotropic components of the quadrupolar interaction can be cancelled out by manipulating the coherences. The MQMAS sequence allows the phase to develop at coherence p for a duration of t_1, before converting to $p = -1$ where it freely evolves over a time of t_2. From Equation 3.3, the anisotropic components of the quadrupolar interaction are removed when

$$t_2 = \frac{36I(I + 1) - 17p^2 - 10}{36I(I + 1) - 27} pt_1 = R(I, p)t_1. \qquad 3.5$$

A 2D Fourier transform of the time domain signal with respect to t_1 and t_2, provides a 2D correlation spectrum with axes δ_1 and δ_2, which represent shifts in the multiple and single quantum dimensions respectively. The 2D spectrum consists of narrow resonance bands, with ridges along the slope of the anisotropic axis, which is given by

$$\delta_1 = R(I, p)\delta_2, \qquad 3.6$$

A projection of the 2D spectrum perpendicular to the slope $R(I,p)$ yields an 1D isotropic spectrum free from quadrupolar broadening.

A shearing transformation can align the ridges along the δ_2 direction, transforming δ_1 into a new isotropic dimension δ_1^{shear}. The isotropic components of δ_1 and δ_2 are

$$\delta_1 = \delta_{CSiso} + \delta_{Qiso}(p) = \delta_{CSiso} - \frac{2\omega_Q^2 \left(1 + \frac{\eta_Q^2}{3}\right)}{15\omega_0^2} \left[I(I + 1) - \frac{3}{4}p^2\right] \qquad 3.7$$

and

$$\delta_2 = \delta_{CSiso} + \delta_{Qiso}(p = -1) = \delta_{CSiso} - \frac{2\omega_Q^2 \left(1 + \frac{\eta_Q^2}{3}\right)}{15\omega_0^2} \left[I(I + 1) - \frac{3}{4}\right] \qquad 3.8$$

respectively. The terms δ_{CSiso} and δ_{Qiso} represent the isotropic components of the chemical shielding shift and the quadrupolar shift. In Equation 3.8, δ_2 gives the centre of gravity of the anisotropic ridge, which is not affected by the transformation. The δ_1^{shear} coordinate after the transformation is given by

$$\delta_1^{shear} = \delta_{CSiso} + \delta_{Qiso}^{shear} = \delta_{CSiso} + \frac{4\omega_Q^2 \left(1 + \frac{\eta_Q^2}{3}\right)}{51\omega_0^2} \left[I(I + 1) - \frac{3}{4}\right], \qquad 3.9$$
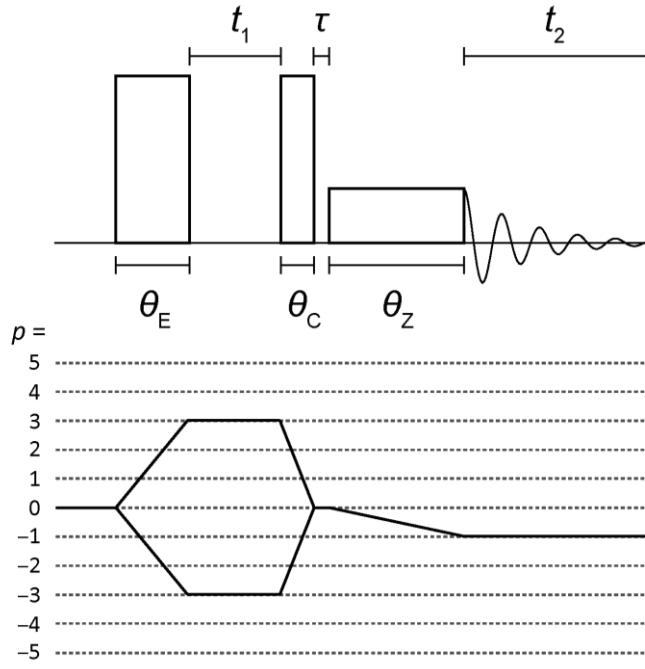
Figure 3.3 A schematic pulse sequence and coherence transfer pathway diagram of a z-filter 3QMAS NMR experiment which includes: an excitation pulse θ_E, a variable delay t_1, a conversion pulse θ_C, a short delay τ, a soft z-filter pulse θ_Z and the acquisition time t_2.

where the quadrupolar shift is positive and p independent. After shearing, the projection of the resonances at the δ_1^{shear} and the δ_2 axes provide isotropic and MAS spectrums respectively. To reflect this, δ_1^{shear} and δ_2 axes are labelled as δ_{iso} and δ_{MAS} in this work. The line $\delta_1^{\text{shear}} = \delta_2$ (labelled CS) describes the variable isotropic chemical shift where the quadrupolar shift is zero. The slope $\delta_1^{\text{shear}} = -\frac{10}{17}\delta_2$ (labelled QIS) describe the variable quadrupolar shift at a constant δ_{CSiso} value defined by the chosen intercept of CS and QIS. The 1D projections of the individual anisotropic resonances can be obtained from slices in the δ_2 direction in the 2D spectra. Therefore, the 2D MQMAS spectrum distinguishes between NMR resonances by both their isotropic chemical shift and their quadrupolar shift, which greatly assists in the deconvolution of complex NMR lineshapes.

A basic MQMAS experiment requires: RF excitation of the multiple quantum coherences p; evolution of these coherences during time t_1; reconversion of the coherences into the observable $p = -1$ coherence; and detection of the resultant signal as a function of time t_2. The most common pulse sequence for achieving this, and the one used in this thesis, is the z-filtered 3QMAS shown in Figure 3.3. The first non-selective pulse excites all coherences and after time t_1 the second pulse converts them back to $p = 0$. Both are high power (hard) pulses to optimise the excitation/reconversion efficiency. After a short duration, the third pulse (z-filter), which is a weaker (soft) pulse to allow accurate excitation of the CT only,

converts the non-observable $p = 0$ coherence into the observable coherence, allowing detection. The 3-pulse *z*-filter sequence allows simultaneous excitation of both coherence pathways $0 \rightarrow \pm p \rightarrow 0 \rightarrow -1$, compared to a 2-pulse experiment which requires consecutive experiments for the excitement of both the $0 \rightarrow -p \rightarrow -1$ and $0 \rightarrow +p \rightarrow -1$ pathways. Selection of the desired coherence pathway ($p = \pm 3$ for 3QMAS; see Figure 3.3) is achieved by phase cycling.[18]

3.1.4. Variable Offset Cumulative Spectroscopy

Occasionally, NMR lineshapes are so broad that the frequency range cannot be covered by the excitation bandwidth from a single pulse, as a sufficiently large frequency bandwidth would require an unachievably short pulse duration (Equation 2.13). In these cases, the simple solution is to perform multiple NMR experiments at incremental frequencies across the required frequency range. The sum of the resultant spectra provides a cumulative spectrum that accounts for the entire lineshape. This technique is called variable offset cumulative spectroscopy (VOCS). To ensure that the entire lineshape is uniformly excited the pulse profiles must remain constant, with frequency increments that are less than the excitation bandwidth of an individual pulse. The downside to this technique is the necessary retuning of the probe before each frequency stepped acquisition.[27]

3.2. Other Analytical Techniques

In addition to solid state NMR this thesis has made use of a few other analytical techniques. A brief description of each is given.

3.2.1. Powder X-ray Diffraction

X-Ray diffraction (XRD) is a useful analytical technique for the determination of crystalline structures. A crystal lattice can act as a set of 3D diffraction gratings for an X-ray beam of similar wavelength to the spacing of planes in the lattice. Constructive interference of the diffracted X-rays upon interaction with the crystalline sample produce a diffraction pattern. Detection and analysis of the diffraction pattern provides information about the spacing of the planes and, therefore, the crystal structure can be inferred.

Constructive interference of the diffracted rays occurs when conditions satisfy Bragg's law

$$n\lambda = 2d\sin\theta \qquad\qquad 3.10$$

where $n\lambda$ are integer multiples of the incident x-ray wavelength, d is the planar spacing and θ is the angle between the incident X-ray and the diffraction plane. The XRD experiment fires a monochromatic X-ray beam at the sample and the detector, at 2θ, records the intensity of the diffracted X-rays. In a powdered sample, every possible crystalline orientation is represented equally. Therefore, by scanning over a range of 2θ angles, all possible diffraction directions of the lattice are attained. The resultant diffractogram plot (intensity versus 2θ), maps out all the lattice spacings, d, in the crystal structure. Hence, the crystal structure can be determined.[11]

3.2.2. Pair Distribution Function XRD

The Bragg peaks in an X-ray diffractogram accurately describe long-range order. Therefore, powder XRD provides accurate structural determination on highly periodic (small unit cell) crystals. However, in more disordered materials the lower periodicity (large unit cells) reduces the long-range order. Instead, the short-range order can be examined to provide the local atomic structure. The short-range order is present in the broad, less well-defined features at high diffraction angles in the diffractogram. By analysing the complete powder XRD pattern, which contains both the Bragg scattering and diffuse scattering data the local structure can be determined.

By Fourier transforming the total diffraction pattern, the pair distribution function (PDF) can be obtained. The PDF function gives the probability of finding atomic pairs separated by a distance r. To describe it, we first must consider the momentum transfer Q of the scattered X-rays which is given by

$$Q = \frac{4\pi}{\lambda}\sin\theta \qquad\qquad 3.11$$

where 2θ is the scattering angle. The total diffraction pattern is then described by the normalised structure function $S(Q)$, which Fourier transformed provides the PDF function $G(r)$ as

$$G(r) = \frac{2}{\pi}\int_0^\infty Q[S(Q) - 1]\sin(Qr)\,dQ\,. \qquad\qquad 3.12$$

When $G(r)$ is plotted it presents peaks at r values corresponding to the interatomic distances. Hence, the PDF can be used for structural determination. To ensure sufficient spatial

resolution for the study of local atomic structure, the diffraction data must be performed using high energy X-rays and with very good counting statistics. Therefore, the majority of PDF XRD experiments are performed using synchrotron X-rays.[28]

3.2.3. Magnetic Susceptibility Measurements

A magnetic property measurement system (MPMS) can be used to determine the magnetic susceptibility of a material. When introduced to an applied magnetic field H, all materials are magnetically polarised due to permanent or induced magnetic dipole moments resulting from the behaviour of the electrons and nuclei (see Chapter 2.1) in the material. The magnetisation M is the measure of the polarisation and is related to the applied field by

$$M = \chi H.$$
$$3.13$$

where χ is the magnetic susceptibility of the material. The magnetic susceptibly, therefore, defines the magnetic properties of the material. The total flux density, B, in the material is then given by

$$B = H + 4\pi M$$
$$3.14$$

in Gaussian cgs units (the preferred unit system of magnetic properties). Notice the different notation used for fields in the discussion of magnetic properties compared to NMR.

The magnetisation, M, of a material is measured by the MPMS and therefore the susceptibility, χ, can be determined. The MPMS achieves this by moving the sample through a coil of superconducting wire, in the applied field H produced by a superconducting magnet. The changing flux density B at the coil, due to the magnetisation of the material, induces a current in the coil. The current is detected by a superconducting quantum interface device (SQUID) which is protected from the strong fields by a superconducting magnetic shield. The SQUID acts as a highly linear current-to-voltage converter. Variations in the SQUID output voltage provide a highly accurate measurement of the material's magnetisation.

For some materials, the magnetic susceptibility, χ, is dependent on H. To account for this, χ is determined by measuring M over a range of H values. In paramagnetic and diamagnetic materials M is linearly dependent on H. An applied magnetic field in a diamagnetic material induces a field in the opposite direction and, hence, such materials have a negative χ value. Conversely, paramagnetic materials produce an induced field in the direction of the applied field and have positive χ values. Diamagnetic susceptibility is almost completely independent of temperature. The temperature dependence of the paramagnetic susceptibility

is different for the several types of paramagnetism. In general, the paramagnetic susceptibility is reduced at higher temperatures.[29]

4

The Development of ^{105}Pd Solid State NMR Methodology and its Application to Pd Catalyst Systems

4.1. Background

The accessible oxidation states and versatility of palladium, make it a desirable option in many technological applications such as electronics, dentistry and catalysis. The most predominant use of palladium is in automobile catalytic converters, where it catalyses the oxidation of CO.[30-31] Palladium is also known to be one of the most active and selective alkyne hydrogenation catalysts, with applications in the petrochemical and food industries.[32] In the pharmaceutical and fine chemical synthesis industries, palladium catalysts play a significant role through the catalysis of carbon-carbon coupling and a range of hydrogenation reactions.[33] Additionally, palladium catalysts are popular in the development of hydrogen fuel cell materials.[34]

The functional demands on modern catalysts require highly accurate refinements of their proposed crystal structures. A small structural change can significantly alter the function of a catalyst. Most catalytic applications of Pd involve the use of organometallic Pd systems, or the deployment of pure or alloyed Pd metal nanoparticles on various substrates.[31-34] This renders characterisation by conventional techniques, such as X-ray diffraction (XRD), somewhat problematic as these systems often lack the effective long-range order that enables these measurements. The short-range, element specific nature of solid state NMR provides a useful alternative that can readily probe structural aspects of materials that lack any long-range periodicity. It is an excellent probe for characterising disordered systems, and exhibits great complementarity with other techniques such as diffraction, for long range order information, and vibrational spectroscopies, for motional information.

No thorough NMR investigation of the ^{105}Pd nucleus in diamagnetic materials has ever been undertaken and the field of ^{105}Pd solid state NMR is undeveloped and unexplored. The dearth of ^{105}Pd solid state NMR studies is predominantly a consequence of the extremely large

Isotope	I	Nat. Abundance /(%)	γ /(MHzT^{-1})	Q /(fm^2)
^{105}Pd	$^5/_2$	22.23	1.95	66.0
^{7}Li	$^3/_2$	92.58	16.55	−4.0
^{11}B	$^3/_2$	80.42	13.66	4.1
^{14}N	1	99.63	3.08	2.0
^{17}O	$^5/_2$	0.04	5.77	−2.6
^{23}Na	$^3/_2$	100.00	11.26	10.4
^{27}Al	$^5/_2$	100.00	11.09	14.7
^{35}Cl	$^3/_2$	75.53	4.17	−8.2
^{39}K	$^3/_2$	93.10	1.99	5.85

Table 4.1 The isotope, spin I, natural abundance, gyromagnetic ratio γ and quadrupole moment Q of popular quadrupolar NMR nuclei.

quadrupole moment (Q = 66 fm^2), low gyromagnetic ratio (γ = 1.95 MHzT^{-1}), and modest natural abundance (22 %) of the ^{105}Pd nucleus.[35] The NMR parameters of the ^{105}Pd nucleus are displayed in Table 4.1 and are compared to other popular quadrupolar NMR nuclei.[35]

As shown, ^{105}Pd has one of the largest Q values in the NMR periodic table which can cause extreme quadrupole broadening even in systems with small EFGs. For example, by inputting these values into Equation 1.45, the solid state NMR observation of the central transition of a ^{105}Pd complex is determined to be ~115 times broader than a ^{27}Al complex in the same environment. Unfortunately, the meagre γ and low natural abundance of ^{105}Pd only further inhibits matters. Even if the NMR line shape of a ^{105}Pd and a ^{27}Al nucleus had the same breadth, Equation 2.35 determines that the ^{105}Pd nucleus would require ~700,000 times the number of transients to achieve a similar SNR.

4.1.1. Literature Review

To date, the difficulty of measuring ^{105}Pd NMR has hampered studies to only very high-symmetry Pd environments generally in beneficial conditions, such as solutions or very low temperatures (< 10 K).

Most of the measurements in the literature occured on cubic Pd metal. The first ^{105}Pd NMR measurement was achieved by Seitchik, Gossard and Jaccarino[36] in 1964, where they achieved a continuous wave NMR measurement of Pd metal at temperatures of 1.4 to 300 K. This provided the first measurement of the Pd Knight shift as -3.1 ± 0.4 %. In 1966, Narath, Fromhold and Jones[37] measured the ^{105}Pd nuclear relaxation rates for Pd metal at temperatures of 1 - 4 K and this work was later expanded to include measurements of the longitudinal relaxation rate at temperatures of 4 - 300 K (Takigawa and Yasuoka[38] in 1981). By 1973 the scientific community's interest in palladium hydride pushed Brill and Voitlander[39] to measure the ^{105}Pd Knight shift of α phase palladium hydride at 75 K.

In 1984, Fedotov and Likholobov[40] claimed to present the first direct observation of ^{105}Pd NMR in solution. Their measurements were performed on H_2PdCl_6 in concentrated acid. However, work by Brevard and Granger[41] reported a ^{105}Pd solution NMR measurement on K_2PdCl_6 (D_2O) in 1981.

In 1977 the first solid state ^{105}Pd NMR measurement on intermetallic Pd was reported by Matsuda, Kohori and Kohara.[42] They performed ^{105}Pd NMR measurements on the superconductor UPd_2Al_3, albeit at 4.2 K. Since then no direct measurement of ^{105}Pd NMR has occurred. In 2004, Rüegger[43] detected indirect spin-spin coupling of ^{105}Pd nuclei to ^{31}P using ^{31}P NMR on Pd(II) complexes. This led to the successful determination of the *J*-coupling constants between ^{105}Pd and ^{31}P.

4.2. Chemical Shift Reference

A first step in the development of a methodology to study an under-developed NMR-active nucleus is to determine an appropriate isotropic chemical shift reference; this is to standardize all future ^{105}Pd chemical shift measurements. The IUPAC[35] recommends a ^{105}Pd reference of K_2PdCl_6 in a saturated D_2O solution presumably following the report of Brevard and Granger[41]. However, the low solubility of this complex in aqueous solutions limits its use as a ^{105}Pd chemical shift reference, as a higher concentration solution is preferred to maximise Pd content.

Conversely, this report proposes the solution $H_2Pd(IV)Cl_{6(aq)}$, which was examined by Fedotov and Likholobov[40] and boasts octahedral Pd point symmetry, as an appropriate
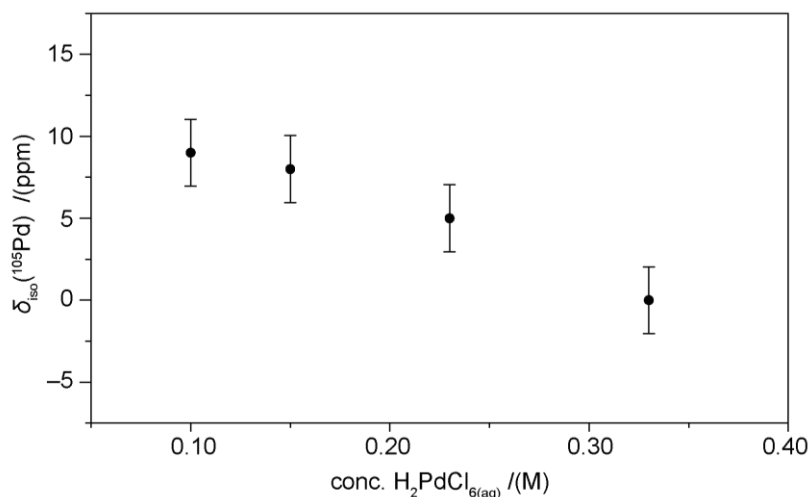
Figure 4.1 The [105]Pd NMR chemical shift of $H_2PdCl_{6(aq)}$ at various concentrations acquired at 7.05 T.

chemical shift reference. However, their reported synthetic route facilitates the fast reduction to $H_2Pd(II)Cl_4$ (planar Pd point symmetry), an observation supported by many industrial processes and extractions at low pH.[44] This species yields a very broad [105]Pd resonance in solution giving limited resolution and accuracy as a chemical shift standard. This study suggests a 0.33 M solution of H_2PdCl_6 in *aqua regia* as the [105]Pd primary chemical shift reference following the synthetic route described by

$$Pd_{(s)} + 4HNO_{3(aq)} + 6HCl_{(aq)} \rightarrow H_2PdCl_{6(aq)} + 4NO_{2(aq)} + 4H_2O_{(l)}. \qquad 4.1$$
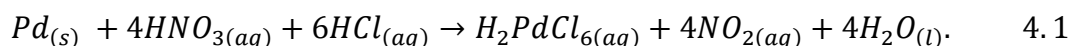
To synthesize the proposed reference 0.125g of Pd metal sponge was dissolved in 2 mL of concentrated (70 %) nitric acid. Then 2 mL of concentrated (36 %) hydrochloric acid was added dropwise producing a dark red solution. An excess of oxidizing acid is required to hinder the reduction of $H_2Pd(IV)Cl_6$ to $H_2Pd(II)Cl_4$. As demonstrated in Figure 4.1, the [105]Pd chemical shift of $H_2PdCl_{6(aq)}$ exhibits a minor concentration dependence. Despite the shift variation decreasing at lower concentrations of ≤ 0.15 M, the relatively high concentration of 0.33 M was selected as the proposed reference to maximise the Pd content and therefore minimise experimental time required.

Furthermore, the proximity to the [39]K ($\gamma = 1.99$ MHzT^{-1}) solid state reference, $KCl_{(s)}$, is very convenient. It allows the use of $KCl_{(s)}$ as an external secondary reference for [105]Pd NMR, eliminating the repetitive handling of *aqua regia* solutions in solid state NMR probes, while requiring only minimal retuning of the NMR probe upon switching observation. The utility of both $H_2PdCl_{6(aq)}$ and $KCl_{(s)}$ referencing approaches is shown in Figure 4.2, which demonstrates the consistency of these shifts across multiple B_0 field strengths. The cubic
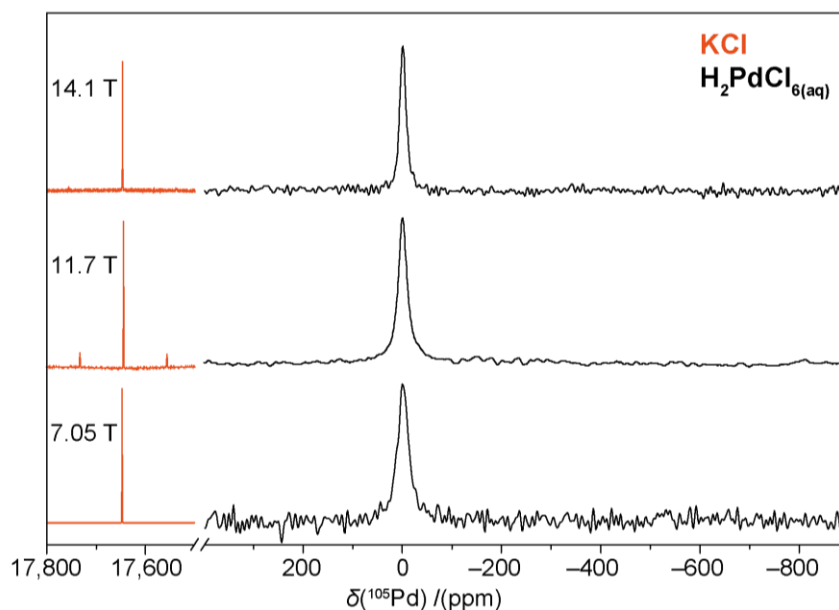
Figure 4.2 The ^{105}Pd MAS (3 KHz) NMR spectra of KCl$_{(s)}$ in orange and 0.33 M H$_2$PdCl$_{6(aq)}$ in black at 14.1 T, 11.7 T and 7.05 T.

point symmetry of K in the KCl$_{(s)}$ lattice rigorously restricts the ^{39}K quadrupolar coupling constant (C_Q) to zero[45] thus creating a field independent reference in the solid state; this has been verified against KCl$_{(aq)}$.[46-47] The H$_2$PdCl$_{6(aq)}$ solution reference shift was set to 0.0 ppm and the ^{39}K resonance of KCl$_{(s)}$ was recorded at a shift position of 17,647 ppm at three fields (14.1 T, 11.7 T and 7.05 T). The field independence of the ^{105}Pd chemical shift confirms that H$_2$PdCl$_{6(aq)}$ does not have a measurable ^{105}Pd C_Q, as observed in some solution species which possess large quadrupole moments Q.[48]

4.3. Experimental

4.3.1. NMR Measurements

Both the static and MAS NMR experiments in this study were performed at room temperature across a range of different magnetic field strengths (B_0) using Bruker Avance II+-600 (14.1 T), Bruker Avance III-500 (11.7 T), Bruker Avance HD-400 (9.40 T), Bruker HD-300 (7.05 T) and Varian Infinity+-300 (7.05 T) spectrometers. All NMR data was processed using *TOPSPIN*. Simulations of Gaussian/Lorentzian lineshapes were performed with *dmfit*.[49]

Solid state NMR of metallic materials has several complications due to the conductivity of the samples. Firstly, the skin effect in conductors causes an exponential decay in the intensity

EM Frequency/(MHz)	Skin Depth /(μm)
26.6	31.7
13.3	44.8

Table 4.2 The skin depth of palladium at the EM frequencies equal to v_0 (^{105}Pd) at 14.1 and 7.05 T.

of EM radiation the deeper it penetrates the material. Therefore, the conducting volume of the sample needs to be small enough to ensure that the RF radiation is exciting nuclei throughout the sample, rather than just the surface. The skin depth δ is defined as the depth below the surface when the intensity of the radiation has fallen to $^1/_e$ of its initial value, and is given for conductors in Equation 4.2 where ρ is the resistivity, v is the EM frequency, and μ is the magnetic permeability. The skin depth for Pd metal at a couple of relevant frequencies is stated in Table 4.2, using known values of ρ and μ.[50-51]

$$\delta = \sqrt{\frac{\rho}{\pi v \mu}} \qquad\qquad 4.2$$

Particles with a radius below the skin depth were generally used in this investigation, however to prevent agglomeration of these particles into a mass larger than the skin depth, an insulator was mixed in with the metal. The insulator diluent has the added benefit of reducing the necessary re-tuning of an NMR probe when a conducting material is placed inside the coil. Regardless, care must be taken to ensure precise tuning when changing between metallic samples. Any conducting materials examined in this work were all diluted with 50-75% $NaCl_{(s)}$. Additionally, a conductive material is difficult to analyse using MAS due to heating caused by the build-up of eddy currents. Therefore, most metallic NMR measurements in this work were taken under static conditions.

4.3.2. ^{105}Pd Solid State NMR Measurements

All ^{105}Pd NMR experiments at 14.1, 11.7 and 9.40 T were undertaken using a Varian 9.5 mm MAS probe with a low gamma attachment whereas the 7.05 T experiments were completed using a 9.5 mm Otsuka MAS probe. All data was referenced to the proposed standard of $H_2PdCl_{6(aq)}$ ($\delta_{iso} = 0$ ppm) and the neighbouring $KCl_{(s)}$ ($\delta_{iso} = 17,647$ ppm).

Name	Field /(T)	v_0 Range /(MHz)	v_0 Step-size /(MHz)
Pd sponge	14.1 T	26.57 - 26.61	0.02
	7.05 T	13.29 - 13.44	0.03
Pd black	14.1 T	26.57 - 26.61	0.02
	7.05 T	13.23 - 13.38	0.03
Pd PVP16	14.1 T	26.57 - 26.69	0.02
Pd/C	14.1 T	26.58 - 26.64	0.02
Dehydrogenated Pd	14.1 T	26.60 - 26.64	0.02

Table 4.3 Details of the VOCS [105]Pd static NMR experiments performed on metallic samples.

The [105]Pd NMR experiments on non-metallic samples were performed at 14.1 T (v_0 ([105]Pd) = 27.49 MHz), 11.7 T (v_0 ([105]Pd) = 22.93 MHz), 9.40 T (v_0 ([105]Pd) = 18.30 MHz) and 7.05 T (v_0 ([105]Pd) = 13.75 MHz) employing an MAS frequency of ~3 KHz where appropriate. A $\pi/2$ pulse length was determined on $H_2PdCl_{6(aq)}$ resulting in a selective $\pi/4$ pulse length of 10, 6, 5 and 4 μs at 14.1, 11.7, 9.40 and 7.05 T respectively. A ($\pi/4$)-τ-($\pi/2$) echo sequence was utilised to diminish ringing effects present at low frequencies. A recycle delay of 0.1 s was used throughout and a rotor synchronised τ period of 323, 327, 659 and 330 μs was used for the 14.1, 11.7, 9.40 and 7.05 T experiments, respectively.

The wide line shapes produced by [105]Pd NMR on metallic materials required VOCS (Chapter 3.1.4), to achieve full, uniform excitation. The VOCS frequency range and step-size is dependent on the line shape characteristics of each sample alongside the experimental parameters used; they are provided in Table 4.3. A solid-echo ($\pi/2$)-τ-($\pi/2$) sequence was utilised to avoid ringing effects present at low frequencies, with $\pi/2$ pulse lengths of 10 and 7.5 μs on the 14.1 and 7.05 T instruments respectively. A recycle delay of 0.01 s was used throughout and a τ period of 30 and 150 μs was used for the 14.1 and 7.05 T experiments respectively. The larger τ period at 7.05 T reflects the greater ringing present in the Otsuka probe.

4.3.3. [39]K and [35]Cl Solid State NMR Measurements

The [39]K NMR experiments at 14.1 T were undertaken using a Varian 9.5 mm MAS probe with a low gamma attachment whereas the experiments at 9.40 T and 7.05 T were completed

using a 9.5 mm Otsuka MAS probe respectively. All data was referenced with respect to KCl$_{(s)}$ (δ_{iso} = 47.8 ppm). The ^{39}K NMR experiments performed at 14.1 T (ν_0 (^{39}K) = 27.97 MHz), 9.40 T (ν_0 (^{39}K) = 18.61 MHz) and 7.05 T (ν_0 (^{39}K) = 13.98 MHz) employed an MAS frequency of 3 KHz throughout. A $^{\pi}/_2$ pulse length was determined on KCl$_{(s)}$ resulting in a selective $^{\pi}/_6$ pulse length of 3, 3 and 2 μs at 14.1, 9.40 and 7.05 T respectively. The single-pulse experiments used a recycle delay of 5 s.

The ^{35}Cl NMR experiments were performed at 11.7T (ν_0 (^{35}Cl) = 49.00 MHz) with an MAS frequency of 12 KHz. The ^{35}Cl NMR experiments were completed using a Bruker 4 mm HX MAS probe with all data referenced with respect to NaCl$_{(s)}$ (δ_{iso} = −46 ppm). A $^{\pi}/_2$ pulse length was determined on NaCl$_{(s)}$ resulting in a selective $^{\pi}/_4$ pulse length of 1 μs being used in the single-pulse experiments, with a recycle delay of 10 s.

4.3.4. ^{1}H, ^{11}B and ^{7}Li Solid State NMR Measurements

The ^{1}H NMR experiments were performed at 14.1 T (ν_0 (^{1}H) = 600.00 MHz) with an MAS frequency of 12 KHz where appropriate. The experiments were completed using a Bruker 4 mm HX MAS probe with all data referenced with respect to alanine$_{(s)}$ (C$_3$H$_7$NO$_2$; δ_{iso} = 1.1, 3.5, 8.5 ppm). A $^{\pi}/_2$ pulse length was determined on alanine$_{(s)}$ resulting in a pulse length of 2.5 μs being used in the single-pulse experiments, with a recycle delay of 3 s.

The ^{11}B NMR experiments were performed at 14.1 T (ν_0 (^{11}B) = 192.50 MHz) with an MAS frequency of 12 KHz. The experiments were completed using a boron-free Varian 4 mm HXY MAS probe with all data referenced with respect to NaBH$_{4(s)}$ (δ_{iso} = −42.06 ppm). A $^{\pi}/_2$ pulse length was determined on NaBH$_{4(s)}$ resulting in a selective $^{\pi}/_4$ pulse length of 2.6 μs being used throughout, with a recycle delay of 0.1 s for the single-pulse experiments. The saturation recovery experiments used 300 pulses in the saturation train with a delay of 30 μs.

The ^{7}Li NMR experiments were performed at 11.7 T (ν_0 (^{11}B) = 194.32 MHz) with an MAS frequency of 30 KHz. The experiments were completed using a Bruker 2.5 mm HX MAS probe with all data referenced with respect to LiCl$_{(s)}$ (δ_{iso} = −0.77 ppm). A $^{\pi}/_2$ pulse length was determined on LiCl$_{(s)}$ resulting in a selective $^{\pi}/_4$ pulse length of 2.25 μs being used throughout, with a recycle delay of 600 s for the single-pulse experiments. The saturation recovery experiments used 200 pulses in the saturation train with a delay of 45 μs.

4.3.5. GIPAW-DFT Calculations

Density functional theory (DFT) calculations were performed by G.J. Rees (University of Warwick) using the *CASTEP* 16 code with the ultrasoft pseudopotential approximation.[52] The generalized gradient approximation (GGA) was employed and adjacent geometry optimisation calculations were performed on all systems.[53] NMR parameter calculation (δ_{iso}, C_Q, η_Q) invoked the gauge included projector augmented-wave (GIPAW)-DFT method. The GIPAW-DFT calculations were performed with a 2x2x2 k-point grid and a kinetic energy cut-off of 1400 eV.

4.3.6. Powder XRD

XRD patterns were measured on a Panalytical X-Pert Pro MPD diffractometer using Cu $K_{\alpha 1}$ radiation ($\lambda = 1.5406$ Å) at ambient temperature. Scans were between 10 - 70° 2θ for the Pd complexes and 30 - 90° 2θ for the metallic Pd samples. Step sizes varied depending on the timescales required for signal acquisition. XRD patterns were fitted using Rietveld refinement where appropriate.

4.3.7. Pair Distribution Function XRD

Total x-ray scattering experiments were performed by D.S. Keeble on XPDF (beamline I15-1) at Diamond Light Source (Harwell Science and Innovation Campus, UK). Samples were packed into 1 mm borosilicate capillaries and were illuminated with photons of energy 78.34 keV ($\lambda = 0.1583$ Å). The scattered intensity was acquired on a Perkin Elmer 1611 CP3, calibrated against a CeO_2 standard and integrated in DAWN.[54] The integrated 1D scattering patterns were used directly for Rietveld refinement and were converted to pair distribution functions in GudrunX,[55] while the structural refinements against both the real and reciprocal space data were performed in TOPAS Academic.[56]

4.3.8. Magnetic Susceptibility Measurements

Magnetic susceptibility measurements were performed on a Quantum Design MPMS 5S SQUID Magnetometer. Powder samples were packed into gel capsules and measurements were performed at temperatures of 300 and 5 K and with magnetic fields of 0 to 50,000 Oe. Gaussian cgs units are used with magnetic field strength H in Oe, (mass) magnetisation M_{mass} in emug^{-1} and (mass) susceptibility χ_{mass} in emug^{-1}.

4.3.9. Transmission Electron Microscopy

Transmission electron microscopy (TEM) analysis was used to determine particle sizes of the Pd nanoparticles. Samples were prepared for TEM by sonicating the nanoparticles in ethanol until fully dispersed. The suspension was then placed onto a holey carbon coated Cu grid and dried. Different microscopes were used depending on the location of the experimentation (University of Warwick/ Johnson Matthey Technology Centre/ University of Oxford).

4.4. High Symmetry Palladium Complexes

Once a chemical shift reference has been established for a burgeoning NMR nucleus, the next step is to develop an idea of its chemical shift range by examining a variety of compounds. Three cubic hexa-halogen palladates with octahedral Pd point symmetry (see Figure 4.3) were chosen as model complexes for this initial ^{105}Pd solid state NMR study: $(NH_4)_2Pd(IV)Cl_6$, $K_2Pd(IV)Cl_6$ and $K_2Pd(IV)Br_6$. These complexes are commercially available (Alfa Aesar) and have relatively high Pd contents which will keep experimental
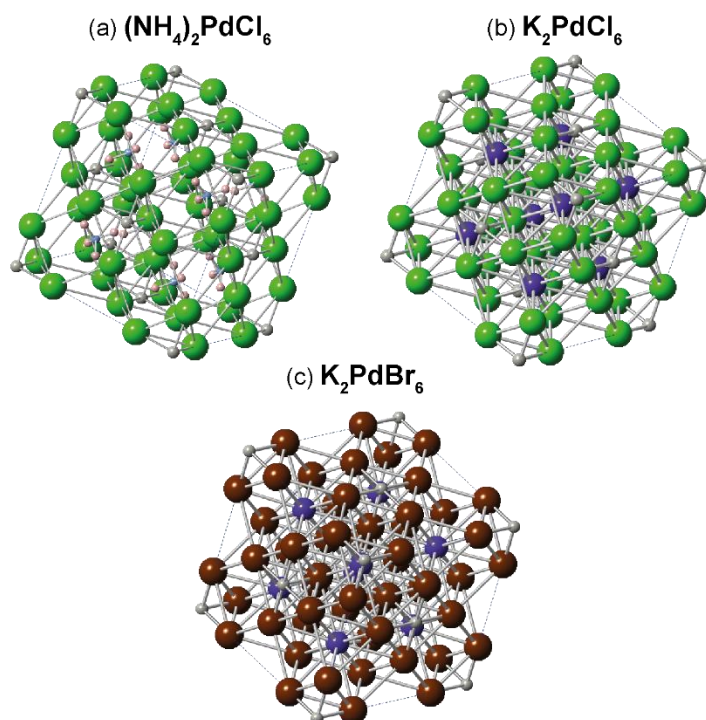
Figure 4.3 The crystal structures of (a) $(NH_4)_2PdCl_6$, (b) K_2PdCl_6 and (c) K_2PdBr_6 giving the relative atomic positions of Pd (grey), Cl (green), Br (burgundy), N (blue), H (pink) and K (purple).

time minimal. Most importantly, the difficult quadrupolar interaction should be negligible due to the highly symmetrical environment.

4.4.1. ^{105}Pd NMR Chemical Shift Range

The ^{105}Pd solid state NMR spectra of the three complexes are displayed in Figure 4.4 and reveal the sensitivity of the ^{105}Pd NMR chemical shift to changes in the Pd environment. The change in anion from $[PdCl_6]^{2-}$ to $[PdBr_6]^{2-}$ produces a large ~800 ppm shift to lower frequency. This greater shielding of the Pd nucleus in K_2PdBr_6, is due to the lower
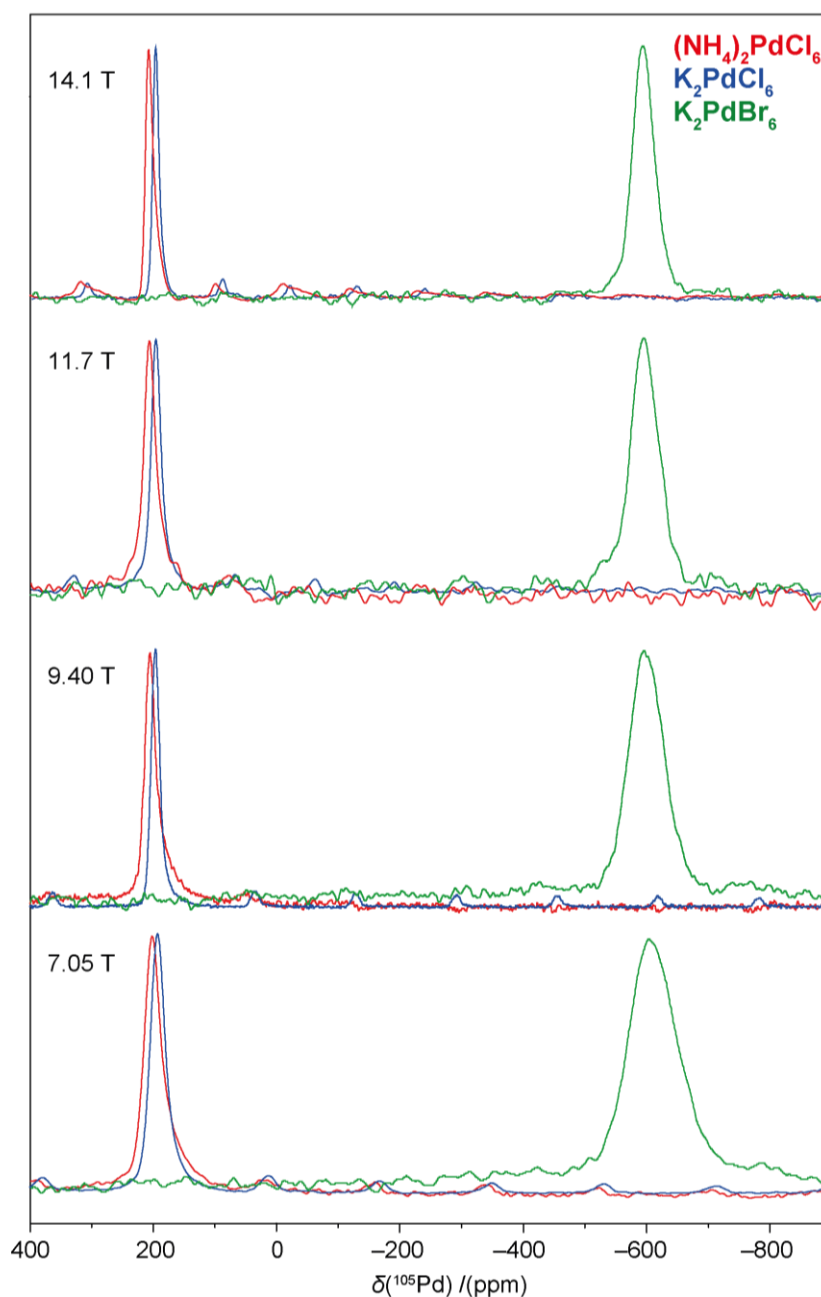
Figure 4.4 The multifield ^{105}Pd MAS (3 KHz) NMR spectra of the three inorganic palladium complexes $(NH_4)_2PdCl_{6(s)}$ (red), $K_2PdCl_{6(s)}$ (blue) and $K_2PdBr_{6(s)}$ (green) acquired at 14.1 T, 11.7 T, 9.40 T and 7.05 T.

53

electronegativity of the heavier halogen.[57] Changing the cation in the second coordination sphere from K^+ to $(NH_4)^+$, also produces a significant shift of ~10 ppm towards higher frequency. This sensitivity to positional substitution of next nearest neighbours is very promising for the use of ^{105}Pd solid state NMR as an analytical tool for structural determination.

4.4.2. Evidence of a Quadrupolar Interaction in the ^{105}Pd NMR Results

A closer look at the line shapes of the $(NH_4)_2PdCl_6$ and K_2PdCl_6 resonances in Figure 4.4 reveals an asymmetric tailing to lower frequencies. This asymmetry, instead of the expected Gaussian/Lorentzian line shape, is indicative of a second order quadrupolar interaction in a disordered system, as detailed in Chapter 1.4.1.[58-59] To investigate further, the ^{105}Pd NMR spectra for the three complexes was compared across multiple fields: 14.1 T, 11.7 T, 9.40 T
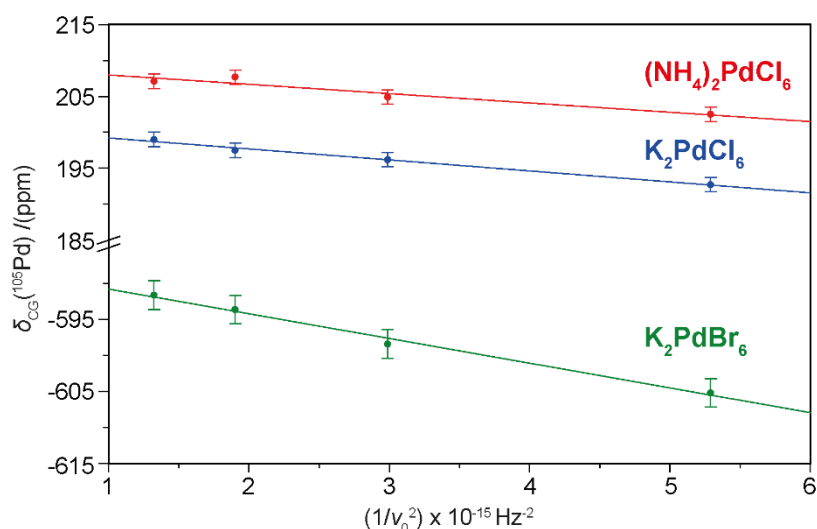
Figure 4.5 The $\delta_{CG}(^{105}Pd)$ of $(NH_4)_2PdCl_6$ (red), K_2PdCl_6 (blue) and K_2PdBr_6 (green) against the inverse square of the Larmor frequency v_0.

Complex	δ_{iso} (exp.) /(MHz)	P_Q (exp.) /(MHz)	P_Q (calc.) /(MHz)
$(NH_4)_2PdCl_6$	209.3 ± 0.9	0.47 ± 0.05	0.00
K_2PdCl_6	200.7 ± 0.3	0.50 ± 0.02	0.00
K_2PdBr_6	-585.0 ± 1.0	0.81 ± 0.05	0.00

Table 4.4 Experimental (NMR) and calculated (*CASTEP*) values of the isotropic shift and quadrupolar product of the three Pd complexes.

and 7.05 T. Figure 4.4 shows that the three complexes all present a field dependent chemical shift. As previously discussed in Chapter 1.4.1, a field dependent chemical shift is often due to a second order quadrupolar shift.

By plotting the centre of gravity of each resonance (δ_{CG}) against the inverse square of the Larmor frequency squared (v_0^2) at each field (Figure 4.5), and then applying Equation 1.47, the quadrupolar parameters for each complex can be determined. The complexes $(NH_4)_2PdCl_6$, K_2PdCl_6 and K_2PdBr_6 have small, but certainly not insignificant, quadrupolar products P_Q in the range of 0.47 to 0.81 MHz (Table 4.4; $P_Q = C_Q$, assuming an η_Q of 0). This conflicts with the complexes' reported crystal structures which depict octahedral Pd(IV) centres (see Figure 4.3).[60-61] The high symmetry Pd environment should ensure that there are
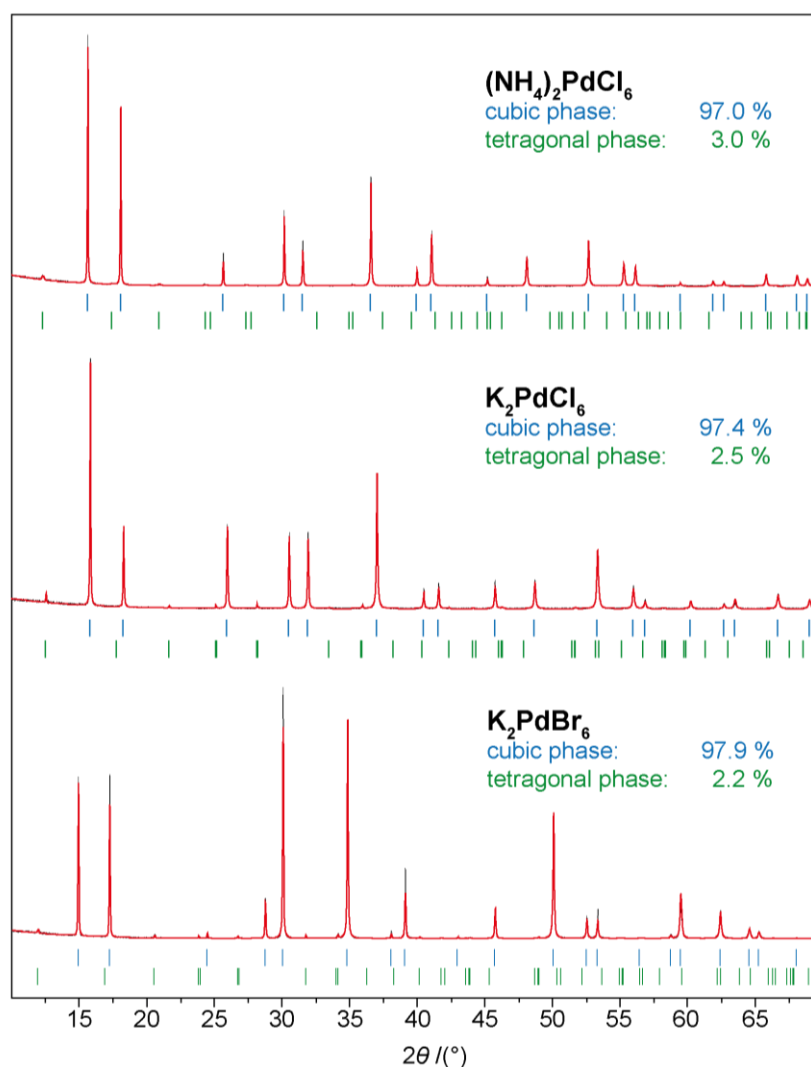
Figure 4.6 The powder XRD patterns for $(NH_4)_2PdCl_{6(s)}$, $K_2PdCl_{6(s)}$ and $K_2PdBr_{6(s)}$ displayed with relative intensities against 2θ. The data is presented with the XRD pattern in black, the Reitveld refinement fitting in red, the cubic *Fm-3m* profile in blue, and the tetragonal *P4/mmm* profile in green.

no EFGs present, as demonstrated by the DFT calculations on these structures, which produced P_Q values of 0.00 MHz (Table 4.4). Disagreement with the published XRD structures suggests that these complexes contain some deviation from the predicted cubic structure.

The samples were tested with powder XRD to verify their high purity. The Rietveld refinement fitting of the patterns for each sample confirmed the structure as the cubic *Fm-3m* phase, as shown in Figure 4.6. Each of the samples contain a small impurity (2 - 3 %) of their respective tetragonal *P4/mmm* phases: $(NH_4)_2Pd(II)Cl_4$, $K_2Pd(II)Cl_4$ and $K_2Pd(II)Br_4$. It is unlikely that these impurity phases are causing the quadrupolar interaction observed in the ^{105}Pd NMR spectra. The square planar Pd symmetry of the tetrahalides would present a significant EFG and, therefore, an extremely broad NMR resonance that is presumed to be undetectable by these measurements.

However, to ensure that the tetrahalide impurities had no effect on the ^{105}Pd NMR spectra, K_2PdCl_6 was washed with *aqua regia*. Stirring the powder into an *aqua regia* solution for 30 minutes before filtering, washing and drying will remove/oxidise any of the soluble $K_2Pd(II)Cl_4$, leaving only the insoluble K_2PdCl_6. The ^{105}Pd MAS NMR spectra of this "washed" sample is compared to the original sample in Figure 4.7(a, b). There is no discernible difference between the two spectra, indicating that the tetrahalide impurities present in the complexes are not the cause of the observed quadruple interactions. Additionally, Figure 4.7(c) compares the MAS and static ^{105}Pd NMR of K_2PdCl_6 to rule out
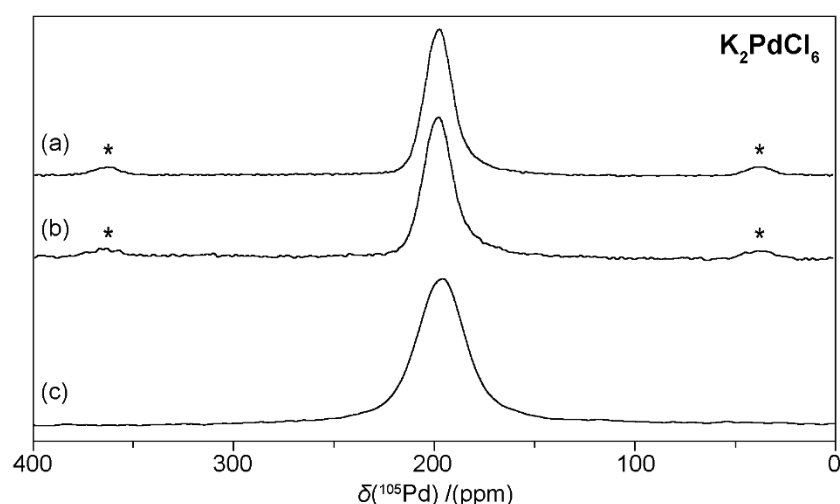
Figure 4.7 The ^{105}Pd NMR spectra acquired at 9.40 T of (a) unmodified $K_2PdCl_{6(s)}$ and (b) *aqua regia* washed $K_2PdCl_{6(s)}$ under MAS (3KHz) alongside (c) unmodified $K_2PdCl_{6(s)}$ under static conditions. Spinning sidebands are marked by an asterix.

varying temperatures due to MAS as an alternative cause of the different chemical shifts at each field. The determined shifts of $\delta_{CG} = 197 \pm 2$ ppm ($\delta_{iso} = 200.7 \pm 0.3$ ppm/P_Q value of 0.50 MHz) from both conditions confirms that the observed field-dependent behaviour of the resonance is a second-order quadrupole contribution.

4.4.3. ^{39}K and ^{35}Cl Solid State NMR

The K containing complexes, K_2PdCl_6 and K_2PdBr_6, were investigated with multi-field ^{39}K MAS NMR. The spectra, shown in Figure 4.8(a), display single narrow resonances at $\delta_{iso} = -10.3 \pm 0.5$ ppm and $\delta_{iso} = -16.4 \pm 0.5$ ppm for K_2PdCl_6 and K_2PdBr_6 respectively. Figure 4.8(b) reveals that the ^{39}K chemical shifts do not exhibit a field dependence; the less substantial ^{39}K quadrupole moment does not produce a large enough P_Q to influence the shift position by a measurable amount at accessible magnetic fields. However, the spinning sideband manifolds, highlighted in the ^{39}K spectra, indicate the presence of non-zero EFGs at the K site.
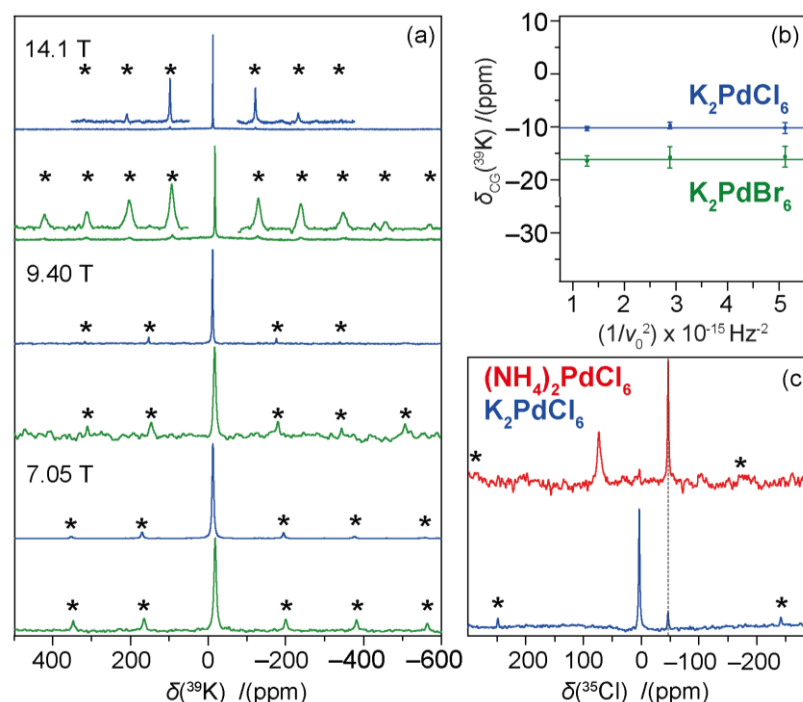
Figure 4.8(a) The ^{39}K MAS (3 KHz) NMR spectra of $K_2PdCl_{6(s)}$ and $K_2PdBr_{6(s)}$, in blue and green respectively, acquired at 14.1 T, 9.40 T and 7.05 T. Spinning sidebands are marked by an asterisk and have been enlarged for the 14.1 T spectra. (b) The $\delta_{CG}(^{39}$K) of $K_2PdCl_{6(s)}$ in blue and $K_2PdBr_{6(s)}$ in green against the inverse square of the Larmor frequency υ_0. (c) The ^{35}Cl MAS (12 KHz) NMR spectra of $(NH_4)_2PdCl_{6(s)}$ and $K_2PdCl_{6(s)}$, in red and blue respectively, acquired at 14.1 T. The resonance given by the internal $NaCl_{(s)}$ reference is marked with a dashed grey line.

For a nucleus in a perfect cubic environment the quadrupole effects are non-existent; however, "close-to-cubic" local environments will produce quadrupole satellite spinning sidebands. Dislocations, defects and impurities in the material create a discernible quadrupole interaction that produces STs that are detectable once reduced to a spinning sideband manifold, despite not always producing a resolvable quadrupolar NMR line-shape.[2] In fact, it is this phenomenon that allows nominally cubic KBr to be used as the default method of setting the magic angle via ^{81}Br NMR spinning sideband analysis.[62] These quadrupolar spinning sideband manifolds are also observable in the ^{105}Pd NMR data (Figure 4.7(a, b)).

Similarly, the Cl containing complexes, $(NH_4)_2PdCl_6$ and K_2PdCl_6, were investigated with ^{35}Cl MAS NMR as shown in Figure 4.8(c). The spectra present single narrow resonances at $\delta_{iso} = 74 \pm 2$ ppm and $\delta_{iso} = 3.6 \pm 0.8$ ppm for $(NH_4)_2PdCl_6$ and K_2PdCl_6 respectively. The resonances are accompanied by low intensity spinning sideband manifolds giving further credence to the presence of EFGs in the structures.

4.4.4. PDF Analyses

The detection of EFGs in the structures, by the ^{105}Pd NMR studies, suggests the technique is sensitive to some deviation from the perfect cubic structure reported by the literature, that cannot be detected by powder XRD. To find this "deviation", high resolution X-ray PDF analysis was performed on the three Pd complexes.

The real space PDF data and fits are presented in Figure 4.9. The very sharp reflection at just over 2 Å in each fit represents a well-defined rigid PdX_6 (X = Cl, Br) bond. The Pd-X bond lengths are highly uniform and the local symmetry of the octahedral unit is strictly preserved, as reported by the literature.[60] The octahedral hexahalopalladate unit is so well defined that the reflection is, surprisingly, narrower than the resolution of the experiment; hence the truncation artefacts collaring the reflection. Therefore, it is highly unlikely that the deviation from cubic symmetry occurs within the octahedral units.

The modelling of the real space PDF for K_2PdBr_6 required the additional refinement of a large atomic displacement parameter for the K site, exceeding what would be expected for a normal thermal parameter range. This can be seen in the PDF fits by comparing the data for K_2PdCl_6 and K_2PdBr_6. The bond lengths determined from the literature structures are
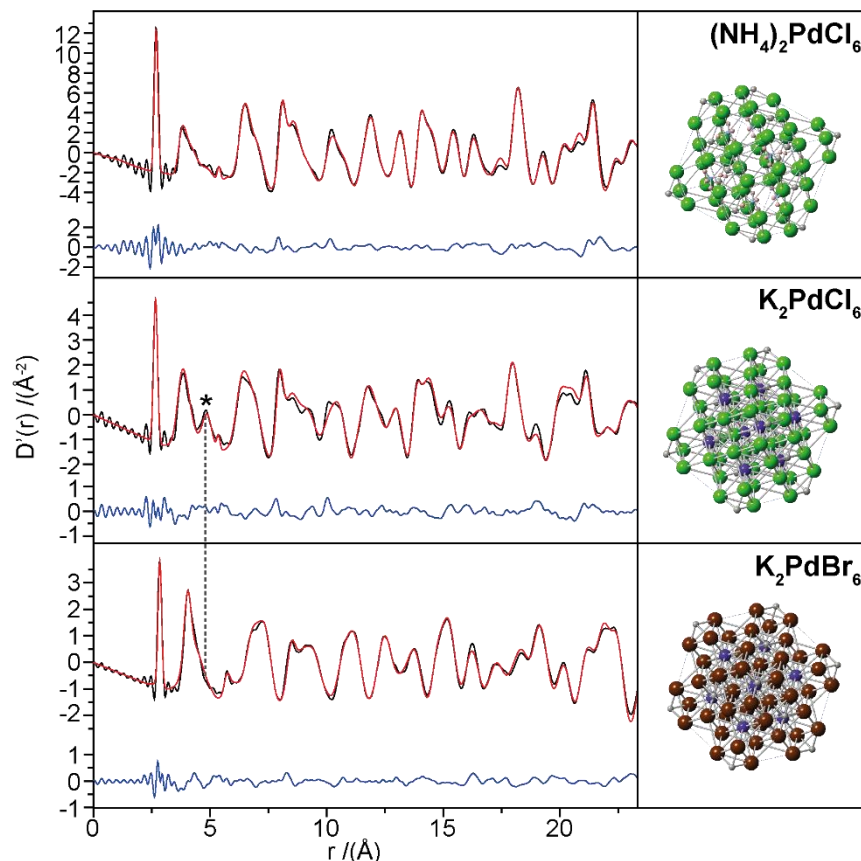
Figure 4.9 Analysis of the X-ray PDF data for $(NH_4)_2PdCl_{6(s)}$ $K_2PdCl_{6(s)}$ and $K_2PdBr_{6(s)}$ with the experimental data in black, the PDF fittings in red and the offset difference curves in blue. The asterix and dashed line mark the K-Pd correlation length present in the K_2PdCl_6 data which is removed by disorder in the K_2PdBr_6 data. Presented alongside are the refined strucures from each fit.

Pair	Bond lengths /(Å)	
	K_2PdCl_6	K_2PdBr_6
Pd-X	2.30	2.46
X-X *intra*	3.26	3.49
K-X	3.43	3.64
X-X *inter*	3.61	3.79
K-Pd	4.20	4.46

Table 4.5 The bond lengths between atomic pairs in the XRD Rietveld refined structures of K_2PdCl_6 and K_2PdBr_6 (X = Cl/Br).

presented in Table 4.5, where X represents the halogen atom (X = Cl/Br).[61] Both contain a narrow Pd-X reflection, as discussed, and then a broader reflection (3 - 4 Å) which

encompasses the following bond lengths: X-X within the octahedral unit, X-X between the octahedral units and K-X. The PDF fit for K_2PdCl_6 then has a reflection at 4.2 Å representing the K-Pd bond length. Importantly, this K-Pd bond length is "missing" from the K_2PdBr_6 PDF fit due to the hypothesized positional disorder on the K (¼, ¼, ¼) positions.

It is noted from Table 4.4 that K_2PdBr_6 exhibits the largest ^{105}Pd EFG of the three complexes ($P_Q = 0.81$ MHz). In contrast, the complexes with lower P_Q, $(NH_4)_2PdCl_6$ and K_2PdCl_6, did not require an atomic displacement parameter on the cation position for accurate fitting. It is therefore suggested that these PDF experiments are sensitive to the larger positional disorder on the K site in K_2PdBr_6, whereas the ^{105}Pd NMR technique is also sensitive to the hypothesized smaller disorder at the cation sites in the chloride complexes.

4.5.   Palladium Metal Particles

As discussed in Chapter 4.1.1, Pd metal is one of the few materials that has previously been investigated with ^{105}Pd solid state NMR. This is due to its *fcc* structure reducing the EFG in the Pd environment to a minimum, similarly to the octahedral Pd complexes. All the previous ^{105}Pd NMR studies on Pd metal examined pure Pd powders with particle sizes > 40 μm.[36-39] Not only does this work provide a more thorough study of ^{105}Pd solid state NMR on Pd metal, but it also studies particle sizes and systems that are more relevant to Pd metal's use in catalysis. The various Pd metal systems that have been investigated are detailed in Table 4.6. Pd black, Pd nanoparticles on carbon and polyvinylpyrrolidone (PVP) stabilised nanoparticles are all commonly used as catalysts.[63-65]

4.5.1. Synthesis

Pd sponge is commercially available from Alfa Aesar with a −100+325 mesh size (44 - 149 μm) and 99.95% purity. The Pd black sample was produced by the Johnson Matthey Technology Centre in Sonning Common, UK. A typical syntheis involves the precipitation of Pd black from a solution of $(NH_4)_2PdCl_6$, formic acid and KOH.[65] The carbon supported Pd nanoparticles were produced by I.T. Ellis from the University of Oxford. The synthesis is described in Chapter 4.7.1 and in greater detail in the thesis of Ellis.[66]

Name	Particle diameter /(nm)	Support	Source
Pd sponge	44 - 149 (10^3)	-	Alfa Aesar
Pd black	20 - 150	-	JMTC[γ]
Pd/C	13 ± 9	C[β]	Oxford
Pd PVP16	16 ± 3	PVP[α]	JMTC[γ]
Pd PVP6	6 ± 5	PVP[α]	JMTC[γ]

Table 4.6 Particle diameter, loading, support type and source of the various Pd metal samples investigated. Particle diameters were determined via TEM analysis.
[α]polyvinylpyrrolidone; [β]carbon black; [γ]Johnson Matthey Technology Centre

The PVP stabilised Pd nanoparticles were synthesized by the author via two different methods to produce the different particle sizes. The methodology for producing Pd PVP16 involves refluxing 40 ml of water, 200 ml of ethylene glycol, 2.432 g of Pd(acac)$_2$ (palladium acetylacetonate), and (palladium acetylacetonate), and 13.34 g of PVP$_{8000}$ (molecular weight = 8,000 gmol^{-1}) for 4 hours at 400 K. The methodology for producing Pd PVP6 is slightly different, refluxing 120 ml of H$_2$O, 104 ml of methanol, 7 ml of 12.1 wt% solution Na$_2$PdCl$_4$, and 6g of PVP$_{8000}$ for 3 hrs at 350 K. The alcohol reduces the Pd(II) complex and the PVP enwraps the Pd nanoparticles before they can agglomerate. Changing the reactants and temperature alters the speed of the decomposition of the Pd(II) complexes allowing different sized particles to be produced. The resultant solutions were then washed with acetone and centrifuged to acquire colloids that produced the Pd nanoparticles upon evaporation.

4.5.2. ^{105}Pd Solid State NMR

As discussed in Chapter 1.3.5, metallic materials have an additional interaction: the Knight shift. In ^{105}Pd NMR of Pd metal the Knight shift is the dominant interaction, despite the strength of its quadrupole moment. The electron configuration of Pd is simplistically described as [Kr]$4d^{10-x}5s^x$ due to its overlapping s and d bands at the Fermi level. Unpaired electrons in the d orbital contribute to the paramagnetic susceptibility of Pd and result in a large K_{cp} component of the Knight shift.[36, 67-68] The negative K_{cp} component is responsible for the very large K of -3.0 ± 0.4 % reported by Seitchik, Gossard and Jaccarino.[36]

The multifield ^{105}Pd NMR spectra of Pd metal sponge and Pd black are presented in Figure 4.10. Both Pd metal samples present with one identical, broad NMR resonance as expected. No quadrupole interaction is observed in either of the metal samples evidenced by the lack
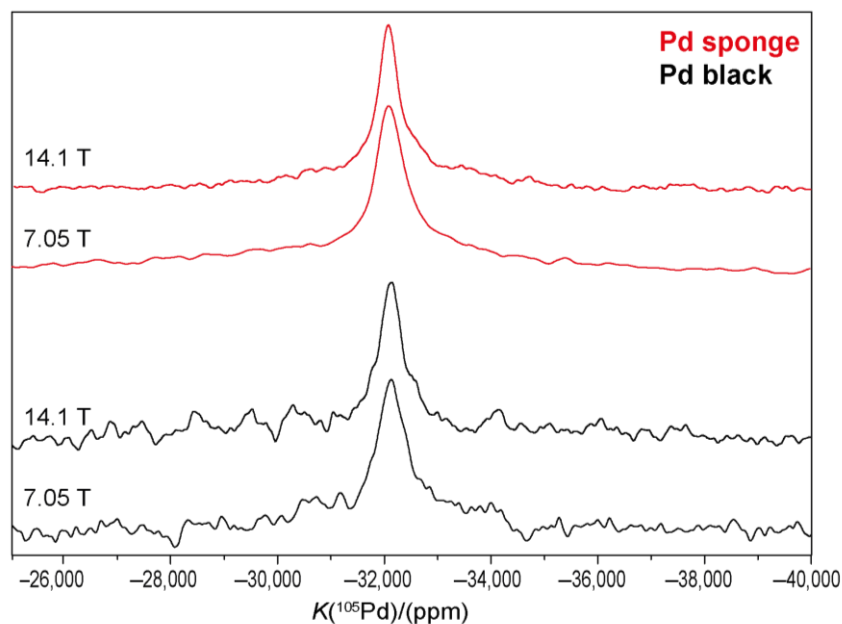
Figure 4.10 The [105]Pd static VOCS NMR of Pd sponge (red) and Pd black (black). at 14.1 T and 7.05 T.

of any field dependence in their shifts. Any quadrupolar shift resulting from the cubic structure will be negligible, at least when overshadowed by the paramagnetic broadening of the Pd metal resonance. The Pd metal sponge gives a more precise K of -3.205 ± 0.006 % (at room temperature), which is corroborated by the Pd black shift and is in agreement with the previously reported value.

The [105]Pd NMR of the Pd metal samples are then compared to the other Pd nanoparticle samples in Similarly, it is believed that the reduced particle size in the Pd metal particles results in the observed K distribution. Adding to this, deviation from cubic symmetry will cause a; their NMR parameters are presented in Table 4.7. The results show no discernible difference in the structure of the micron-sized Pd sponge and the nano-sized Pd black. However, supported nanoparticles present very different NMR spectra. Pd PVP16 and the Pd/C samples have similar particle diameters (16 ± 3 and 13 ± 9 nm respectively); both present with broad resonances and give a K that is shifted to higher frequencies. This is due to a distribution of reduced Knight shift values presumably caused by a deviation from the cubic Pd metal structure.

Comparable results were observed by Rees *et al.* in their investigation of Pt nanoparticles using [195]Pt NMR.[69] Their results showed that 5 nm diameter Pt particles produced a broad line shape consisting of resonances with a range of K values. Each resonance represented a sub-surface layer of the Pt particle, with the core layer resonance presenting with the bulk Pt
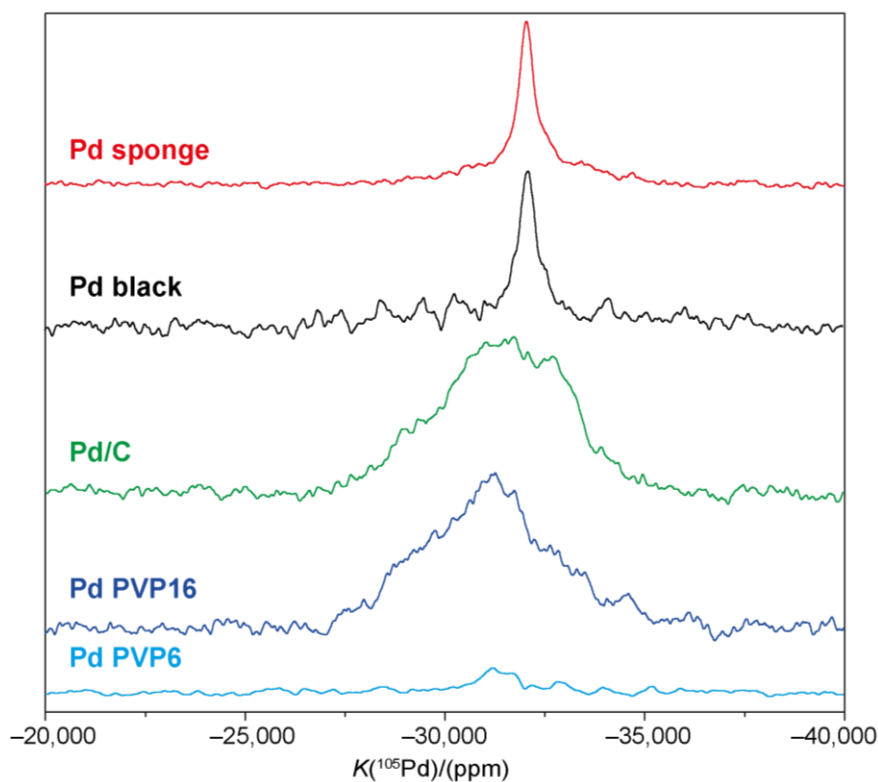
Figure 4.11 The [105]Pd static VOCS NMR of Pd sponge (red), Pd black (black), Pd/C (green), Pd PVP16 (blue) and Pd PVP6 (cyan) at 14.1 T.

Name	K /(ppm)	FWHM /(KHz)
Pd sponge	$-32{,}050 \pm 60$	13 ± 1
Pd black	$-32{,}110 \pm 90$	16 ± 1
Pd/C	$-31{,}500 \pm 400$	80 ± 10
Pd PVP16	$-31{,}100 \pm 400$	80 ± 10
Pd PVP6	-	-

Table 4.7 The experimentally determined [105]Pd NMR parameters, Knight shift K and full-width at half-maximum FWHM, of the various Pd metal particles.

metal K and the other layers having a reduced K moving towards the surface. In particles that are sufficiently small, the ratio of atoms in these subsurface layers to in the bulk is large enough that they can be observed by NMR.

Similarly, it is believed that the reduced particle size in the Pd metal particles results in the observed K distribution. Adding to this, deviation from cubic symmetry will cause a quadrupolar broadening, unlike in [195]Pt ($I = 1/2$). It could also be argued that the support

systems introduced the disorder to the metallic structure instead. However, the similarity in the spectra between the two different support types examined puts doubt on this hypothesis, as does the different NMR result from Pd PVP6 (6 ± 5 nm). No observable NMR resonance could be detected on these smaller particles. This can be explained by the smaller particles having a greater ratio of Pd atoms in a disordered environment allowing for such a large K distribution, alongside the associated quadrupolar broadening, that the resonance was too broad to be observed in the given timeframe.

4.6. Palladium Hydride

Palladium hydride is a system of great scientific interest. It was first examined as early as 1866[70] and has continued to be studied extensively, with a wide range of experimental and theoretical techniques, up to the present day.[71-73] The most exceptional of Pd metal's interactions with hydrogen is its affinity for hydrogen absorption. At room temperature and atmospheric pressure, Pd will readily absorb a volume of $H_{2(g)}$ ~900 times its own volume. By heating the material, the hydrogen is easily expelled from the Pd lattice. Additionally, the palladium structure suffers virtually no macro-disruption under bulk hydrogenation, in comparison to the other transition metals which can also absorb large amounts of hydrogen.[71] Accordingly, the use of palladium as a hydrogen storage material has driven much of the interest in the material. However, the study of the mechanics behind the hydrogen absorption
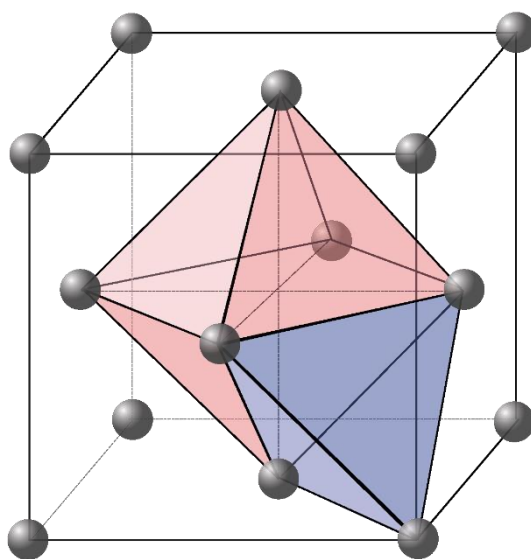
Figure 4.12 A diagram of the *fcc* Pd metal lattice highlighting the octahedral (red) and tetrahedral (blue) interstitial sites.

are also useful for better understanding the role of Pd in catalysing hydrogenation reactions. Therefore, palladium hydride is an attractive material to be investigated with the newly developed [105]Pd solid state NMR methodology.

Hydrogen inserts into the octahedral interstitial sites of the *fcc* Pd lattice, as shown by Figure 4.12, causing an isotropic lattice expansion. Pd-H[int] is described as having two phases, α and β, which differ only in their hydrogen content and increased lattice parameters. The dilute α-(PdH$_x$) exists when $x < 0.015$ (at room temperature) and its lattice parameter increases to 0.3894 nm, when compared to 0.3890 nm for pure Pd. Above that hydrogen concentration (and below a critical temperature) the α and β phases coexist, until the pure β-(PdH$_x$) phase begins at $x > 0.607$ (at room temperature) with a significantly larger lattice parameter of 0.4025 nm.[73] The Pd-H[int] P-C-T (pressure-composition-temperature) isotherms have been thoroughly studied and the saturation H/Pd ratio achieved under ambient conditions is ~0.7.[74]

Hydrogenation and dehydrogenation is known to cause permanent changes in the mechanical and electrical properties of Pd.[75] These changes are also evident in the hysteresis of pressure isotherms, and various other physical measurements, of hydrogenation and dehydrogenation cycles.[76] These physical variations are manifestations of dislocations and vacancies in the Pd structure caused by the α/β miscibility gap.[75-78] The difference in volume between the two phases causes dislocations to arise during the $\alpha\rightarrow\beta$ and $\beta\rightarrow\alpha$ phase transitions. Positron lifetime spectroscopy determined the concentration of vacancies formed under a hydrogenation and dehydrogenation cycle to pure β phase (at room temperature) to be of the order of $10^{-3} - 10^{-2}$, significantly higher than Pd at thermal equilibrium.[78]

4.6.1. Synthesis

Pd-H[int] samples for solid state NMR were produced by exposing Pd sponge (Chapter 4.5.1) to a H$_2$ atmosphere (ambient conditions) for at least 30 minutes and then packing the modified metal into NMR rotors while under the same conditions. For the ^{1}H NMR measurements, 4 mm MAS rotor inserts, provided by cortecnet, were used to keep the samples in air tight conditions. Similarly, the [105]Pd NMR was performed on samples contained in custom made 9.5 mm glass inserts sealed with Precision Seal® rubber septa caps. Dehydrogenated samples were synthesized by leaving a Pd-H[int] sample exposed to the atmosphere, allowing the H to escape the Pd lattice as H$_{2(g)}$ over several days.

4.6.2. ^{1}H Solid State NMR

The prepared Pd-H^{int} samples were examined with ^{1}H solid state NMR. Figure 4.13(a) shows the spectrum for the synthesized palladium hydride sample in an H$_2$ atmosphere, which contains three distinct resonances. A large narrow resonance at $\delta_{iso} = 4.3 \pm 0.1$ ppm is assigned as free H$_{2(g)}$,[79] a broader resonance at $\delta_{iso} = 32.9 \pm 0.2$ ppm is assigned as hydrogen within the Pd lattice, and a small resonance at $\delta_{iso} = 0.9 \pm 0.1$ ppm is believed to be an organic impurity. The H$_{2(g)}$ resonance confirms that the rotor has retained its hydrogen atmosphere and, therefore, the palladium hydride will be at saturation as β-PdH$_{0.7}$.

The large positive chemical shift, relative to the normal ^{1}H chemical shift range, is from a Knight shift effect due to the metallic environment of the Pd lattice, which confirms the presence of palladium hydride. The positive K of β-PdH$_{0.7}$ corroborates the previous results collated by Brill and Voitlander on β-PdH$_x$.[39] However, results presented here give a higher chemical shift than the β-PdH$_x$ chemical shift range determined by their study (19 - 26 ppm at 298 K).

Figure 4.13(b) shows a spectrum of the same sample once the H$_2$ atmosphere has been removed, allowing the hydrogen to escape the Pd lattice. The resonances assigned to β-PdH$_{0.7}$ and H$_{2(g)}$ are both removed whereas the small contaminant resonance has remained,
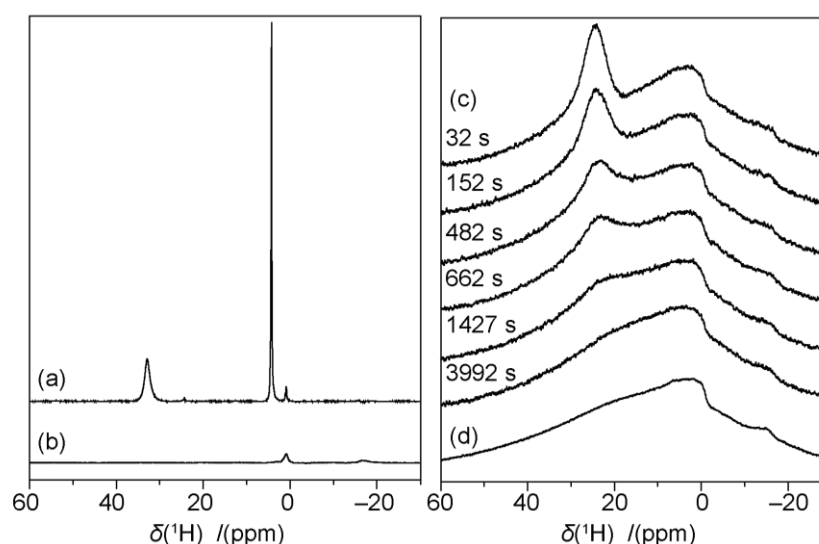
Figure 4.13 The ^{1}H NMR of palladium hydride samples acquired at 14.1 T including: MAS (12 KHz) NMR spectra of (a) PdH$_{0.7(s)}$ in a H$_{2(g)}$ atmosphere and (b) the same sample once the hydrogen has been released; and (c) static *in-situ* measurements of palladium hydride at 32 s, 152 s, 482 s, 662 s, 1427 s and 3992 s after the H$_{2(g)}$ atmosphere was first released; and (d) a static measurement of the rotor background present in this setup.

which corroborates the NMR assignments. To investigate the Pd-H$^{\text{int}}$ phases with lower hydrogen content, the H was allowed to escape from the Pd lattice *in-situ* while being observed with ^{1}H NMR. Figure 4.13(c,d) shows the β-PdH$_x$ resonance gradually diminishing in intensity over a period of ~1 hr, as expected. Additionally, as the H/Pd ratio decreases the β-PdH$_x$ shift moves towards lower values of 24 - 21 ppm, suggesting that Brill and Voitlander were working with a lower H concentration.

The dependence of K on the H/Pd ratio is due to the changes in the electron configuration. As H is first absorbed in the α phase, its electrons fill the holes in the Pd 4d orbital, which decreases the density of d states at the Fermi level, therefore reducing the susceptibility and decreasing the resultant negative K_{cp} component.[39, 67, 80] This has been observed by Brill and Voitlander[39] and corroborated by studies on the varying susceptibility of palladium hydride systems.[67, 80-81] The pure β phase begins once the susceptibility has reached zero. Now, as hydrogen content increases, the electron density of the 5s orbital increases. As seen in Equation 1.37, this results in an increase of the positive K_{p} component.[39, 81] This causes the Knight shift to increase with hydrogen content over the whole H concentration range, and explains why the ^{1}H Knight shift range observed in this study is positive.

4.6.3. ^{105}Pd Solid State NMR

Once the β-PdH$_{0.7}$ synthesis had been confirmed via ^{1}H NMR, the system was studied using ^{105}Pd static VOCS NMR. The spectrum of PdH$_{0.7}$ is shown in Figure 4.14(b) and clearly
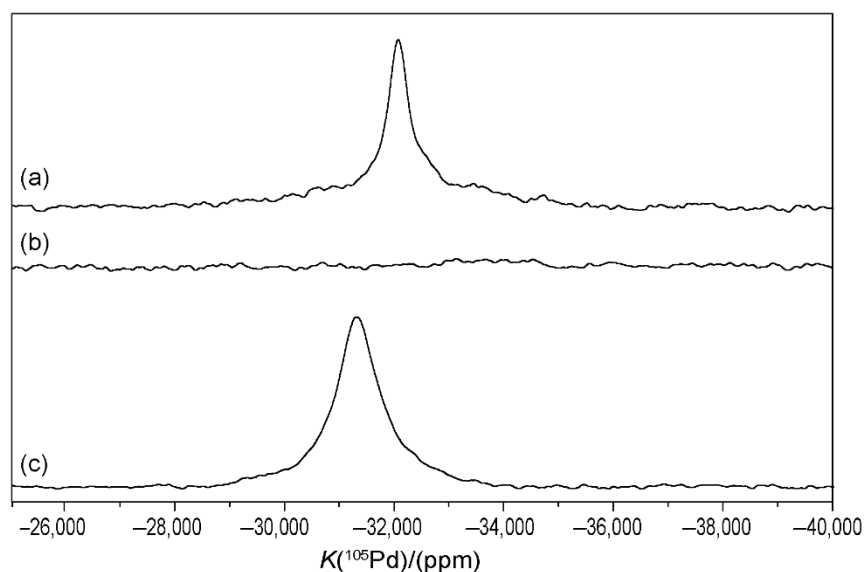
Figure 4.14 The ^{105}Pd static VOCS NMR of (a) Pd metal sponge, (b) PdH$_{0.7(s)}$ in a H$_{2(g)}$ atmosphere and (c) the same sample once the hydrogen has been released at 14.1 T.

does not return an observable [105]Pd NMR resonance. This is despite sweeping a Knight shift range down to 0 ppm, far beyond that shown in Figure 4.14. However, due to the large predicted change in K and the long [105]Pd NMR experimental times, it is possible that the resonance was missed in the search. However, it is more likely that the significant lattice expansion of $PdH_{0.7}$ may have introduced enough disorder in the structure, that the combined Knight shift and quadrupolar interactions have broadened the resonance beyond detection of the current methodology, similarly to the Pd PVP6 results.

A more successful result was obtained on the Pd sponge sample post hydrogen release, as shown in Figure 4.14(c). However, the NMR result does not return to that given by the unmodified Pd sponge (Figure 4.14(a)). The [105]Pd resonance has shifted to a less negative K of $-31,300 \pm 100$ ppm and has broadened (FWHM = 24 ± 1 KHz). This result is due to the dislocations introduced into the Pd metal structure during the hydrogenation/dehydrogenation cycle.[75-78] The deviation from cubic symmetry presents in the NMR as a reduced Knight shift and a broader resonance, as seen in the Pd nanoparticles (Chapter 4.5.2). The dislocations have previously been directly detected only by positron lifetime spectroscopy,[78] once again demonstrating the sensitivity of [105]Pd NMR to structural distortions.

4.7. Boron and Lithium Interstitial Doping of Pd Nanoparticles

As demonstrated by the palladium hydride system, light elements can be inserted into the octahedral interstitial sites in the Pd lattice, significantly altering the geometry and electronic properties of the system. Therefore, interstitial modification of Pd can be used to alter its catalytic properties. The most simple alteration, occurs when the filling of the interstitial sites with a different atom blocks the formation of Pd-H[int], which can improve catalytic selectivity in hydrogenation.[82] An advantage over other catalyst modifications, is that interstitial doping does not block active sites on the Pd surface.[83]

Palladium with interstitial carbon has been studied previously and has been found to have a maximum C/Pd ratio of 0.15.[84] Like Pd-H[int], Pd-C[int] undergoes a lattice expansion increasing the lattice parameter up to 0.399 nm.[85] The electronic properties are altered via a band overlap between the C $2p$ and the Pd $4d$ electrons.[86] Pd-C[int] has been shown to be a selective catalyst in a number of reactions.[87-88]

Additionally, Pd-B^{int} has been previously studied and was found to have a maximum B/Pd ratio of 0.20, alongside a lattice parameter increase to 0.402 nm.[89] A higher B/Pd ratio has recently been reported, although the heavier B doping resulted in structural rearrangement of the Pd lattice into a hexagonal crystal structure.[90] Electronically, Pd-B^{int} is similar to Pd-C^{int}, as the B $2p$ band is almost degenerate with the Pd $4d$ band. Pd-B^{int} has been found to be an effective catalyst in selective hydrogenations and formic acid decomposition.[91-92]

Recently, I.T. Ellis (University of Oxford) has further investigated the synthesis, physical structure, electronic properties and catalytic abilities of Pd-B^{int}. The novel Pd-Li^{int} is also synthesized for the first time and investigated in parallel to Pd-B^{int}.[66, 93] In addition to his analyses, this work used the newly developed ^{105}Pd solid state NMR alongside ^{11}B solid state NMR, ^{7}Li solid state NMR and magnetic susceptibility measurements to assist in the determination of the structure of the interstitially modified Pd nanoparticles.

4.7.1. Synthesis

The Pd-B^{int} and Pd-Li^{int} catalysts were previously synthesized as nanoparticles supported on carbon with a catalyst loading of 5 wt%. This work focuses on systems with a loading of 45 ± 2 wt%. This higher loading is not representative of how the materials would be used in catalysis, but is useful for structural determination by techniques that benefit from a higher Pd content such as ^{105}Pd NMR. By investigating the higher loaded materials, it is hoped that structural information can be inferred about the viable catalysts. The various methods for the synthesis of Pd-B^{int} and Pd-Li^{int} with different loadings, discussed in detail by Ellis, are summarised here.[66]

The synthesis of the interstitially modified nanoparticles begins with the production of palladium metal nanoparticles on a carbon support. I.T. Ellis produced a 5 wt% loaded Pd/C, by first dispersing activated carbon in butan-1-ol. A solution of Pd(NO$_3$)$_2$ was then added dropwise and stirred before being filtered, washed and dried. The catalyst was then reduced in a furnace at 770 K with a 1:1 H$_2$:N$_2$ atmosphere. For this work, a 45 wt% loaded Pd/C was achieved by grinding activated carbon with Pd(OAc)$_2$ (palladium acetate; Pd(O$_2$C$_2$H$_3$)$_2$) until homogeneous before heating in an N$_2$ atmosphere above the Pd(OAc)$_2$ decomposition temperature (478 K). These "base catalysts" were then used to synthesize the interstitially modified catalysts. The 45 wt% loaded Pd/C has previously been discussed in Chapter 4.5.

The synthesis of Pd-B^{int} began by suspending the base Pd/C catalyst in THF (tetrahydrofuran; $(CH_2)_4O$) under a N_2 atmosphere, followed by the addition of BH_3-THF. The solvent was evaporated leaving a black powder that was heated at 470 K, still under N_2, to drive the boron into the Pd lattice before being washed and dried. The synthesis of Pd-Li^{int} involved grinding LiOAc and the base Pd/C into a homogenous powder which is then heated at 520 K (to decompose the acetate) under an N_2 atmosphere before being washed and dried.

Samples of the Pd-B^{int} and Pd-Li^{int} catalysts were also prepared with an additional acid wash to remove surface contaminants. These were stirred in 0.1 M $HCl_{(aq)}$ for 30 mins before being washed with distilled water and dried.

4.7.2. Verification of the Synthesis Methods

To ensure that the 45 wt% and the 5 wt% loaded samples are sufficiently structurally similar to justify the investigation of the higher loaded materials, they were both compared via powder XRD and solid state NMR. Additionally, these catalysts are compared to their acid washed counterparts.

The success of the interstitial modification of the Pd nanoparticles can be confirmed by using powder XRD to observe the resultant lattice expansion. The XRD patterns for this suite of catalysts is shown in Figure 4.15. As expected the 5 wt% loaded Pd/C (Figure 4.15 (a)) presents reflections that match the *fcc* structure of Pd metal. The interstitial modification of the structure is evident in the patterns for 5 wt% loaded Pd-B^{int}/C and Pd-Li^{int}/C (Figure 4.15(b,d)); the reflections are shifted towards lower 2θ values, indicative of the expected lattice expansion.[66]

The 45 wt% loaded Pd/C (Figure 4.15 (f)) is shown to contain two phases: Pd and the expanded lattice Pd-C^{int}. The different synthesis method for producing the 45 wt% loaded material appears to drive C into the Pd lattice. However, the 45 wt% loaded Pd-B^{int}/C and Pd-Li^{int}/C (Figure 4.15(g,i)) have very similar XRD patterns as the 5 wt% loaded catalysts. Hence, the presence of Pd-C^{int} does not substantially affect the interstitial modification. It is hypothesized that the interstitial carbon is reduced out of the lattice during the synthesis of Pd-B^{int}/C and Pd-Li^{int}/C. The 45 wt% loaded materials have slightly broadened reflections; this is believed to be due to slight variations of the success of the interstitial doping throughout the material. The acid washed materials all present XRD patterns (Figure 4.15(c, e, h, j) that are similar to their original materials. Each present with a small shift in
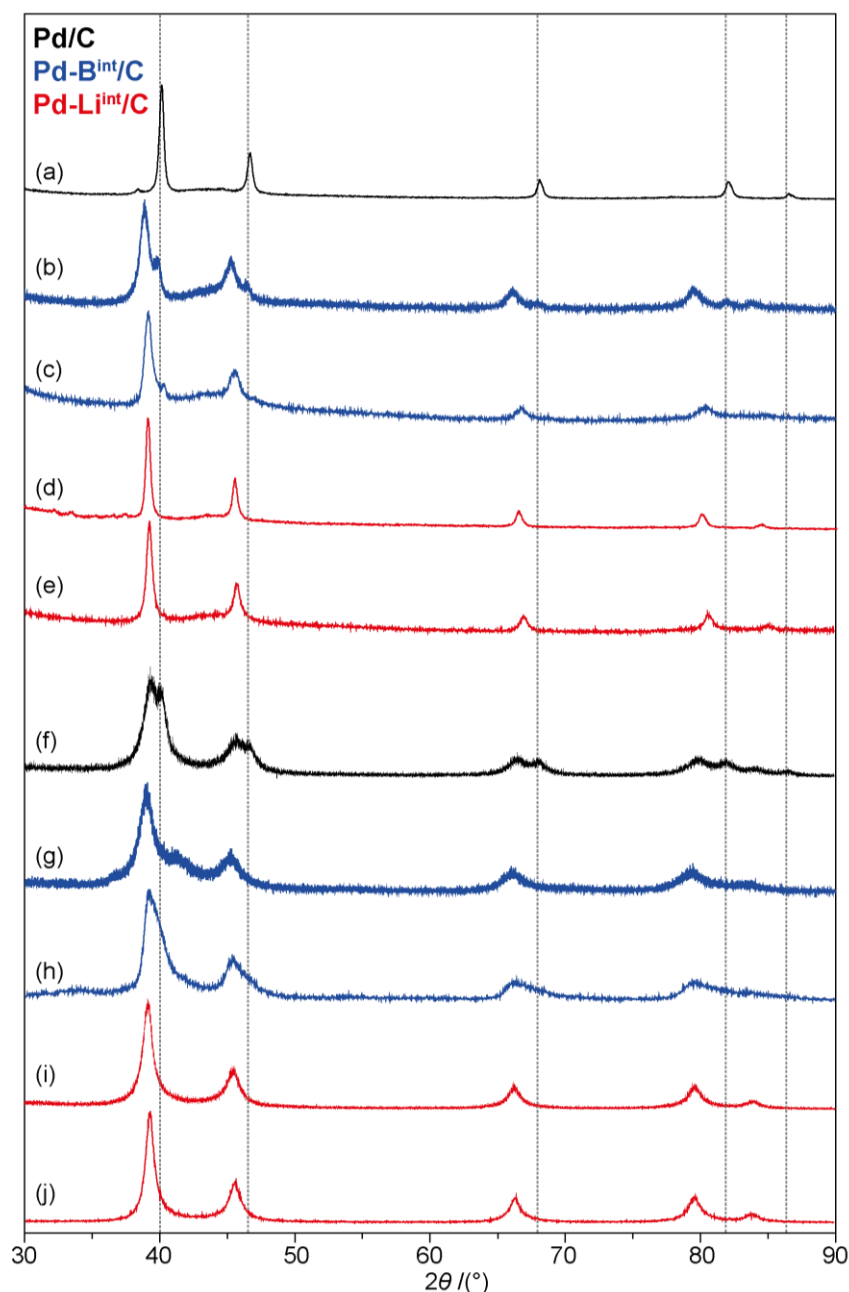
Figure 4.15 The XRD patterns for the (a - e) 5 % and (f - j) 45 wt% loaded catalysts displayed with relative intensities against 2θ. The patterns for Pd/C, Pd-B^{int}/C and Pd-Li^{int}/C are in black, blue and red respectively and (c, e, h, j) are the patterns for the acid washed catalysts. The dashed lines represent the positions of the (111), (200), (220), (311) and (222) reflections for unmodified Pd at 40.0, 46.5, 67.9, 81.9 and 86.3° respectively.

the reflections towards higher 2θ values. This suggests that the additional washing has removed some of the interstitial dopant, slightly reducing the lattice expansion.

The different loadings of the Pd-B^{int}/C and Pd-Li^{int}/C samples were also compared with ^{11}B and ^{7}Li NMR respectively, as shown in Figure 4.16. The 45 wt% and 5 wt% loaded materials are virtually indistinguishable via NMR. The powder XRD and NMR results have confirmed that the 45 wt% loaded versions of Pd-B^{int}/C and Pd-Li^{int}/C are structurally very similar to
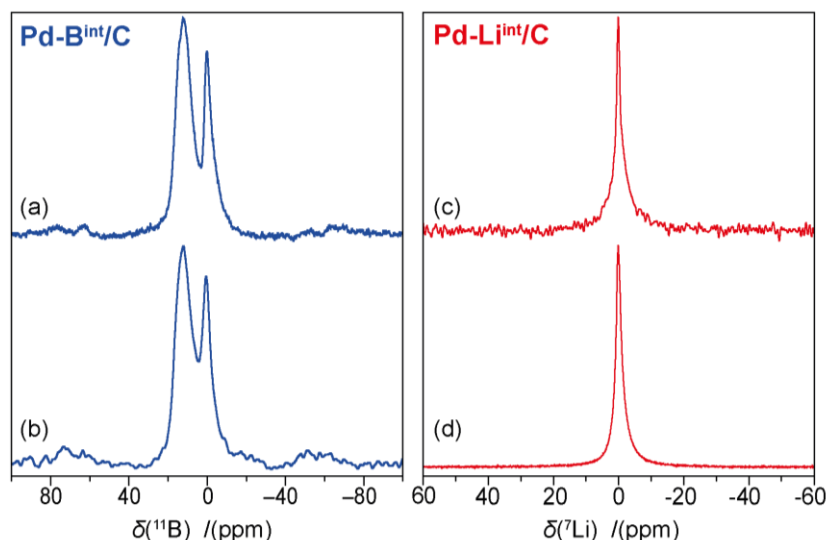
Figure 4.16 The ^{11}B MAS (12 KHz) NMR of (a) 5 % and (b) 45 wt% loaded Pd-B^{int}/C alongside the ^{7}Li MAS (30 KHz) NMR of (c) 5 % and (d) 45 wt% loaded Pd-Li^{int}/C at 14.1 T.

the 5 wt% loaded catalysts. Therefore, from this point onwards this investigation will examine only the higher loaded samples to determine the structures of these systems.

4.7.3. ^{11}B Solid State NMR of Pd-B^{int}/C

As seen in Figure 4.16(a,b) the ^{11}B NMR spectra of Pd-B^{int}/C contains at least two resonances corresponding to multiple B environments. One of these resonances corresponds to the interstitial B whereas the other(s) will be surface B contaminants. To determine which resonance corresponds to the interstitial B, T_1 relaxation measurements have been performed using the saturation recovery method described in Chapter 3.1.2. The spectrum was preliminarily deconvoluted into two resonances at 13 ± 1 ppm and 1 ± 1 ppm as shown in Figure 4.17(a); the relaxation results for both resonances are shown in Figure 4.17(c). As detailed in Chapter 3.1.2, the characteristic relaxation time T_1 can be procured by fitting the saturation recovery data. When a single-exponential was inadequate, bi-exponential and stretched-exponential fits were also attempted. The resultant T_1 values are detailed in Table 4.8.

The relaxation profile of the 1 ± 1 ppm resonance is adequately described by a single exponential with a T_1 of 0.64 ± 0.04 s. The relaxation profile of the 13 ± 1 ppm resonance is best fit with a bi-exponential function with a T_1' of 0.848 ± 0.007 s and a T_1'' of 0.003 ± 0.009 s. The necessity of two relaxation rates suggests that two separate components from different B environments, hence two different values of T_1, form the resonance at 13 ± 1 ppm. Therefore, it is believed that three B environments exist in the Pd-B^{int}/C system
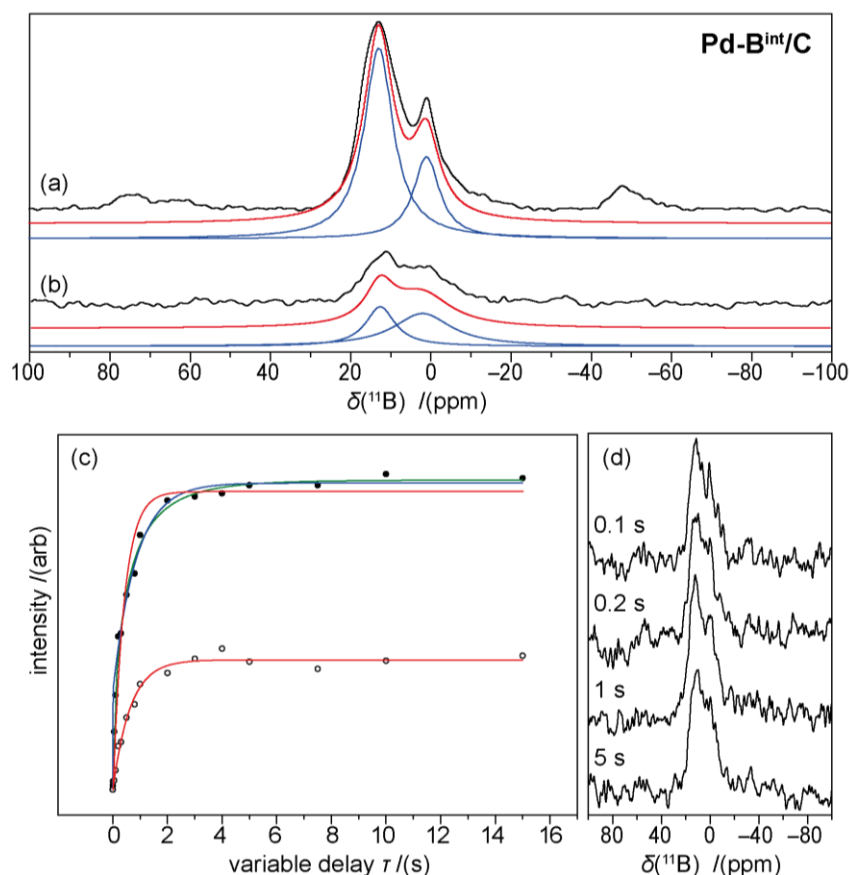
Figure 4.17 The ^{11}B MAS (12 KHz) NMR of (a) original and (b) acid washed Pd-B^{int}/C (45 wt% loaded) at 14.1 T with the spectra in black, the simulated lineshapes in red and the deconvoluted resonances in blue. (c) The saturation recovery relaxation plots of the 13 ± 1 ppm (solid circles) and 1 ± 1 ppm (hollow circles) ^{11}B resonances from Pd-B^{int}/C with single exponential fits (red), bi-exponential fits (blue) and stretched exponential fits (green). (d) The ^{11}B MAS (12 KHz) NMR of acid washed Pd-B^{int}/C (45 wt% loaded) at 14.1 T using 16,000 transients and a relaxation delays of: 0.1 s, 0.2 s, 1 and 5 s.

that result in the observed NMR lineshape. Two of the components have similar relaxation rates ($T_1 \approx 1$ s) whereas the other component relaxes exceptionally quickly ($T_1 < 0.01$ s). It is thought that the fast relaxing component is interstitial B, as a B atom inside the Pd lattice will take on the fast relaxation rate of its metallic envrionment.[94] The slower relaxing components are assigned as B compounds on the surface of the Pd/C. However, a bi-exponential relaxation profile can also be caused by a single environment with a strong quadrupolar interaction.[20] The quadrupolar nature of ^{11}B puts doubt on the assignment of the interstitial B component.

Further confirmation is provided by the ^{11}B NMR of the acid washed Pd-B^{int}/C. The acid wash should remove surface elements leaving the interstitial B intact. In fact, the acid wash has greatly reduced the B content by removing surface B compounds and reducing the amount of interstitial B (as seen in Chapter 4.7.2). This is demonstrated by the ^{11}B NMR

Resonance	Exponential fits				
	Single	**Bi**		**Stretched**	
δ_{CG} /(ppm)	T_1 /(s)	T_1' /(s)	T_1'' /(s)	T_1^* /(s)	x
13 ± 1	0.848 ± 0.007	0.848 ± 0.007	0.003 ± 0.009	0.49 ± 0.03	0.63 ± 0.03
1 ± 1	0.64 ± 0.04	-	-	-	-

Table 4.8 The parameters of single, bi and stretched exponential fits of the saturation recovery data from the ^{11}B NMR resonances present in Pd-B[int]/C (45 wt% loaded). Errors on the relaxation parameters were determined via the fitting program (*Origin Pro*), and therefore may not fully account for the experimental uncertainty in the intensity measurements.

spectrum of the acid washed Pd-B[int]/C (Figure 4.17(b)) which required ~60 times the number of transients as the spectrum of the original (Figure 4.17(a)). A greatly reduced resonance is still present at 13 ± 1 ppm, where the fast-relaxing component occurred in the original Pd-B[int]/C. However, due to the reduction in B content a saturation recovery experiment is unfeasible. Instead, the relaxation rate can be crudely estimated by varying the recycle delay of a one-pulse NMR experiment and observing any changes in the SNR. If the recycle delay is $< 5 \times T_1$ then saturation effects will occur, reducing the SNR of the produced spectrum. The results of such an experiment are shown in Figure 4.17(d). Increasing the recycle delay from 0.1 s shows no increase in the SNR at 13 ± 1 ppm. Therefore, the T_1 of the component must be < 0.02 s, confirming the presence of a very fast relaxing component that is not completely removed by an acid wash. Hence, the interstitial B component can be confidently assigned at 13 ± 1 ppm. The ^{11}B NMR also presents evidence of surface B compounds which may be of significant importance to the catalytic abilities of the material.

Interstitial B is expected to display a Knight shift due to its environment in the metal Pd lattice. The Knight shift of B in a variety of metallic environments has been reported previously and the determined shift of 13 ± 1 ppm is within the reported range.[95]

4.7.4. ^{7}Li Solid State NMR of Pd-Li[int]/C

The ^{7}Li NMR investigation of Pd-Li[int]/C closely follows the parallel ^{11}B NMR investigation of Pd-B[int]/C. The ^{7}Li NMR lineshape of Pd-Li[int]/C is also found to contain at least two resonances as shown in Figure 4.18(a). Unlike the ^{11}B NMR spectrum, the multiple resonances are difficult to deconvolute due to the featurelessness of the ^{7}Li NMR lineshape. However, the multiple resonances become clear when observing the changing lineshape
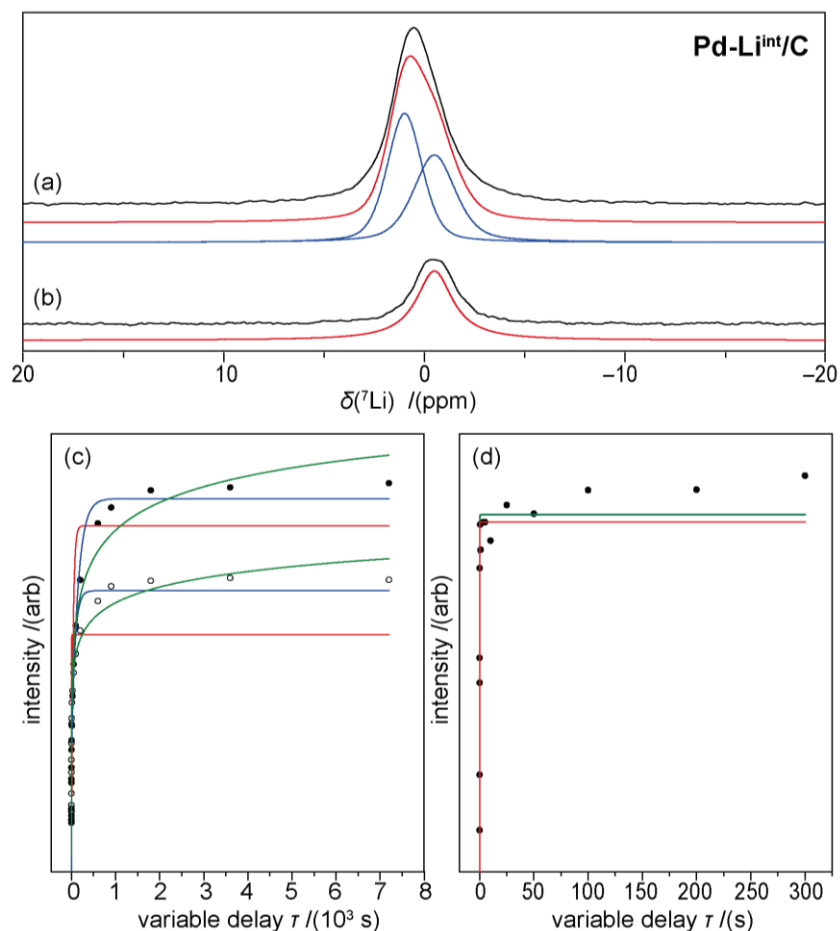
Figure 4.18 The ^{7}Li MAS (30 KHz) NMR of (a) original and (b) acid washed Pd-Li^{int}/C (45 wt% loaded) at 11.7 T with the spectra in black, the simulated lineshapes in red and the deconvoluted resonances in blue. The saturation recovery relaxation plots with single exponential fits (red), bi-exponential fits (blue) and stretched exponential fits (green) of: (c) the 0.9 ± 0.2 ppm (solid circles) and -0.6 ± 0.2 ppm (hollow circles) ^{7}Li resonances from Pd-Li^{int}/C; (d) the -0.7 ± 0.2 ppm ^{7}Li resonance from acid washed Pd-Li^{int}/C.

during saturation recovery experiments. The spectrum was preliminarily deconvoluted into two resonances at 0.9 ± 0.2 ppm and −0.6 ± 0.2 ppm. The saturation recovery results for both resonances are presented in Figure 4.18(c) and the resultant T_1 values are given by Table 4.10.

The exponential fits are poorer in the ^{7}Li saturation recovery data, compared to the ^{11}B data, due to the longer relaxation times. This enforces the use of less transients per acquisition to keep experimental time sufficiently low. However, Figure 4.18(c) demonstrates that bi-exponential fits give the best match for both components, producing four different T_1 times which, therefore, suggests four different Li environments exist in Pd-Li^{int}/C. Similarly to Pd-B^{int}/C, one of the components at −0.6 ± 0.2 ppm relaxes very fast ($T_1 < 0.01$ s), with a T_1 of

| Resonance | Exponential fits | | | | |
| | Single | Bi | | Stretched | |
δ_{CG} /(ppm)	T_1 /(s)	T_1' /(s)	T_1'' /(s)	T_1^* /(s)	x
0.9 ± 0.2	40 ± 10	140 ± 40	0.07 ± 0.05	1000 ± 1000	0.22 ± 0.03
−0.6 ± 0.2	1.7 ± 0.8	70 ± 30	0.006 ± 0.004	1000 ± 3000	0.15 ± 0.02

Table 4.10 The parameters of single, bi and stretched exponential fits of the saturation recovery data from the ^{7}Li NMR resonances present in Pd-Li^{int}/C (45 wt% loaded). Errors on the relaxation parameters were determined via the fitting program (*Origin Pro*), and therefore may not fully account for the experimental uncertainty in the intensity measurements.

0.006 ± 0.009 s, which designates it as Li located in the interstitial sites of the Pd lattice. The other components relax slower so they are assigned as surface Li environments.

Once again, the quadrupole nature of the nuclei and its effect on relaxation cannot be ignored; therefore, the acid washed Pd-Li^{int}/C sample is investigated. The ^{7}Li MAS NMR spectrum of acid washed Pd-Li^{int}/C is shown in Figure 4.18(b) and appears to contain a single component at −0.7 ± 0.2 ppm. The saturation recovery data for this resonance is shown in Figure 4.18(d) and the resultant T_1 values are detailed in Table 4.9.

The lower Li content further impedes the fitting due to the poorer SNR. However, the bi and stretched exponentials fits are not superior to the single exponential fit, and, therefore, it is believed that a singular Li environment remains. This component has a T_1 of 0.007 ± 0.001 s which, alongside its chemical shift, agrees with the designation of the interstitial Li component in Pd-Li^{int}/C. The acid wash has been successful in removing all the surface Li while leaving the interstitial Li intact.

| Resonance | Exponential fits | | | | |
| | Single | Bi | | Stretched | |
δ_{CG} /(ppm)	T_1 /(s)	T_1 /(s)	T_1' /(s)	T_1 /(s)	x
−0.7 ± 0.2	0.007 ± 0.001	0.0014 ± 0.0005	0.046 ± 0.002	0.012 ± 0.003	0.46 ± 0.06

Table 4.9 The parameters of single, bi and stretched exponential fits of the saturation recovery data from the ^{7}Li NMR resonances present in acid washed Pd-Li^{int}/C (45 wt% loaded). Errors on the relaxation parameters were determined via the fitting program (*Origin Pro*), and therefore may not fully account for the experimental uncertainty in the intensity measurements.

Mirroring the Pd-B^{int}/C results, the NMR investigation has revealed the presence of non-interstitial Li, which could significantly alter catalytic function, and has confirmed the position of the interstitial Li at -0.7 ± 0.2 ppm. The ^{7}Li Knight shift of Li metal is 0.026 %,[94] so it is reasonable to assume that Li in the metallic environment of the Pd lattice should present with a larger chemical shift than -0.7 ± 0.2 ppm. However, DFT calculations included in the work of Ellis, predict that Li is situated in the Pd interstitial sites as Li$^+$.[66, 93] This would vastly alter the Knight shift making comparison to the K of Li metal unviable.

4.7.5. Magnetic Susceptibility Measurements

The magnetic susceptibility of the Pd-H^{int} system has been thoroughly studied previously.[39, 67, 80-81] It has been clearly demonstrated that the magnetic susceptibility of the system decreases linearly with increasing H content.[80-81] As mentioned in Chapter 4.5.2, Pd metal is paramagnetic due to the Pauli susceptibility of holes in the $4d$ orbital, which is enhanced by the density of d states at the Fermi level (Stoner enhancement factor).[68] Donation of the H electrons into holes in the Pd $4d$ orbital, reduces the density of states at the Fermi level.
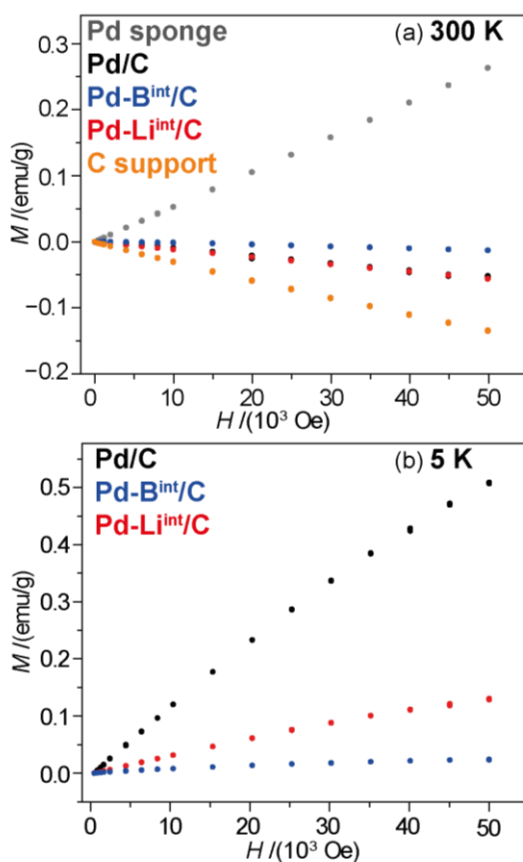
Figure 4.19 The magnetisation M versus applied field H measurements of Pd sponge (grey), Pd/C (black), Pd-B^{int}/C (blue), Pd-Li^{int}/C (red), activated C (orange) at a temperature of (a) 300 K and (b) 5 K.

Name	X_{mass} /(10^{-6} emug^{-1})
Pd/C	10.72 ± 0.07
Pd-B^{int}/C	0.55 ± 0.01
Pd-Li^{int}/C	2.79 ± 0.02

Table 4.11 The experimentally determined X_{mass} for the C supported Pd nanoparticles at a temperature of 5 K.

As the H content becomes sufficiently high (β-PdH$_{0.607}$ at room temperature), Pd-H^{int} becomes diamagnetic. Therefore, the magnetic susceptibility of the interstitially modified catalysts is of interest.

Magnetic susceptibility measurements have been made on the (45 wt% loaded) Pd/C, Pd-B^{int}/C and Pd-Li^{int}/C catalysts. By measuring the (mass) magnetisation M_{mass} versus the applied magnetic field H, the (mass) magnetic susceptibility χ_{mass} can be determined from Equation 3.13, where the gradient of the line is given by

$$\chi_{mass} = \frac{M_{mass}}{H}.$$ 4.3

As detailed in Chapter 3.2.3, a paramagnetic material has a positive χ_{mass} whereas a diamagnetic material has a negative χ_{mass}.[29] Figure 4.19(a) shows the M versus H measurements of the three carbon supported catalysts, pure Pd sponge and activated C at a temperature of 300 K. The carbon supported catalysts, including Pd/C, are diamagnetic at 300 K in contrast to the paramagnetism of pure Pd. This is due to the diamagnetism of the C support overshadowing the paramagnetism of the Pd nanoparticles. To circumvent this, the M versus H measurements on the carbon supported catalysts were also performed at a temperature of 5 K (Figure 4.19(b)). Diamagnetism is temperature independent, whereas χ is larger at lower temperatures in paramagnetic materials, including Pd metal.[29, 68, 81]

Hence, reducing the temperature will allow any paramagnetism present to dominate the diamagnetism of the C support. At 5 K, all three carbon supported catalysts demonstrate a paramagnetic χ_{mass}. As shown in Table 4.11, the interstitial modification of Pd/C with B and Li significantly reduces the χ_{mass} of the system, akin to Pd-H^{int}. This further confirms the interstitial location of B and Li in the Pd lattice.

As mentioned in Chapter 4.7, the $2p$ orbital of interstitial B is degenerate with the Pd $4d$ band. This reduces the density of states at the Fermi level and therefore reduces the Pd

paramagnetism, as observed.[90] DFT calculations in the work of I.T. Ellis suggest that no such overlap occurs between Li and Pd. Instead Li is thought to enter the lattice as Li^+, donating electrons to the Pd d band and, therefore, reducing the paramagnetism. The resultant negative charge is then spread over the Pd lattice, so that the metal remains virtually charge neutral. Interstitial Li does not reduce the density of states at the Fermi level which may explain the more paramagnetic nature of Pd-Li^{int} in comparison to Pd-B^{int} and Pd-H^{int}.[66]

4.7.6. ^{105}Pd Solid State NMR

The use of powder XRD, solid state NMR and magnetic susceptibility measurements have helped provide a thorough understanding of the Pd-B^{int}/C and Pd-Li^{int}/C systems. Finally, the novel ^{105}Pd solid state NMR was applied to these systems, the results of which are shown in Figure 4.20. Despite the 45 wt% loaded Pd/C containing a phase of Pd-C^{int}, the Pd phase still produces a ^{105}Pd resonance. The ^{105}Pd NMR parameters of Pd/C is detailed in Chapter 4.5.2

The ^{105}Pd NMR results from Pd-B^{int}/C and Pd-Li^{int}/C were fruitless. Similarly to PdH$_{0.7}$, no NMR resonance could be detected for either system despite sweeping a wide K range. Once again, the unknown K and the lattice expansion related disorder/broadening combined with long experimental times puts detection via ^{105}Pd NMR beyond the limits of this investigation. However, the negative ^{105}Pd NMR result gives even further confirmation of successful interstitial modification. If the B and Li remained only on the surface of the Pd, then the NMR spectra would resemble that of Pd/C.
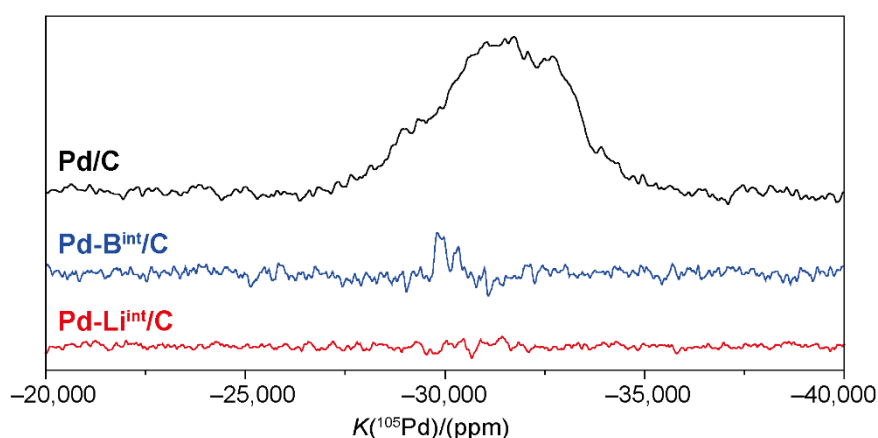
Figure 4.20 The ^{105}Pd static VOCS NMR of 45 wt% loaded Pd/C (black), Pd-B^{int}/C (blue) and Pd-Li^{int}/C (red) at 14.1 T.

4.8. Conclusions

This study proposes a standard chemical shift reference of 0.33 M $H_2PdCl_{6(aq)}$ alongside a secondary chemical shift reference of $KCl_{(s)}$. It also demonstrates the feasibility of ^{105}Pd solid state NMR on diamagnetic compounds and begins to develop a ^{105}Pd NMR chemical shift range. Combined with the more accurate determination of the room temperature Knight shift for Pd metal, these findings will greatly aid any future studies using ^{105}Pd solid state NMR.

The sensitivity of ^{105}Pd solid state NMR to structural distortions, due to its large quadrupole moment and the EFG it produces, is shown to be exemplary. Study of the hexa-halogen palladates demonstrated its sensitivity to be beyond that of NMR from other quadrupole nuclei and lab source X-ray diffractometers. X-ray PDF refinements were necessary to confirm the detected distortions in the complexes. The large Knight shift in ^{105}Pd is also shown to be a sensitive probe of disorder by its ability to detect defects in Pd metal and differentiate between different sizes of Pd metal nanoparticles.

However, its sensitivity is also very limiting. The large quadrupole moment constrains ^{105}Pd solid state NMR to studies of highly symmetrical materials. Otherwise the quadrupole broadening becomes so severe that experimental times become unfeasible. Additionally, the large Knight shift range and long experimental times make studies of Pd systems with varying Knight shifts often unachievable. This was demonstrated by the studies on the catalysis related Pd systems, which often relied heavily upon various other analytical techniques for structural determination. Nevertheless, this work forms a solid basis for any further ^{105}Pd NMR studies and verifies the technique as a sensitive probe to structural distortion, which could have significant applicability to catalytic structural determination.

The study of PdLi^{int}/C and PdB^{int}/C catalysts provided conclusive proof of the interstitial location of the dopants. The similarities of the interstitial doped materials to the palladium hydride system was also demonstrated. It is hoped that the additional structural characterisation of these catalysts will aid in future improvement of their functionality.

5

The Study of Disorder in Mullite Using Multi-Nuclear Solid State NMR and *supercell* Enabled GIPAW-DFT Calculations

5.1. Background

The ceramic aluminosilicate mullite occurs rarely in nature, forming when magma interacts with alumina rich sediments. It was first discovered on the Isle of Mull (Scotland), hence where the name originates. Mullites have excellent mechanical and thermal properties such as low thermal expansion, low thermal conductivity, high corrosion stability, and excellent creep resistance. Due to their stability in challenging conditions, mullite ceramics have a diverse range of applications including: tableware, construction ceramics, electronic devices, optically translucent ceramics for furnace windows, barrier coatings for tube furnaces, and heat shields for space re-entry vehicles. [96-97] Most relevant to this thesis is mullite's role in catalysis. Mullite is most commonly used as a substrate for catalytic converters, and is the support of choice for many supported metal catalysts.[98-102] The structure of the support is often equally as important as the structure of the metal to the overall function of a supported catalyst. Additionally, mullite structured mixed oxides have been reported as having impressive catalytic ability.[103] Therefore, a full structural characterisation of mullite is of great interest, so its catalytic function can be better understood and, hence, improved.

The majority of mullite materials are produced synthetically, with the nominal composition of:

$$Al_2(Al_{2+2x}Si_{2-2x})O_{10-x} \quad 0.2 < x < 0.9. \qquad 5.1$$
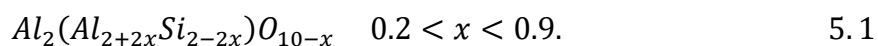
Theoretically, mullite can form any composition between sillimanite (Al_2SiO_5) and alumina (Al_2O_3), but, in reality there is a miscibility gap between $x = 0$ and $x = 0.2$ due to the differing founding conditions (moderate pressure/temperature for sillimanite and low pressure/high temperature for mullite). Mullite has two stoichiometric forms when $x = 0{:}25$ ($3Al_2O_3{:}2SiO_2$), and $x = 0{:}4$ ($2Al_2O_3{:} SiO_2$), so called 3:2 and 2:1 mullite respectively.

The structure of mullite is proposed to be closely related to that of crystalline sillimanite.[104] The suggested refined structure consists of edge sharing AlO_6 octahedral chains running along the c-axis, which are cross linked with SiO_4 and AlO_4 motifs.[105] Sillimanite consists of four oxygen environments; one is a two-coordinated oxygen (O_b) site while the rest are three-coordinated (O_t). The O_b site bridges between the two tetrahedral double chains forming a moiety that is termed T_2O.

The mullite system is characterised by a fundamental difference in an increase of Al with respect to Si, with some of the corner shared O linking the tetrahedral SiO_4 sites being removed due to charge compensation:

$$2Si^{4+} + O^{2-} \rightarrow 2Al^{3+} + \square. \qquad\qquad 5.2$$
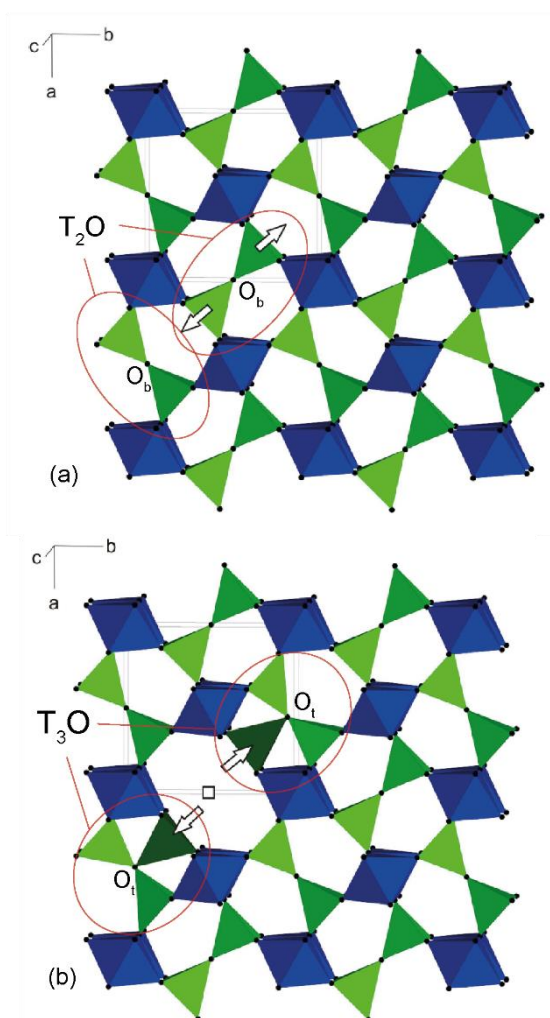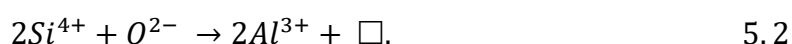
Figure 5.1 (a) A diagram of the sillimanite structure highlighting the T_2O moiety and the bridging oxygen site O_b. (b) A diagram of the proposed mullite structure highlighting the vacancy at the O_b site that causes the $T_2\square$ units to back bond towards adjacent T_2O moieties, forming T_3O environments. The Al octahedra are in blue, the Al/Si tetrahedra are in green and the oxygen atoms are in black

This produces oxygen vacancies ($\square$) in the structure, as demonstrated in Figure 5.1.[106] Crystallographic refinements suggest that the bridging oxygen (O_b) in the T_2O moiety is removed, displacing the disconnected cations. The oxygen deficient tetrahedral units ($T_2\square$) back bond to connect with an adjacent T_2O unit, forming a three-coordinated oxygen. This moiety containing three tetrahedral units connected at an O_t site, termed T_3O, is a distinctive feature in mullite's structure. The T_3O moiety directly defies the Loewenstein avoidance principle, which states that two AlO_4 units cannot share an O site.[107] The literature often uses T* or tricluster to refer to this formation; for clarity, this thesis will refer to the moiety as T_3O throughout.[96, 108]

Despite the general structure of mullite being well understood, plenty of debate still remains about the finer points, as demonstrated by the numerous studies in the literature.[105, 108-109] Ongoing debate on the mullite structure is focused on a few key areas. While some evidence of the existence of the T_3O moiety has been presented, absolute confirmation is still sought. Additionally, a structural characterisation of T_3O has proven elusive. Some report that SiO_4 is present in T_3O environments, whereas others have implied that the SiO_4 contribution is immeasurable.[97, 105, 110-112] Another unresolved aspect of the mullite structure is the configuration of the Al/Si tetrahedral units. The tetrahedral double chains in sillimanite contain alternating AlO_4 and SiO_4 units. Due to the additional Al, the same cannot be true for mullite. Whether any order exists in the AlO_4/SiO_4 distribution is still an open question.[105, 110-118]
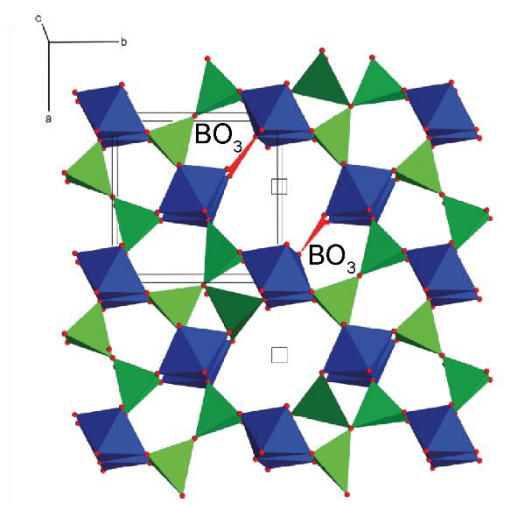
Figure 5.2 A diagram of the proposed boron doped mullite structure highlighting the BO_3 units that have substituted for the tetrahedral units of a T_2O moiety. The Al octahedra are in blue, the Al/Si tetrahedra are in green, the oxygen atoms are in black and the trigonal B units are highlighted in red.

Due to the disordered nature of the material, solid state NMR is one for the most suited analytical tools for further structural determination, because of its ability to study local order in systems lacking long range periodicity. Several ^{27}Al NMR investigations of mullite have been reported, with the majority attempting to detect the presence of the AlO_4 units in the T_3O moiety.[116, 119] King presented a deconvoluted ^{27}Al MAS NMR spectrum containing an AlO_6 site, and AlO_5 site and two AlO_4 sites, claiming that AlO_4 in the T_3O environment provides a distinct resonance.[120] Previous ^{29}Si MAS NMR studies have shown that the mullite structure possesses several Si environments.[115, 117, 119] The most intense resonance (~88 ppm) is attributed to a sillimanite type environment.[119] King, following the calculations of Ban and Okada, tentatively assigned the other resonances to Si environments with different configurations of Al/Si tetrahedral units as next nearest neighbours.[110, 120]

Another area of interest arises due to mullite's ability to accommodate a variety of different dopant cations. By doping with boron, materials can be created that share the properties of pure aluminosilicate mullites with that of aluminoborates. Aluminoborates have a wide range of uses due to several beneficial attributes, that are discussed in detail in Chapter 6.1. Therefore, these intermediate materials have great potential for material science and engineering applications, hence the numerous studies in the literature.[121-125] Several studies report that B incorporates into the mullite structure in a BO_3 coordination.[120-122, 124-125] It is believed that BO_3 substitutes for the tetrahedral units in the T_2O moiety (see Figure 5.2), via a substitution mechanism analogous to increased Al content:

$$2Si^{4+} + O^{2-} \rightarrow 2B^{3+} + \square. \qquad\qquad 5.3$$

This work uses the newly developed *supercell* program alongside DFT calculations to thoroughly model the structure of 3:2 and 2:1 mullite. These models are then compared to a rigorous study of both mullites with [29]Si, ^{27}Al and ^{17}O solid state NMR approaches. The findings of these studies are then applied to the analysis of a ^{27}Al solid state NMR study of several B doped mullites.

5.2. Experimental

5.2.1. Synthesis

The synthesis of all mullite samples used in this investigation was performed by H. Lührs (Universität Bremen) and complete details of the methodology have been reported

Name	Initial Composition /(%)		
	Al_2O_3	SiO_2	B_2O_3
3:2	60.0	40.0	0.00
1 % B_2O_3	60.76	38.23	1.01
4 % B_2O_3	61.89	33.99	4.12
6 % B_2O_3	63.86	29.76	6.38
2:1	66.5	33.5	0

Table 5.1 The ratios of Al, B and Si in the initial compositions used for the synthesis of each of the samples as percentages of alumina, silica and B_2O_3.

previously.[126] To allow a thorough ^{29}Si and ^{17}O NMR investigation, isotopically enriched samples of 3:2 and 2:1 mullite were synthesized via a solid state method. The samples were prepared using stochiometric amounts of ^{29}Si or ^{17}O enriched SiO_2 and amorphous Al_2O_3, that were homogenised and pressed into a pellet. The pellets were inductively heated, under $N_{2(g)}$, to ~1970 K to crystallize. An unenriched single crystal 2:1 mullite sample was also acquired, which was grown via the Czochralski method.[127]

The boron doped variants were produced via a sol-gel method which provides greater control over the product. Stochiometric amounts of aluminium nitrate nonahydrate $(Al(NO_3)_3 \cdot 9H_2O)$, tetraethoxysilan $(C_8H_{20}O_4Si)$ and boric acid (H_3BO_3) were dissolved in ethanol to produce a gel. The gel is then dried, ground and calcined before being heated at a temperature of 1470 K for 5 hrs.

All samples were powdered for the NMR investigation and the initial compositions of each sample are shown in Table 5.1.

5.2.2. *supercell* Structure Generation

The *supercell* program is a newly developed combinatorial structure-generation approach for the description of vacancy or substitution defects in otherwise periodically-ordered materials.[128] Disorder in a material is approximated by a set of generated structures which can then undergo GIPAW-DFT calculations.

Two approaches were used for the structure generation of the 3:2 mullite. The first approach began with the structure of sillimanite and is, therefore, referred to as the "sillimanite" approach. A 2x2x1 sillimanite structure, provided by Burnham Charles,[104] was modified by

substituting four Al into tetrahedral Si positions and two vacancies at the O_b sites. By varying the positions of the additional Al and vacancy sites, the *supercell* program was used to generate all the possible, symmetrically unique configurations of the structure. From these generated structures, 100 were randomly sampled to represent the disordered 3:2 mullite structure. This approach maintains the premise of the AlO_4/SiO_4 order present in sillimanite, whereas the next approach uses a random distribution of Al/Si tetrahedra.

The "random" approach began with a 2x2x2 initial structure based on the XRD refined 3:2 mullite structure reported by Balzar and Ledbetter.[129] The partial occupancy on the O_b site (O_b:□ = 0.871:0.129) was extrapolated by the *supercell* program, generating 9 symmetrically unique structures, that model the oxygen vacancy disorder. Then all the Al/Si tetrahedra were made interchangeable, while preserving the correct Al/Si ratio. From the symmetrically unique structures generated by the random AlO_4/SiO_4 disorder, 10 are randomly sampled from each of the 9 vacancy configurations, totalling 90 generated structures to represent the disordered 3:2 mullite structure.

The *supercell* treatment of 2:1 mullite was similar to the 3:2 "random" approach, using the same structure with an additional vacancy and a stochiometric Al/Si ratio. The increased number of vacancies generates 23 unique symmetry structures for the oxygen vacancy disorder. Once again, 10 of the generated structures representing AlO_4/SiO_4 disorder are randomly sampled for each vacancy configuration, totalling 230 structures to represent the disordered 2:1 mullite structure.

5.2.3. GIPAW-DFT Calculations

The supercell structure generation and subsequent calculations were performed by K. Okhotnikov and T. Charpentier (C.E.A. Saclay). The DFT-GGA calculations of each of the generated structures, were completed with the pseudopotential approximation in the *VASP* package.[130]

These calculations were carried out in three sequential stages. Firstly, a rough relaxation geometry optimisation was accomplished on the generated structures, using a reduced k point grid (1x1x2). The output of these calculations then underwent a precise relaxation geometry optimisation with a finer k-point grid (2x2x5), to give the final structures. Both relaxation stages employed a kinetic energy cut-off of 500 eV. In the final step, GIPAW-DFT calculations were performed on the products of the precise relaxation to provide NMR

parameters (δ_{iso}, C_Q, η_Q). The GIPAW-DFT calculations were performed with a 2x2x5 k-point grid and an energy cut-off of 550 eV while the isotropic chemical shift values were determined via a reference shielding of 308.8, 561.1 and 261.3 ppm for ^{29}Si, ^{27}Al and ^{17}O respectively.

5.2.4. Solid State NMR Measurements

The MAS NMR experiments in this study were performed at room temperature across a range of different magnetic field strengths (B_0) using Bruker Avance III-850 (19.9 T), Bruker Avance II+-600 (14.1 T), Bruker Avance II+-500 (11.7 T) and Varian Infinity+-300 (7.05 T) spectrometers. All NMR data was processed using *TOPSPIN* and MQMAS data were sheared using the *TOSPSPIN* program *xfshear*. Simulations of Gaussian/Lorentzian lineshapes were performed with *dmfit*.[49]

The ^{29}Si NMR experiments at 19.9 T and 7.05 T were undertaken using a Bruker 4 mm HX probe and a Bruker 7 mm broadband MAS probe respectively. All data was referenced with respect to kaolinite$_{(s)}$ (Al$_2$Si$_2$O$_5$(OH)$_4$; $\delta_{iso} = -93$ ppm). The ^{29}Si NMR experiments performed at 19.9 T (v_0 (^{29}Si) = 168.84 MHz) and 7.05 T (v_0 (^{29}Si) = 59.59 MHz) employed an MAS frequency of 12 KHz and 5 KHz respectively. A $^{\pi}/_2$ pulse length was determined on kaolinite$_{(s)}$ resulting in a pulse length of 4 μs for the single pulse experiments, with a recycle delay of 4,500 s.

The ^{27}Al NMR experiments were performed at 11.7 T (v_0 (^{27}Al) = 130.29 MHz) and 14.1 T (v_0 (^{27}Al) = 156.34 MHz) with an MAS frequency of 20 KHz. The experiments were completed using a Bruker 3.2 mm HX probe with all data referenced with respect to yttrium aluminium garnet$_{(s)}$ (YAG; Y$_3$Al$_5$O$_{12}$; δ_{iso}[AlO$_6$] = 0.7 ppm). A $^{\pi}/_2$ pulse length was determined on YAG$_{(s)}$ resulting in a selective $^{\pi}/_{12}$ pulse length of 2 μs being used for the single-pulse experiments, with a recycle delay of 4 s used throughout. The 2D MQMAS experiments utilised a *z*-filtered 3QMAS pulse sequence with a 3.75 μs excitation pulse, a 1.25 μs conversion pulse and a 25 μs selective *z*-filter pulse.

The ^{17}O NMR experiments were performed at 11.7 T (v_0 (^{17}O) = 67.78 MHz) with an MAS frequency of 20 KHz. The experiments were completed using a Bruker 3.2 mm HX probe with all data referenced with respect to ^{17}O enriched (10 %) H$_2$O$_{(l)}$ ($\delta_{iso} = 0$ ppm). A $^{\pi}/_2$ pulse length was determined on ^{17}O enriched H$_2$O$_{(l)}$ resulting in a selective $^{\pi}/_4$ pulse length of 2 μs. A ($^{\pi}/_4$)-τ-($^{\pi}/_2$) echo sequence was utilised to diminish ringing effects present at low

frequencies. A recycle delay of 750 s was used throughout and a rotor synchronised τ period of 47 μs was used in the echo experiments. The 2D MQMAS experiments utilised a z-filtered 3QMAS pulse sequence with a 3 μs excitation pulse, a 0.9 μs conversion pulse and a 20 μs selective z-filter pulse.

5.3. $3Al_2O_3:2SiO_2$ Mullite

5.3.1. ^{29}Si Results

The deconvoluted ^{29}Si MAS NMR spectrum of 3:2 mullite is presented in Figure 5.3(a), alongside the simulated spectra of the *supercell*-GIPAW DFT structures generated from the "sillimanite" and "random" starting approaches (Figure 5.3(c) and (d) respectively). It is clear that the "random" approach produces a spectrum in better agreement with the experimental data, as the "sillimanite" approach simulation is missing several lower frequency components. While the "random" approach does not produce a perfect simulation, it is sufficient to provide a comprehensive assignment of the deconvoluted resonances in the ^{29}Si MAS NMR spectrum (Table 5.2). The SiO_4 environments predicted by the calculations are schematically represented in Figure 5.3(e). The nomenclature used for each environment,

Experimental		Calculated		Assignment	
δ_{iso}	Intensity	δ_{iso}	Intensity	Name	Moiety
/(ppm)	/(%)	/(ppm)	/(%)		
(±0.5)	(±1)				
−79.9	1	−82.3	7	$8Al(O_t)$	
−81.9	2	−83.4	5	$7Al(O_t):1Si(O_t)$	T_3O
−83.7	4	−87.3	4	$6Al(O_t):2Si(O_t)$	
−87.5	37	−89.8	36	$1Al(O_b):6Al(O_t)$	
−90.3	25	−92.9	23	$1Si(O_b):6Al(O_t)$	
−92.5	9	−94.9	15	$1Al(O_b):4Al(O_t):2Si(O_t)$	T_2O
−95.1	9	−98.1	11	$1Si(O_b):4Al(O_t):2Si(O_t)$	
−97.8	3	−102.5	0	$4Si(O_b)$	
−106.9	10	-	-	SiO2	SiO_2

Table 5.2 The experimental and simulated ("random" approach *supercell* enabled GIPAW-DFT) NMR parameters of the deconvoluted resonances of the ^{29}Si spectrum of ^{29}Si labelled 3:2 mullite, with each resonance assigned a corresponding SiO_4 environment.
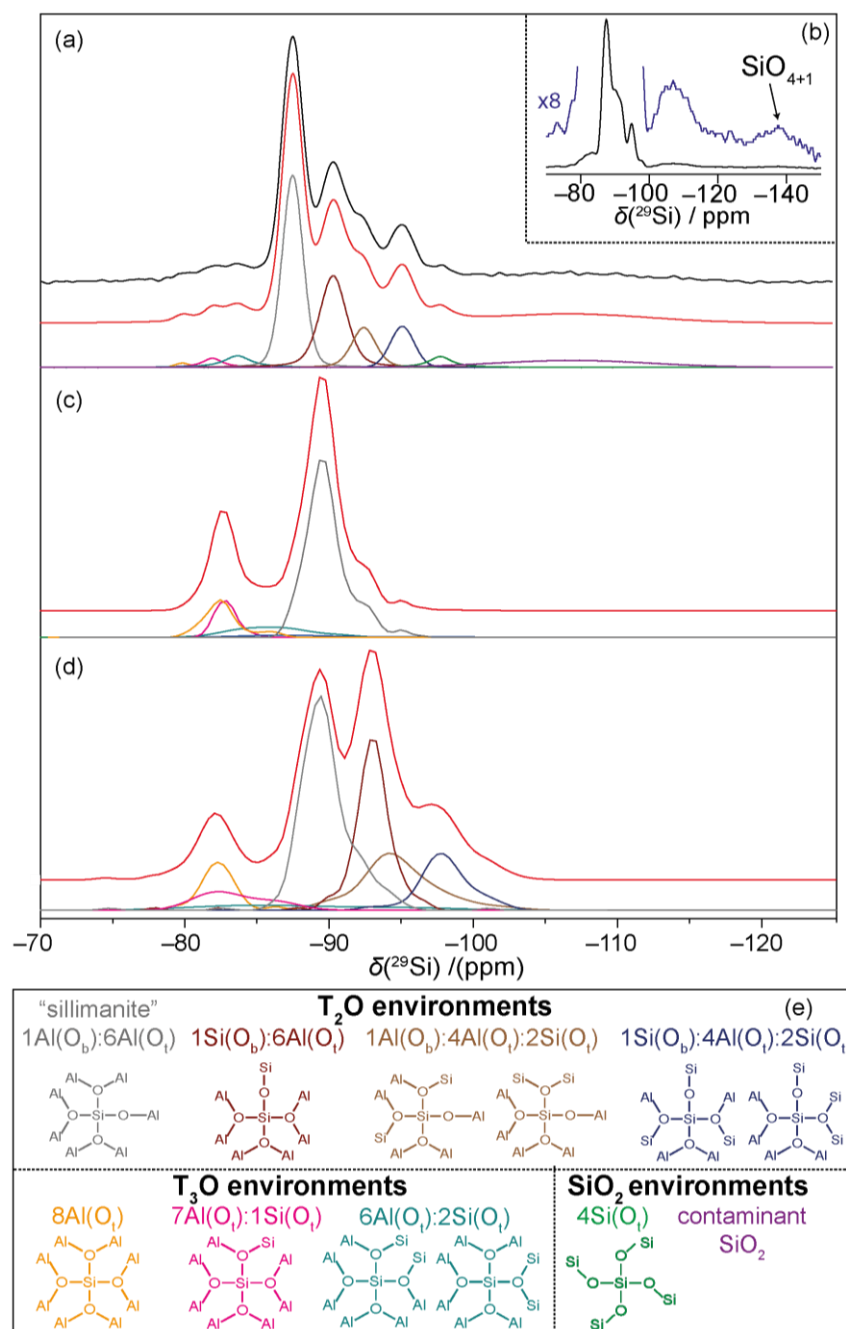
Figure 5.3(a) The ^{29}Si MAS (12 KHz) NMR spectrum of ^{29}Si enriched 3:2 mullite at 19.9 T with (b) an insert displaying the magnified, quantitative ^{29}Si MAS (5 KHz) NMR spectrum of ^{29}Si enriched 3:2 mullite at 7.05 T with the SiO$_{4+1}$ resonance labelled. The *supercell* enabled GIPAW-DFT simulated ^{29}Si spectra of the (c) "sillimanite" and (d) "random" approaches to 3:2 mullite. Experimental spectra are in black, with simulated lineshapes in red and deconvoluted/simulated resonances in colours corresponding to (e) the schematic representation of the assigned Si environments.

describes the number of next nearest Al or Si neighbours and the nature of the shared O between them (O$_b$ or O$_t$) (*e.g.* the sillimanite Si environment 1Al(O$_b$):6Al(O$_t$) is bonded to one Al through a bridging oxygen and three pairs of Al via three-coordinated oxygens).

The ^{29}Si MAS spectrum contains multiple SiO_4 resonances, with the most dominant assigned to a sillimanite environment at -87.5 ± 0.5 ppm, which splits the spectrum into two distinct regions. At lower frequencies are the four SiO_4 environments, including the sillimanite environment, which exist in T_2O moieties. At higher frequencies are three environments that represent T_3O moieties, and, thus, confirm the existence of the T_3O moiety in the mullite structure and the presence of SiO_4 in said moiety. In both the T_2O and T_3O regions of the spectrum, the various environments produce distinct resonances due to the different number of SiO_4 units each has as next nearest neighbours. Additional small resonances exist in the lowest frequency region of the NMR spectrum that are not observable in the simulations. The resonance at -97.8 ± 0.5 ppm is predicted by the calculation, albeit in negligible quantities, and can be assigned to an SiO_2 environment within the mullite structure. The resonance at -106.9 ± 0.5 ppm is assigned to an amorphous silica impurity remaining from the starting material of the solid state synthesis method. The calculations also predict a small amount of SiO_4 with an additional long bond, dubbed SiO_{4+1}. A corresponding resonance can be observed in the longer, quantitative ^{29}Si MAS measurement (Figure 5.3(b)) at ~135 ppm, between the expected shifts for SiO_4 (-60 to -120 ppm) and SiO_5 (~-150 ppm).[2] The presence of this distorted SiO_{4+1} polyhedra is discussed in greater detail in the next section (Chapter 5.3.2).

The "random" approach calculations produce a minor δ_{iso} inaccuracy and the component intensities (site populations) are slightly misrepresented, as demonstrated in Table 5.2. Despite, this the combined use of NMR and *supercell* enabled DFT calculations, provides a complete understanding of the mullite structure which allows total assignment of the ^{29}Si NMR spectrum. The ^{29}Si assignments are in partial agreement with those previously reported,[110, 120] but correct the exact assignment of some of the resonances.

The "sillimanite" approach completely under represents the T_2O environments, overpredicting T_3O formation. The failure of this approach, that assumed some of the sillimanite AlO_4/SiO_4 order remained, compared with the success of the no order "random" approach, implies a lack of order in the AlO_4/SiO_4 configuration in mullite's structure. A random configuration of Al and Si tetrahedral units proves that the mullite structure defies the Loewenstein avoidance principle. It is hypothesized that by ignoring this principle, the "random" approach may ignore an inequivalence of charge which could result in the observed δ_{iso} inaccuracy. Further investigation of this hypothesis was beyond the scope of this study.

From this point forward, only the results from the calculations performed on the structures generated by the "random" approach will be discussed.

5.3.2. ^{27}Al Results

The calculated ^{27}Al NMR parameters (δ_{iso} and C_Q) from the 3:2 mullite generated structures are presented in Figure 5.4(a). Unlike the ^{29}Si NMR study, the quadrupolar broadened ^{27}Al NMR does not have the resolution to distinguish environments by their different next nearest neighbours. Instead, the data is classified by the Al coordination number, with AlO$_4$ sites

Figure 5.4 (a) A plot of the GIPAW-DFT calculated ^{27}Al δ_{iso} and C_Q values of the various environments in the *supercell* generated 3:2 mullite structures. (b) The ^{27}Al 3QMAS (20 KHz) NMR 2D spectrum of ^{17}O enriched 3:2 mullite at 11.7 T with the MAS spectrum above and the projected δ_{iso} spectrum on the right. The predicted environments from the simulations are assigned to distinct resonances in the 2D spectrum with the addition of an α-Al$_2$O$_3$ contaminant.

divided into T_2O and T_3O moieties (labelled $AlO_4(T_2O)$ and $AlO_4(T_3O)$ respectively). The predicted environments are then assigned to the resolved resonances in the ^{27}Al 2D 3QMAS spectrum (Figure 5.4(b)). As expected, the most populated environments in both the simulated and NMR data are the moieties found in the parent sillimanite: $AlO_4(T_2O)$ and AlO_6.[104]

The $AlO_4(T_3O)$ environments are indistinguishable from $AlO_4(T_2O)$ environments via modern NMR methodology, with mean calculated δ_{iso} values of 64 ± 9 ppm and 67 ± 6 ppm respectively. This contrasts with published work that assigned the resolved resonance at $\delta_{iso} \approx 50$ ppm as $AlO_4(T_3O)$.[120] Instead, $AlO_{4+1}(T_3O)$, an environment analogous to the Si environment SiO_{4+1}, is assigned to that resonance in the GIPAW-DFT calculations. These quasi-tetrahedral environments form as part of the T_3O moiety, but have an additional long bond to an adjacent O_t site creating a four-coordinated oxygen site (O_q). Due to the elongated bond the resonance is situated at a mean calculated δ_{iso} of 45 ± 5 ppm, between the shifts of AlO_4 (80 - 50 ppm) and AlO_5 (40 - 30 ppm) giving further support to the proposal of the AlO_{4+1} moeity.[2] The simulation also predicts some AlO_5 formation that is not observable in the 2D 3QMAS NMR data. However, the low population (< 1%) and wide spread NMR parameters of the proposed AlO_5 sites would significantly hinder detection.

The oxygen deficient tetrahedral units ($AlO_3\square$), formed by vacancy substitution at T_2O moieties in the generated structures, almost completely form T_3O polyhedra post DFT geometry optimisation. However, a very small percentage (< 1%) remain as $AlO_3\square$ in the relaxed structure with a calculated δ_{iso} of 81 ± 9 ppm. This metastable environment, that is predicted in mullite for the first time, is tentatively assigned to the small, high frequency resonance in the 2D 3QMAS NMR spectrum (Figure 5.4). Despite the low site population, it has a concentrated population of predicted δ_{iso} and C_Q values, and, hence, may be detected by ^{27}Al 3QMAS NMR.

An unpredicted resonance at $\delta_{iso} \approx 16$ ppm in the ^{27}Al NMR spectra can be assigned to an α-Al_2O_3 impurity remaining from the starting material of the solid state synthesis method.[2] The good agreement between the calculated and experimental ^{27}Al NMR parameters lends further credence to the strength of the *supercell* method of disorder simulation, which has allowed a complete assignment of the ^{27}Al NMR data.

5.3.3. ^{17}O Results

The GIPAW-DFT calculated ^{17}O NMR parameters, δ_{iso} and C_Q, from the 3:2 mullite generated structures are presented in Figure 5.5(a). The generated structures contain 53 unique O sites, therefore only the 10 sites with > 1 % of the total O population are illustrated in Figure 5.5(a). Each unique environment is classified by its coordination with O_b, O_t and
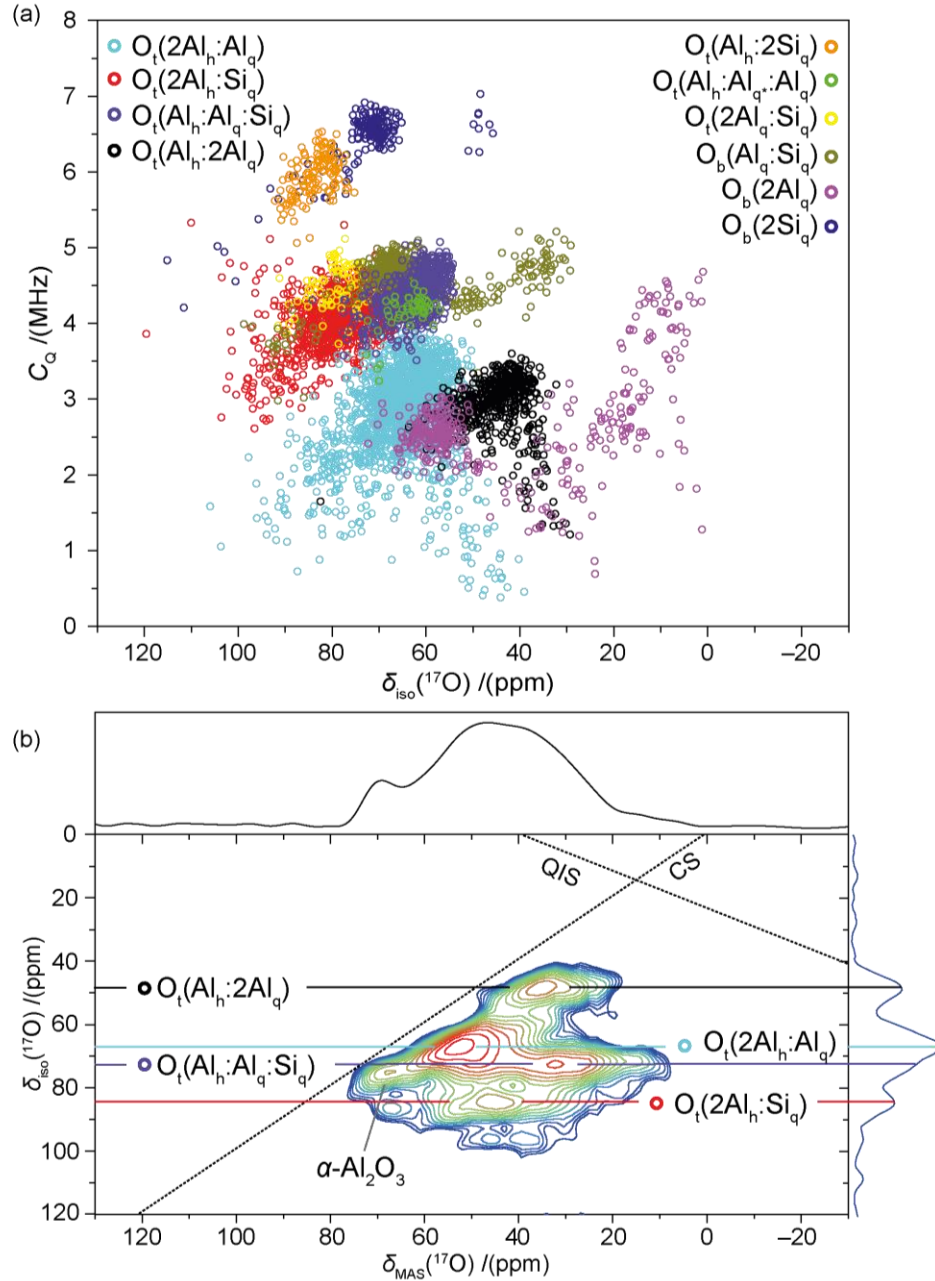
Figure 5.5(a) A plot of the GIPAW-DFT calculated ^{17}O δ_{iso} and C_Q values of the environments (with > 1% total O population) in the *supercell* generated 3:2 mullite structures. (b) The ^{17}O 3QMAS (20 KHz) NMR 2D spectrum of ^{17}O enriched 3:2 mullite at 11.7 T with the MAS spectrum above and the projected δ_{iso} spectrum on the right. The predicted environments from the simulations are assigned to distinct resonances in the 2D spectrum with the addition of an α-Al$_2$O$_3$ contaminant.

O_q representing two, three and four coordinate oxygen sites respectively. The sites are further labelled by the coordination of their nearest neighbours, detailed by the subscript (h = six-coordinate; q = four-coordinate; q* = 4+1-coordinate). For example, $O_t(2Al_h:Al_q)$ is a three-coordinate oxygen shared by two AlO_6 and one AlO_4 polyhedra.

As mentioned in Chapter 5.1, the sillimanite structure contains four oxygen sites: $O_t(2Al_h:Al_q)$, $O_t(2Al_h:Si_q)$, $O_t(Al_h:Al_q:Si_q)$ and $O_b(Al_q:Si_q)$. Compared to sillimanite, the disorder in the 3:2 mullite structure has introduced many additional environments, as demonstrated by Figure 5.5(a). However, only the four most populated O environments can be assigned in the ^{17}O 3QMAS 2D spectrum of 3:2 mullite (Figure 5.5(b)). These environments are: $O_t(2Al_h:Al_q)$ with a predicted δ_{iso} of 65 ± 8 ppm; $O_t(2Al_h:Si_q)$ with a predicted δ_{iso} of 79 ± 7 ppm; $O_t(Al_h:Al_q:Si_q)$ with a predicted δ_{iso} of 62 ± 5 ppm; and $O_t(Al_h:2Al_q)$ with a predicted δ_{iso} of 45 ± 6 ppm. Similarly to the ^{27}Al NMR, the ^{17}O spectra also contains a resonance from the α-Al_2O_3 impurity which has a $\delta_{iso} \approx 75$ ppm.[2, 131]

The only sillimanite site not observable in the experimental data is the bridging oxygen $O_b(Al_q:Si_q)$, predicted at $\delta_{iso} = 62 \pm 13$ ppm. It is overshadowed in the NMR data by the more popular sites that surround it. This fate is shared by several other environments presented in Figure 5.5(a), including the T_3O site $O_t(2Al_q:Si_q)$. Two other environments, $O_t(Al_h:2Si_q)$ and $O_b(2Si_q)$, are shown to have distinct NMR parameters from the popular sites. However, these are not observed in the 2D NMR spectrum due to their stronger quadrupole interaction ($C_Q \approx 6$ MHz) and low population ($< 4\%$).[132] Unfortunately, the four-coordinated sites O_q, whose detection via ^{17}O NMR would confirm the presence of the $(Al/Si)O_{4+1}$ moieties, are predicted to have a combined population of ~1 % and, therefore, are not observed.

Similarly to the ^{29}Si data, the predicted δ_{iso} values are all underestimated by a few ppm. Still, the close agreement between the predicted and experimental ^{17}O NMR parameters lends credence to the proposed 3:2 mullite structure, despite not directly confirming the presence of moieties of greatest interest (T_3O, $(Al/Si)O_{4+1}$, etc.). Once again, the *supercell* enabled GIPAW-DFT calculations have allowed complete assignment of the ^{17}O NMR spectra.

5.4. 2Al$_2$O$_3$:SiO$_2$ Mullite

5.4.1. ^{29}Si Results

The ^{29}Si MAS NMR of 2:1 mullite is presented in Figure 5.6(a), alongside the simulated spectrum of the structures generated by the *supercell* GIPAW-DFT approach (Figure 5.6(b)). The simulated spectrum for 2:1 mullite has several differences to the calculated ^{29}Si

spectrum for 3:2 mullite (Figure 5.3(c)). As shown by Table 5.3, there are less Si habituated in the T$_2$O environments, whereas the higher frequency T$_3$O moieties have an increased presence. An additional T$_3$O site, 3Al(O$_q$):6Al(O$_t$) (Figure 5.6(c)), is sufficiently populated

to affect the simulation. This Si site is bonded to an O$_q$ site in a T$_3$O moiety that contains the quasi-tetrahedral AlO$_{4+1}$ unit. The higher population of the T$_3$O environments is in line with the increased vacancies in the 2:1 mullite structure. Unfortunately, the ^{29}Si NMR of 2:1 mullite does not reflect these differences. As shown in Figure 5.6(a), the spectrum is overshadowed by an amorphous SiO$_2$ impurity produced by the single crystal synthesis method. This impurity makes structural determination of 2:1 mullite by ^{29}Si NMR on this sample fruitless, while the solid state ^{17}O enriched 2:1 mullite sample was produced in too small of a quantity to study with ^{29}Si NMR.
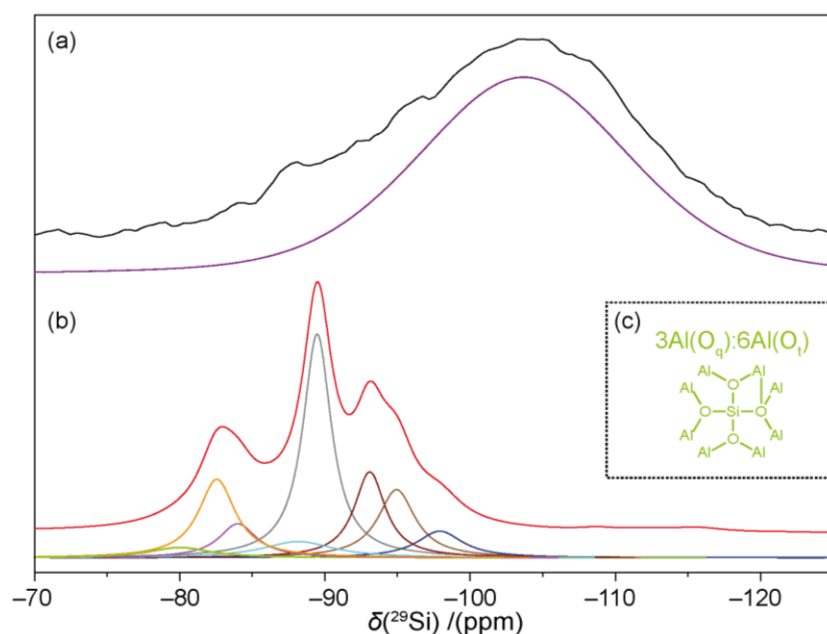
Figure 5.6(a) The ^{29}Si MAS (5 KHz) NMR spectrum of 2:1 mullite (single crystal) at 7.05 T. (b) The *supercell* enabled GIPAW-DFT simulated ^{29}Si spectra of 2:1 mullite. Experimental spectra are in black, with simulated lineshapes in red and deconvoluted/simulated resonances in colours corresponding to Figure 5.3(e) and the insert (c), which together show schematic representations of the most popular (> 2 %) predicted Si environments in 2:1 mullite.

Calculated		Assignment	
δ_{iso}	Intensity	Name	Moiety
/(ppm)	/(%)		
−79.9	2.0	$3Al(O_q):6Al(O_t)$	
−83.1	14.3	$8Al(O_t)$	
−84.3	8.1	$7Al(O_t):1Si(O_t)$	T_3O
−88.5	5.2	$6Al(O_t):2Si(O_t)$	
−89.5	34.9	$1Al(O_b):6Al(O_t)$	
−92.6	16.0	$1Si(O_b):6Al(O_t)$	
−95.2	13.7	$1Al(O_b):4Al(O_t):2Si(O_t)$	T_2O
−97.3	5.7	$1Si(O_b):4Al(O_t):2Si(O_t)$	

Table 5.3 The calculated (*supercell* enabled GIPAW-DFT) NMR parameters of the simulated resonances of the ^{29}Si spectrum of 2:1 mullite and the corresponding environments.

5.4.2. ^{27}Al and ^{17}O Results

The calculated ^{27}Al NMR parameters (δ_{iso} and C_Q) from the 2:1 mullite generated structures are presented in Figure 5.7(a). In comparison to the 3:2 mullite predictions (Table 5.4), there is an expected increase in the number of Al in $AlO_{4+1}(T_3O)$, $AlO_4(T_3O)$ and $AlO_3\square$ moieties due to the increase in vacancies. The ^{27}Al 2D 3QMAS spectrum of 2:1 mullite (single crystal) is presented in Figure 5.7(b). Unfortunately, the increase in population of the $AlO_{4+1}(T_3O)$ and $AlO_3\square$ sites is too small to give any appreciable difference in the NMR spectrum. The

Site	Calculated Al Population Share /(%)	
	3:2 mullite	2:1 mullite
AlO_6	42.8	40.0
$AlO_4(T_2O)$	48.4	46.8
$AlO_4(T_3O)$	4.4	7.2
$AlO_{4+1}(T_3O)$	2.2	2.6
$AlO_3\square$	1.8	2.3
AlO_5	0.5	1.1

Table 5.4 The calculated Al population, as a percentage of all Al sites, of the NMR observed environments in the *supercell* generated structures of 3:2 and 2:1 mullite.
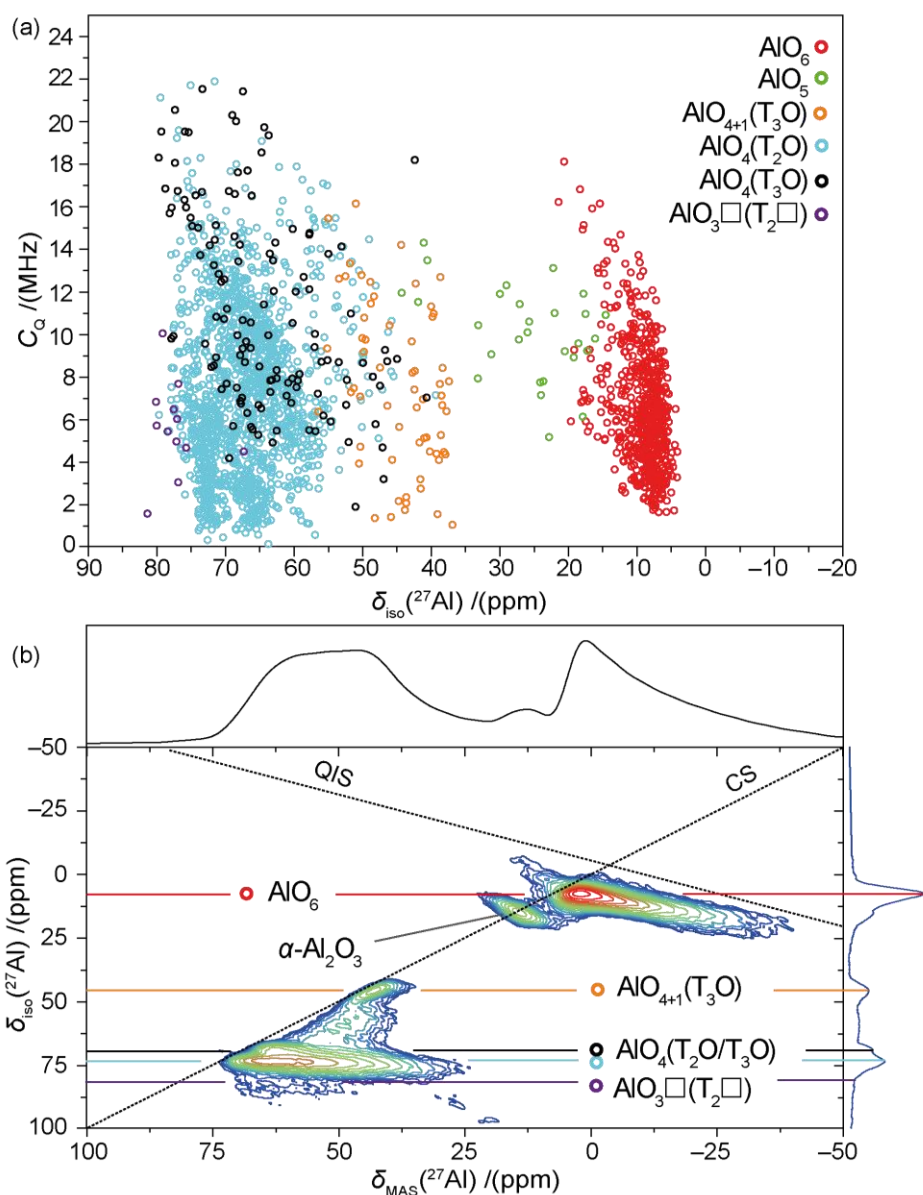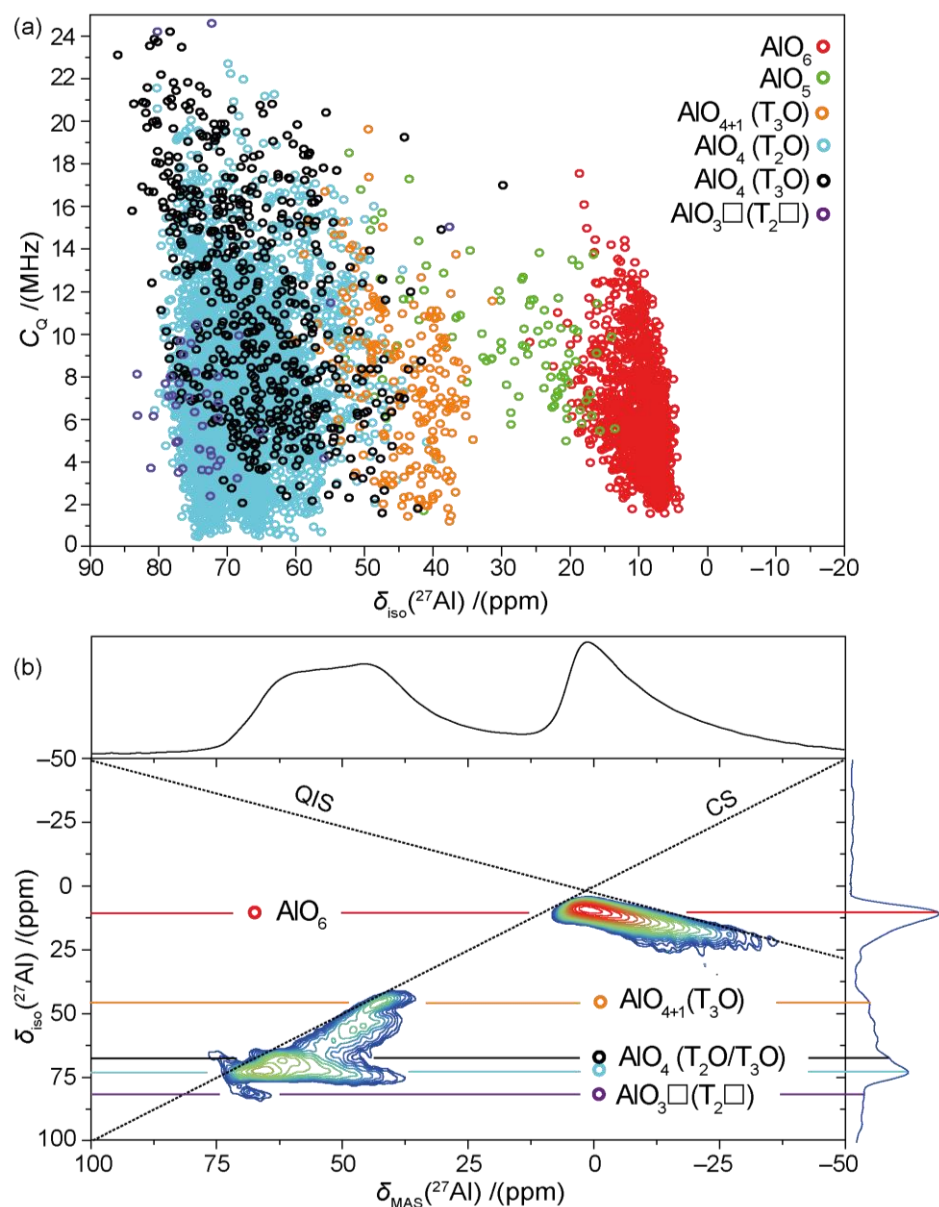
Figure 5.7 (a) A plot of the GIPAW-DFT calculated ^{27}Al δ_{iso} and C_Q values of the various environments in the *supercell* generated 2:1 mullite structures. (b) The ^{27}Al 3QMAS (20 KHz) NMR 2D spectrum of 2:1 mullite (single crystal) at 11.7 T with the MAS spectrum above and the projected δ_{iso} spectrum on the right. The predicted environments from the simulations are assigned to distinct resonances in the 2D spectrum.

2D 3QMAS NMR spectrum does, however, show an ostensible increase in intensity at $\delta_{\text{iso}} \approx 65$ ppm which is credited to the larger population of the AlO$_4$(T$_3$O) environment in 2:1 mullite.

The calculated ^{17}O NMR parameters, δ_{iso} and C_Q, from the 2:1 mullite generated structures are presented in Figure 5.8(a). In comparison to the 3:2 mullite predictions (Table 5.5), there is an expected decrease in the number of Si containing moieties due to the increased Al:Si ratio. The ^{17}O 2D 3QMAS spectrum of 2:1 mullite is presented in Figure 5.8(b). Similarly
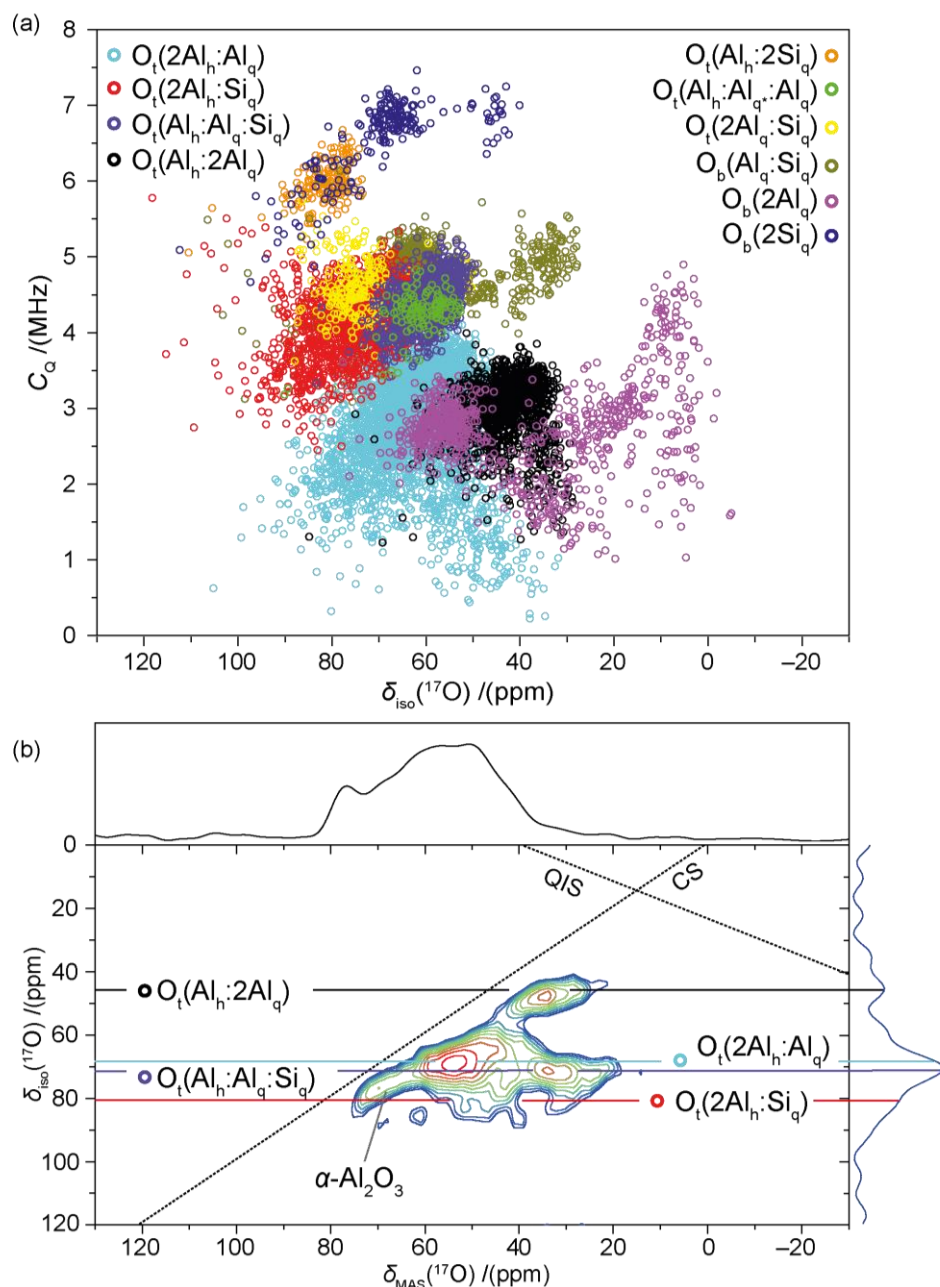
Figure 5.8(a) A plot of the GIPAW-DFT calculated ^{17}O δ_{iso} and C_Q values of the various environments in the *supercell* generated 2:1 mullite structures. (b) The ^{17}O 3QMAS (20 KHz) NMR 2D spectrum of ^{17}O enriched 2:1 mullite at 11.7 T with the MAS spectrum above and the projected δ_{iso} spectrum on the right. The predicted environments from the simulations are assigned to distinct resonances in the 2D spectrum.

to the ^{27}Al results, the change in population is too small to be observable in the NMR spectra. The ^{17}O 3QMAS for 2:1 mullite produced a lower SNR, due to a smaller quantity of the sample, which is responsible for the apparent reduction in intensity of some resonances.

The solid state synthesised 2:1 mullite is shown to have an α-Al$_2$O$_3$ impurity in the ^{17}O NMR data (Figure 5.8(b)), as seen in the ^{27}Al and ^{17}O data on the solid state synthesised 3:2 mullite (Figure 5.4(b) and Figure 5.5(b) respectively). However, due to the different synthesis, the

Site	Calculated O Population Share /(%)	
	3:2 mullite	2:1 mullite
$O_t(2Al_h:Al_q)$	22.1	23.0
$O_t(Al_h:Al_q:Si_q)$	17.8	14.7
$O_t(Al_h:2Al_q)$	13.9	16.9
$O_t(2Al_h:Si_q)$	13.8	11.1

Table 5.5 The calculated O population, as a percentage of all O sites, of the NMR observed environments in the *supercell* generated structures of 3:2 and 2:1 mullite.

single crystal 2:1 mullite does not contain such an impurity and, therefore, it is not detected in the ^{27}Al NMR data on 2:1 mullite (Figure 5.7(b)). Due to the small changes in site population it appears that only ^{29}Si, out of the NMR nuclei examined, has the resolution to confidently confirm differences in the 2:1 mullite. Unfortunately, this would require a new sample to be synthesized that does not contain such a large amorphous SiO_2 contaminant, perhaps by the sol-gel method.

5.5. Boron Doped Mullite

The study of 1 %, 4% and 6% B_2O_3 doped mullites (see Table 5.1) began with the work of Lührs *et al.*, and was continued with a thorough NMR investigation by King.[120, 124-126] They confirmed that the B dopant was incorporating into the structure as BO_3 using ^{11}B NMR, which also verified the varying B content in the samples. Their use of ^{29}Si and ^{27}Al NMR revealed structures identical to 3:2 mullite, presenting no discernible trends with increasing B content. However, due to the new information on mullite structure, revealed by the *supercell* enabled calculations in this study, the three B doped mullites have been reinvestigated using ^{27}Al 3QMAS 2D NMR.

5.5.1. ^{27}Al Results

The ^{27}Al 3QMAS 2D NMR spectra of 1 %, 4% and 6% B_2O_3 mullites are displayed in Figure 5.9. Except for the missing α-Al_2O_3 contaminant resonance, the same resonances are observed in the spectra of 3:2 and 2:1 mullite, confirming that the mullite structure can incorporate B without significant structural changes. The only other change occurs at the resonance ($\delta_{iso} \approx 80$ ppm), which was tentatively assigned to the $AlO_3\square$ moiety. Although
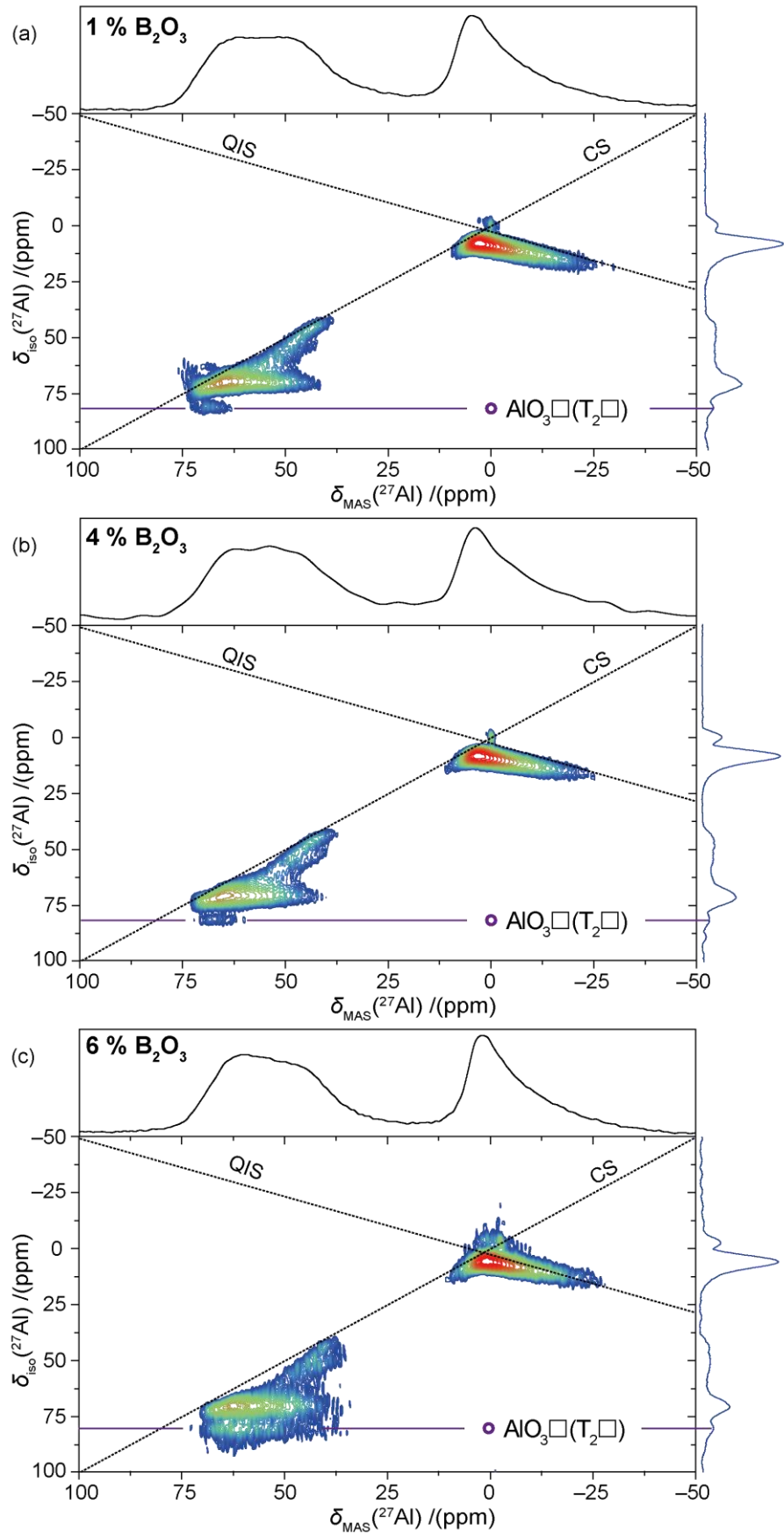
Figure 5.9 The ^{27}Al 3QMAS (20 KHz) NMR 2D spectrum of (a) 1 %, (b) 4% and (c) 6% B_2O_3 doped mullites at 14.1 T with the MAS spectrum above and the projected δ_{iso} spectrum on the right. The resonance corresponding to $AlO_3\square(T_2\square)$ is labelled.

100
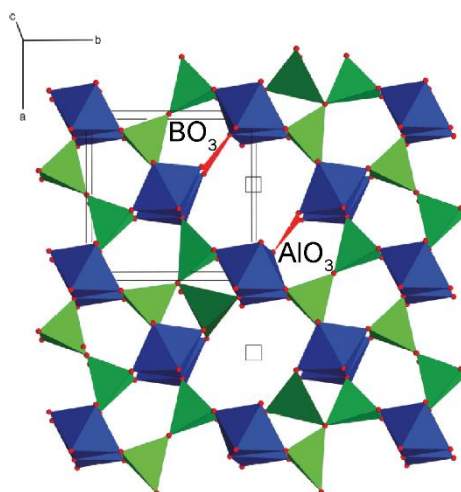
Figure 5.10 A diagram of the proposed boron doped mullite structure highlighting the possible configuration of BO_3 and AlO_3 units. The Al octahedra are in blue, the Al/Si tetrahedra are in green, the oxygen atoms are in black and the trigonal B and Al units are highlighted in red.

observable in the 2D spectrum, the low intensity resonance could not be distinguished in the projected δ_{iso} spectra for either aluminosilicate mullite. However, in all three of the B doped mullites the resonance is not only larger in the 2D spectrum, but clearly visible in the projected δ_{iso} spectra. The intensity of the resonance at $\delta_{iso} \approx 80$ ppm also increases as the B_2O_3 content increases. Although projected δ_{iso} spectra are not strictly quantitative,[133] it is clear that increasing B content increases the Al site occupancy of the $AlO_3\square$ moiety.

The current opinion on B doped mullites states that BO_3 substitutes for the tetrahedral units in the T_2O moiety, as represented in Figure 5.2. It is hypothesized that, due to their similar configuration in the structure, the BO_3 substitution may stabilise adjacent $AlO_3\square$ polyhedra (see Figure 5.10), encouraging their formation. Additionally, it is also possible that the increased number of vacancies introduced by the BO_3 substitution, inherently leads to an increase in $AlO_3\square$ sites. Regardless, the ^{27}Al NMR results on B doped mullite further justify the existence of the $AlO_3\square$ moiety in mullite.

5.6. Conclusions

This study has successfully answered several of the remaining questions about mullites structure. Firstly, the configuration of AlO_4 and SiO_4 units in 3:2 mullite was shown to lack order due to the success of the "random" approach over the "sillimanite" approach for structure generation. Secondly, the investigation provided a complete assignment of all

components in the ^{29}Si MAS spectrum of 3:2 mullite, confirming the existence of the T$_3$O moiety and conclusively proving the inclusion of SiO$_4$ tetrahedra in its formation.

Additionally, this study unveiled some new features of mullites structure. The ^{29}Si and ^{27}Al investigations determined the presence of quasi-tetrahedral polyhedra (AlO$_{4+1}$/SiO$_{4+1}$) that contain an additional long bond to a four-coordinate oxygen site. The discovery of the AlO$_{4+1}$ environment at ~50 ppm, allowed the previously reported assignments of the ^{27}Al MAS spectrum of mullite to be corrected. The ^{27}Al investigation also proposed AlO$_3\square$ as an environment in the mullite structure, which was verified by the investigation into boron doped mullites. In the B doped mullites, the AlO$_3\square$ environment was shown to increase in population with B content.

Unfortunately, the differences in structure between 3:2 and 2:1 mullite could not be confirmed with this method, due to the large amorphous SiO$_2$ contaminant in the 2:1 mullite sample. However, the close agreement of the *supercell* generated NMR simulations with the experimental ^{29}Si, ^{27}Al and ^{17}O NMR data on all the mullite samples proved the strength of the described methodology for the modelling of disordered systems, which could be applied to other catalyst systems.

6

The Study of Mullite-like Aluminoborates using Solid State NMR

6.1. Background

Mullite type materials consist of characteristic edge sharing octahedral chains along the *c*-axis, which are cross linked with three, four or five coordinated polyhedral motifs. As discussed in Chapter 5, several aluminosilicate phases, including those doped with small quantities of substitutional boron, belong to the mullite family. Figure 6.1 demonstrates the mullite type compositional field in the Al_2O_3 - SiO_2 - B_2O_3 ternary system, as reported by Werding and Schreyer.[134] The aluminoborates $Al_{18}B_4O_{33}$ ($9Al_2O_3{:}2B_2O_3$ or A9B2) and $Al_4B_2O_9$ ($2Al_2O_3{:}B_2O_3$ or A2B) are the two thermodynamically stable phases in the Al_2O_3 - B_2O_3 system.[135] Both phases are known to have mullite-like structures, however the complex details of both crystal structures are yet to be solved.[136-137]
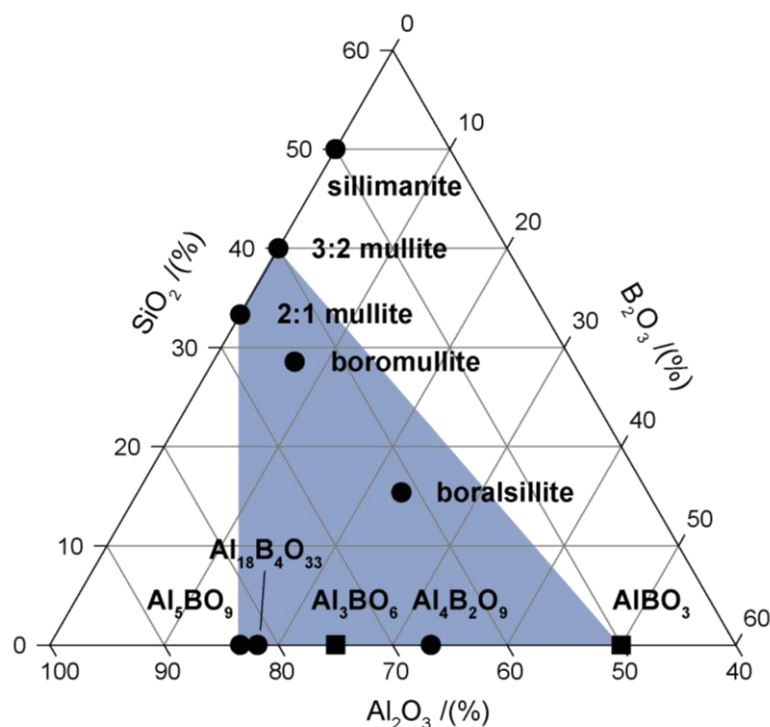
Figure 6.1 A ternary plot of the Al_2O_3 - SiO_2 - B_2O_3 system showing known compounds with mullite-like structures (●) and known compounds with structures differing from mullite's (■). The boron-mullite compositional field is shown in blue.

The A9B2 phase has been utilised as a model sample for advanced quadrupolar ^{27}Al NMR techniques due to the ordered, yet convoluted, nature of its Al environments. Double rotation (DOR) NMR,[138] MQMAS NMR, ultrahigh field MAS NMR[139] and satellite transition spectroscopy (SATRAS)[140] have all been applied to the study of the material. Alongside ^{11}B MAS NMR, these studies have revealed a crystalline structure composed of AlO$_6$, AlO$_5$, AlO$_4$ and BO$_3$ polyhedra.[136] However, the exact chemical composition of this phase is still a matter of debate. Various chemical analyses have provided the stated composition of Al$_{4.1}$B$_{0.9}$O$_9$ (termed A9B2).[135, 141-142] In contrast, crystallographic structure refinements, with an ordered distribution of Al and B, suggest a composition closer to Al$_5$BO$_9$ (A5B rather than A9B2).[136, 143] The crystal structure reported by Garsche et $al.$ is shown in Figure 6.2(a).[143] A substitution of less than 2 % of Al atoms with B in the A5B composition would yield A9B2. This discrepancy in the two proposed compositions has previously been rationalised by the possibility of a solid solution of Al and B at the tetrahedral site, with 9 % of AlO$_4$ sites replaced with BO$_4$. However, Fisch et $al.$ found no evidence of BO$_4$ sites in their ^{11}B MAS NMR investigation.[136] In this thesis, the phase will be termed A9B2 throughout, following the nomenclature used by the majority of the literature to avoid confusion. A9B2 is commercially available under the trade names $Alborex$ and $Alborite$.

The A2B phase has a structure closely related to that of boralsilite (Al$_{16}$Si$_2$B$_6$O$_{37}$; see Figure 6.1), with B replacing Si sites. Fischer et $al.$ confirmed the presence of AlO$_6$, AlO$_5$, AlO$_4$, BO$_4$ and BO$_3$ motifs using ^{11}B and ^{27}Al MAS NMR. They reported the crystal structure shown in Figure 6.2(b).[97] At certain sites boron can exist as three or four-coordinate, with the BO$_4$ moiety having an additional bond to an adjacent bridging oxygen. In the BO$_4$ environment, this oxygen site is shared by three tetrahedral units analogous to the observed T$_3$O sites in aluminosilicate mullites (Chapter 5). The variation in coordination at the B site and the displacement of the adjacent O creates the disorder that is observed by NMR. The exact details of the oxygen disorder and the positions of the BO$_4$ moieties are not solved yet.

A series of Al$_{6-x}$B$_x$O$_9$ compounds (where $1 \leq x \leq 3$) can be synthesized between the two stable A9B2 and A2B phases.[144] Further heat treatment of these phases yields either A9B2 or A2B, hence the phases are thought to be metastable. The disordered structure of this series of aluminoborate compounds (Figure 6.2(c)) is close to that of mullite. Mackenzie et $al.$ have previously performed an ^{11}B and ^{27}Al NMR study on a similar series of compounds.[145] They revealed the presence of both BO$_4$ and BO$_3$ sites in the structure, where an increase in B content caused an increase in the BO$_4$:BO$_3$ ratio. Their tentative ^{27}Al NMR assignments

show the structure to be composed of two AlO_6 motifs and three AlO_5/AlO_4 motifs, where the configuration of the three non-octahedral motifs varies with boron content. They showed that the structure contained one AlO_5 and two AlO_4 sites at low B content, whereas at high B content an additional AlO_5 unit replaced one of the AlO_4 sites.

The A9B2 and A2B ceramics are of high research interest due to their novel properties, which include: high elastic modulus, high tensile strength, low thermal expansion, low thermal conductivity and high corrosion resistance.[146-148] Hence, aluminoborates have

(a) $Al_{18}B_4O_{33}$ (A9B2)   (b) $Al_4B_2O_9$ (A2B)
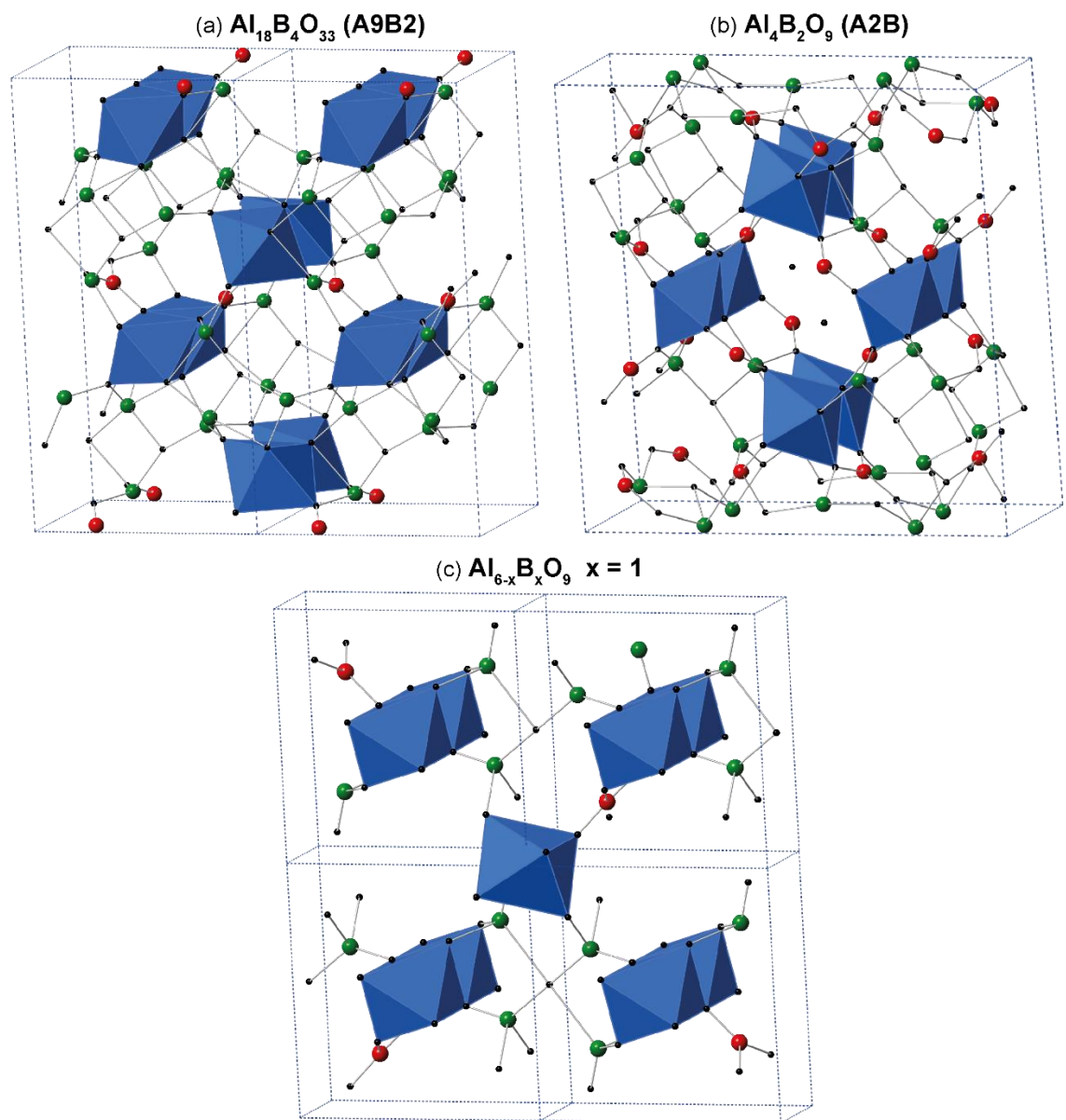
(c) $Al_{6-x}B_xO_9$ x = 1

Figure 6.2 The reported crystal structures of the three aluminoborate phases (a) A9B2, (b) A2B and (c) $Al_{6-x}B_xO_9$. AlO_6 octahedra are in blue and Al, B and O atoms are in green, red and black respectively.

applications in optics, tribology, fire insulation, nuclear reactor components, refractory linings, nanomaterials and structural materials.[143, 149-153] The majority of structural applications focus on the utilisation of aluminoborate needles or whiskers for the reinforcement of other materials, such as light metals (Al, Mg), other ceramics, and epoxy resins. [154-157] Most relevant to this thesis is the role of aluminoborates in catalysis. Due to their refractory nature and their ability to be prepared with a high surface area, they are well suited as catalyst materials. Aluminoborates are most commonly used as solid acid catalysts, which are important to many industrial reactions such as catalytic reforming, cracking, isomerisation, and (de)alkylation.[158-160] Similarly to aluminosilicate mullites, they are also used as a catalyst support.[161-163] Multiple studies have shown that varying the synthesis and composition of these materials has a significant effect on the acidity and activity of the catalysts.[158-160]

This investigation aims to produce a detailed structural characterisation of the phases in the Al_2O_3 - B_2O_3 system using ^{11}B and ^{27}Al solid state NMR. The structural changes of the A9B2, A2B and metastable $Al_{6-x}B_xO_9$ phases are investigated as a function of initial B content. Solid state and sol-gel synthesized A9B2 samples are also compared to the commercially available materials.

6.2. Experimental

6.2.1. Synthesis

Three series of powder samples with varying precursor Al/B ratios were produced for this investigation: the A9B2 phase series (A), the A2B phase series (B), and the metastable $Al_{6-x}B_xO_9$ series (C). The synthesis method and initial precursor composition (in wt% Al_2O_3/B_2O_3) of each compound is given in Table 6.1. *Alborite* and *Alborex* were obtained from Shikoku Chemical Corporation (Japan). The synthesis of all remaining samples was performed by K. Hoffman (Universität Bremen) and complete details of the methodology have been reported previously.[59, 164]

Samples A1-A3, series B and series C were all synthesised via a sol-gel method. Stochiometric amounts of aluminium nitrate nonahydrate ($Al(NO_3)_3 \cdot 9H_2O$) and boric acid (H_3BO_3) were dissolved in glycerol to produce a gel. The gels are then crystallised at 1373 K for 5 hrs, 1223 K for 44 hrs, or 1173 K for 6hrs to produce the A9B2, A2B, and $Al_{6-x}B_xO_9$ phases, respectively. Samples A4, A5 and A6 (A9B2 phase) were synthesized via a solid

Sample	Method	Initial comp.	
		Al_2O_3 /(wt%)	B_2O_3 /(wt%)
Alborite	-	-	-
Alborex	-	-	-
A1	G	82.0	18.0
A2	G	80.4	19.6
A3	G	47.6	52.4
A4	S	82.0	18.0
A5	S	80.4	19.6
A6	S	57.7	42.3
B1	G	70.0	30.0
B2	G	65.0	35.0
B3	G	60.0	40.0
B4	G	35.0	65.0
C1	G	86.8	13.2
C2	G	83.0	17.0
C3	G	80.0	20.0
C4	G	77.5	22.5
C5	G	74.6	25.4

Table 6.1 The synthesis methods and initial compositions of the three series of aluminoborates studied: A (A9B2), B (A2B) and C ($Al_{6-x}B_xO_9$). The initial compositions are given in corresponding ratios of Al_2O_3 and B_2O_3.
G - sol-gel method; S - solid state method

state reaction. Powdered α-Al_2O_3 and B_2O_3 were mixed in corresponding ratios (Table 6.1), pressed into a pellet and crystallised at 1473 K for 10 hrs.

Hoffman *et al.* verified the phases of the samples in series A and B (as A9B2 and A2B respectively) with XRD.[164] The precursor ratios of series C indicate compositions of $Al_{6-x}B_xO_9$ where x = 1.09, 1.38, 1.61, 1.79 and 2 for C1, C2, C3, C4, and C5 respectively. However, due to volatilisation of boron during synthesis the actual composition of the product may be different to the initial composition.

6.2.2. Solid State NMR Measurements

The MAS NMR experiments in this study were performed at room temperature across a range of different magnetic field strengths (B_0) using Varian-600 (14.1 T), Bruker Avance II+-600 (14.1 T), and Bruker Avance III HD-400 (9.40 T) spectrometers. All NMR data was processed using *TOPSPIN* and MQMAS data was sheared using the *TOSPSPIN* program *xfshear*. Simulations of non-quadrupolar ($C_Q = 0$) lineshapes (Gaussian) and second-order quadrupolar lineshapes were performed with *dmfit*.[49] Disordered quadrupolar lineshapes, which have a Gaussian distribution of C_Q values, were simulated using *QuadFit*.[13] The distributions are defined by a C_Q centre, a C_Q width and a broadening factor (Δ).

The ^{11}B NMR experiments were performed at 14.1 T (υ_0 (^{11}B) = 192.50 MHz) with an MAS frequency of 12 KHz. The experiments were completed using a boron-free Varian 4 mm HXY MAS probe with all data referenced with respect to NaBH$_{4(s)}$ (δ_{iso} = −42.06 ppm). A $^\pi/_2$ pulse length was determined on NaBH$_{4(s)}$ resulting in a selective $^\pi/_2$ pulse length of 5 μs being used, with a recycle delay of 20 s used throughout. The quantitative nature of these experiments was tested on selected samples, by comparison with experiments using smaller flip angles that satisfy the uniform excitation condition for quadrupolar nuclei (see Equation 2.21). In this case, a selective $^\pi/_9$ pulse length of 1.1 μs was used resulting in a much longer acquisition time (>24 hr). The difference in relative ratio of the intensity of BO$_3$ and BO$_4$ resonances was negligible and therefore the longer experiment was deemed unnecessary.

The ^{27}Al NMR experiments were performed at 14.1 T (υ_0 (^{27}Al) = 156.34 MHz) and 9.40 T (υ_0 (^{27}Al) = 104.23 MHz) with an MAS frequency of 20 KHz. The experiments were completed using a Bruker 3.2 mm HX probe with all data referenced with respect to yttrium aluminium garnet$_{(s)}$ (YAG; Y$_3$Al$_5$O$_{12}$; δ_{iso}[AlO$_6$] = 0.7 ppm). A $^\pi/_2$ pulse length was determined on YAG$_{(s)}$ resulting in a selective $^\pi/_6$ pulse length of 0.8 μs and 1 μs being used for the single-pulse experiments at 14.1 T and 9.40 T, respectively. At 9.40 T a recycle delay of 10 s was utilised, whereas a shorter delay of 2 s was used at 14.1 T to minimise experimental time. The 14.1 T 2D MQMAS experiments utilised a *z*-filtered 3QMAS pulse sequence with a 3.5 μs excitation pulse, a 1.5 μs conversion pulse and a 17.0 μs selective *z*-filter pulse.

6.3. The A9B2 Phase

6.3.1. ^{11}B Solid State NMR

The ^{11}B MAS NMR spectra of the A9B2 samples (series A) is presented in Figure 6.3. The NMR parameters are determined via simulated fitting of each spectrum and the results are given in Table 6.2. As expected, each spectrum is dominated by a second-order quadrupolar broadened lineshape with parameters indicative of trigonal planar BO_3 ($C_Q \approx 2.6$ MHz, $\delta_{iso} \approx 16.5$ ppm, and $\eta_Q \approx 0.07$ - 0.120).[2] The ^{11}B lineshape of *Alborex* is subtly distinct from the rest of the species. In Figure 6.3(b) the low frequency shoulder of the BO_3 resonance is raised, which is not matched by the simulated second-order quadrupole lineshape. This is due to the whisker macrostructure of *Alborex*, as observed by Hoffman *et al.* using scanning electron microscopy (SEM) imaging.[164] The stacking of the needle shaped crystal formations in the NMR rotor causes a preferred orientation of crystals, altering the second-order quadrupolar powder pattern (see Chapter 1.4.1). Under MAS conditions, this results in an increase in intensity at the low frequency shoulder position.[7, 165]

Each sample also presents with small resonances at δ_{iso} values between 2.6 and −0.7 ppm, which are assigned to BO_4 moieties.[2] Fisch *et al.* did not observe these environments with ^{11}B NMR as they were obscured by the broad BO_3 resonance, a product of the lower B_0 field used in their study.[136] The detection of BO_4 environments confirms the hypothesis that a solid solution of AlO_4 and BO_4 units is present in the A9B2 structure. This explains the different chemical compositions given by structural refinements and chemical analysis in the literature. The BO_4 to BO_3 ratio increases with increasing initial B content for both synthesis methods in series A, which is concurrent with the replacement of AlO_4 sites with BO_4 units. The varied BO_4 content of the compounds in series A (Table 6.2) suggests a range of compositions close to $Al_{18}B_4O_{33}$, which has been confirmed previously by prompt gamma neutron activation analysis (PGAA).[164] The majority of the compounds in series A have multiple BO_4 components (Figure 6.3), indicating disorder at the BO_4 site.

6.3.2. ^{27}Al Solid State NMR

The ^{27}Al MAS NMR spectra of the A9B2 samples (series A) is presented in Figure 6.4. Due to the convoluted nature of the MAS lineshape, ^{27}Al 2D 3QMAS NMR experiments (Figure 6.5) were performed on a selected range of samples: Alborite, A1, A4 and A6. The 3QMAS
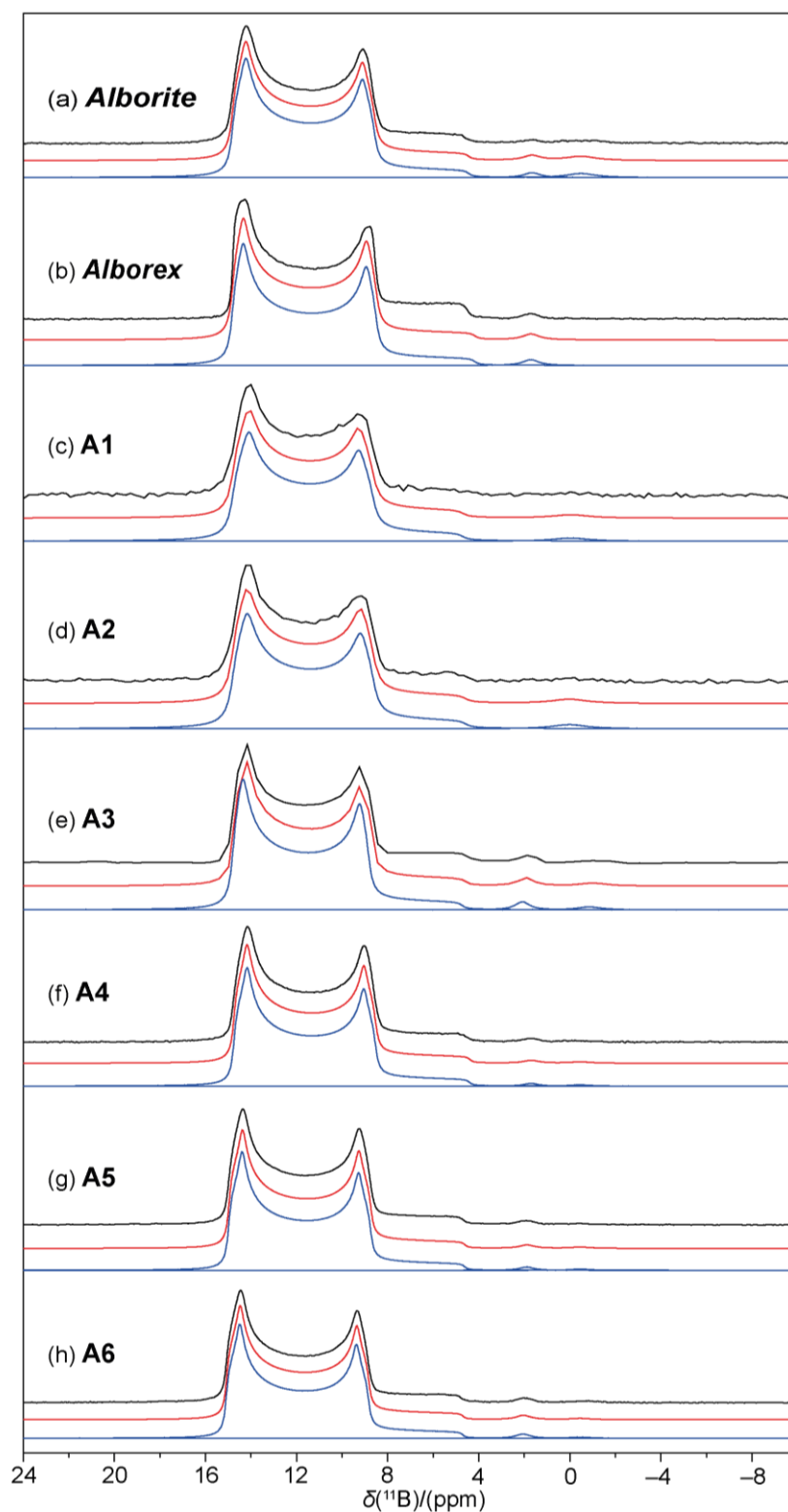
Figure 6.3 The ^{11}B MAS (12 KHz) NMR spectra at 14.1 T of series A (A9B2): (a) *Alborite*, (b) *Alborex*, (c) A1, (d) A2, (e) A3, (f) A4, (g) A5 and (h) A6. The experimental spectra, the simulated lineshapes and the deconvoluted resonances are presented in black, red and blue, respectively.

Sample	δ_{iso} /(ppm) (± 0.5)	C_Q /(MHz) (± 0.1)	η_Q (± 0.01)	FWHM /(KHz) (± 0.05)	Species	Intensity /(%) (± 0.5)	Species Int. /(%) (± 0.5)
	16.5	2.6	0.09	-	BO_3	97.9	97.9
Alborite	2.4	-	-	0.12	BO_4	0.5	2.1
	0.2	-	-	0.46		1.6	
Alborex	16.7	2.7	0.07	-	BO_3	98.4	98.4
	2.6	-	-	0.14	BO_4	1.6	1.6
A1	16.5	2.6	0.12	-	BO_3	99.3	99.3
	0.2	-	-	0.19	BO_4	0.7	0.7
A2	16.5	2.6	0.11	-	BO_3	98.4	98.4
	0.7	-	-	0.39	BO_4	1.6	1.6
	16.6	2.6	0.09	-	BO_3	97.1	97.1
A3	2.5	-	-	0.16	BO_4	2.0	2.9
	−0.7	-	-	0.29		0.9	
	16.3	2.6	0.09	-	BO_3	98.3	98.3
A4	2.3	-	-	0.20	BO_4	1.4	1.7
	0.3	-	-	0.20		0.3	
	16.3	2.6	0.09	-	BO_3	97.9	97.9
A5	2.3	-	-	0.22	BO_4	1.7	2.1
	0.0	-	-	0.25		0.4	
	16.4	2.6	0.09	-	BO_3	97.5	97.5
A6	2.3	-	-	0.19	BO_4	1.9	2.5
	−0.3	-	-	0.21		0.6	

Table 6.2 The ^{11}B NMR parameters of series A (A9B2) determined via simulated fitting.
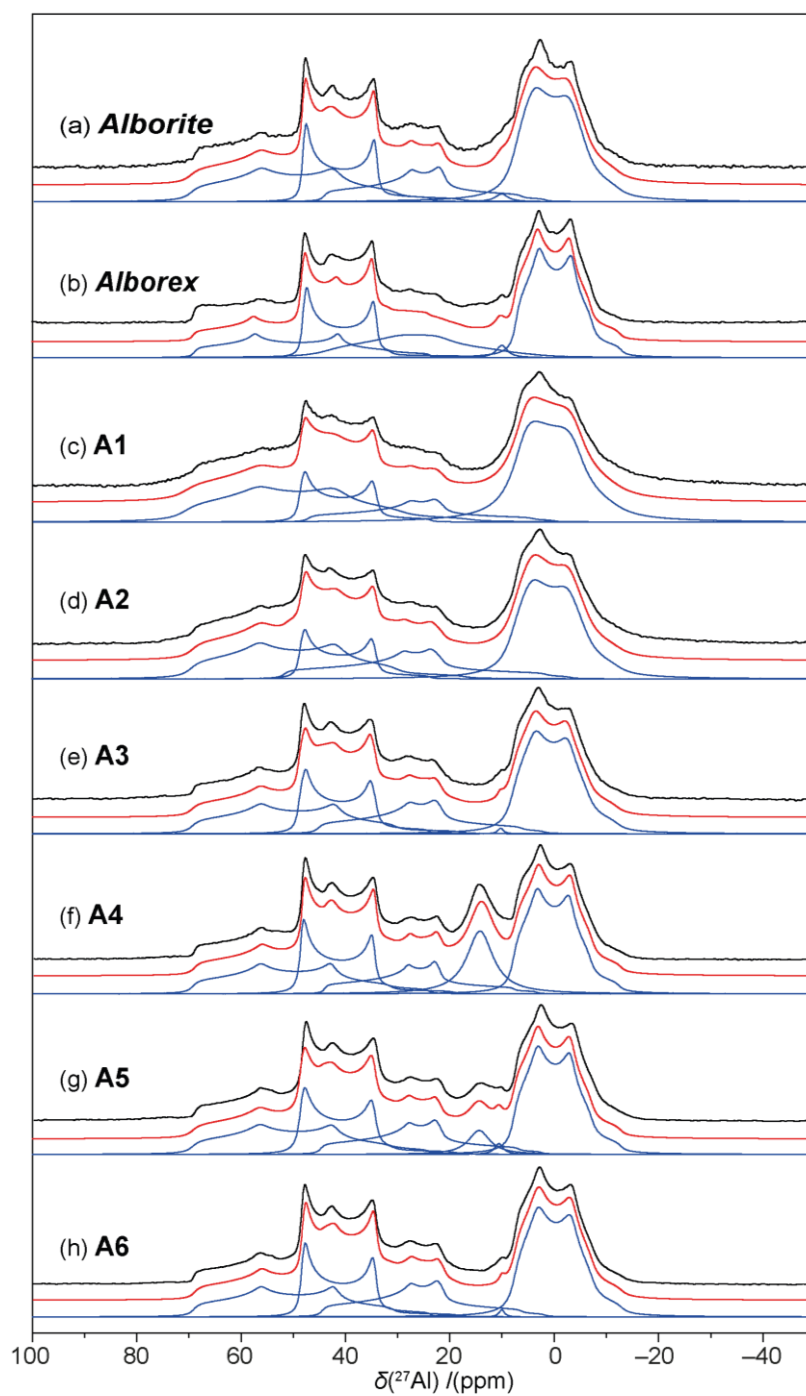
Figure 6.4 The ^{27}Al MAS (20 KHz) NMR spectra at 14.1 T of series A (A9B2): (a) *Alborite*, (b) *Alborex*, (c) A1, (d) A2, (e) A3, (f) A4, (g) A5 and (h) A6. The experimental spectra, the simulated lineshapes and the deconvoluted resonances are presented in black, red and blue, respectively.

Figure 6.5 The ^{27}Al 2D 3QMAS (20 KHz) NMR spectra at 14.1 T of selected (a) alborite, (b) A1, (c) A4 and (d) A6. The MAS spectrum is displayed above and the projected δ_{iso} spectrum on the right. Distinct resonances in the 2D spectrum are labelled with their assigned environments.

Sample	δ_{iso} /(ppm) (± 1)	C_Q /(MHz) (± 0.1)	η_Q (± 0.01)	FWHM /(KHz) (± 0.05)	Species	Intensity /(%) (± 1)	(w/o Al_2O_3)
	72	9.2	0.45	-	AlO_4	24	24
	52	6.8	0.04	-	AlO_5	18	18
Alborite	45	8.0	0.75	-	AlO_5	16	16
	10	-	-	0.46	AlO_6	1	1
	9	5.8	0.30	-	AlO_6	42	42
	72	9.3	0.38	-	AlO_4	18	18
	52	6.8	0.05	-	AlO_5	20	20
Alborex	44	7.9	0.63	-	AlO_5	20	20
	10	-	-	0.40	AlO_6	2	2
	9	5.8	0.37	-	AlO_6	42	42
	73	9.5	0.45	-	AlO_4	30	30
A1	52	6.9	0.06	-	AlO_5	14	14
	47	8.3	0.80	-	AlO_5	12	12
	9	5.8	0.06	-	AlO_6	44	44
	72	9.3	0.43	-	AlO_4	28	28
A2	52	6.8	0.06	-	AlO_5	14	14
	52	9.0	0.81	-	AlO_5	18	18
	9	5.9	0.30	-	AlO_6	40	40
	72	9.2	0.44	-	AlO_4	23	23
	52	6.8	0.08	-	AlO_5	20	20
A3	45	8.0	0.77	-	AlO_5	18	18
	10	-	-	0.20	AlO_6	1	1
	9	5.8	0.36	-	AlO_6	39	39

	71	9.1	0.45	-	AlO_4	20	23
	52	6.8	0.00	-	AlO_5	19	22
A4	44	7.8	0.75	-	AlO_5	14	16
	9	5.8	0.38	-	AlO_6	33	39
	14	-	-	6.13	Al_2O_3	14	-
	72	9.1	0.44	-	AlO_4	21	23
	52	6.8	0.04	-	AlO_5	20	21
	45	8.0	0.76	-	AlO_5	16	17
A5	10	-	-	0.32	AlO_6	1	1
	9	5.9	0.38	-	AlO_6	36	39
	13	-	-	1.16	Al_2O_3	7	-
	71	9.1	0.44	-	AlO_4	22	22
	52	6.8	0.04	-	AlO_5	20	20
A6	45	8.0	0.76	-	AlO_5	18	18
	10	-	-	0.20	AlO_6	1	1
	9	5.9	0.37	-	AlO_6	40	40

Table 6.3 The ^{27}Al NMR parameters of series A (A9B2) determined via simulated fitting.

data allowed accurate simulated fitting of the MAS lineshapes. The NMR parameters determined via simulated fitting of each spectra are given in Table 6.3.

Each sample is shown to contain one AlO_6, one AlO_4 and two AlO_5 sites as previously determined.[136, 138-140] The NMR parameters of each component are similar to those determined by Kunath *et al.* and Massiot *et al.*, although some variation occurs across the series.[140, 166] Similarly, the predicted site occupation ratio of 2:1:1:1 for AlO_6:AlO_5:AlO_5:AlO_4 is approximately followed throughout.[136] However, an additional small AlO_6 resonance is detected in the spectra of *Alborex*, A3, A5 and A6 (Figure 6.4(b, e, g, h)). This AlO_6 component is only observed in the compounds that have a high initial B content, and, hence, contain a high BO_4 content. Therefore, it is hypothesized that the AlO_6 units adjacent to the BO_4 unit are distorted by a decreased bond length, creating a distinct AlO_6 site. This hypothesis also explains the disorder seen at the BO_4 site by ^{11}B NMR (Figure

6.3). The smaller AlO_6 resonance has been fitted with a narrow Gaussian/Lorentzian lineshape in the simulations, despite the probable quadrupolar nature of the component. The small observed intensity is thought to be one of the singularities present in a full second-order quadrupole lineshape (see Figure 1.7), with the rest of the shape overshadowed by the larger AlO_6 resonance. There is tentative evidence for the second singularity of the proposed quadrupole lineshape at ~0 ppm in Figure 6.4(b).

The samples A4 and A5 (Figure 6.4(f, g)) have a resonance at ~14 ppm that is assigned to an amorphous α-Al_2O_3 impurity from the starting materials. The α-Al_2O_3 impurity only occurs in these high initial Al_2O_3 content samples produced via the solid state methodology, and its intensity increases with the initial Al_2O_3 content. The sol-gel samples A1 and A2, which were produced with the same initial Al_2O_3:B_2O_3 ratios, do not contain an observable quantity of α-Al_2O_3. This is replicated in the aluminosilicate mullites (Chapter 5), verifying that the α-Al_2O_3 is a by-product of the solid state synthesis method and that the sol-gel synthesis method provides a greater control over the end product.

The samples A1 and A2 (Figure 6.4(c, d)) are observed to have more disturbed lineshapes in their MAS spectra. This is visible in the AlO_6 resonances, which are less accurately fitted by the simulations. Additionally, both present an increased AlO_4:AlO_5 ratio with the intensity of the AlO_4 components reaching ~30 %. This is believed to be due to local disorder in the crystal structure of the high initial Al content, sol-gel synthesized systems, as disorder effects were also detected in the diffraction data acquired by Hoffman *et al.*.[164]

6.4. The A2B Phase

6.4.1. ^{11}B Solid State NMR

The ^{11}B MAS NMR spectra of the set of A2B samples (series B) is presented in Figure 6.6. The NMR parameters determined via simulated fitting of each spectra are given in Table 6.4. The ^{11}B NMR spectra confirm the presence of both BO_3 and BO_4 components in the A2B phase. For each of the samples the trigonal BO_3 moiety is represented by a second-order quadrupole lineshape with a C_Q of 2.6 ± 1 MHz, a δ_{iso} of 16.8 ± 1 ppm and a η_Q of 0.11 ± 0.01. The BO_4 resonances fall into the δ_{iso} range of 1.0 to −1.3 ppm.
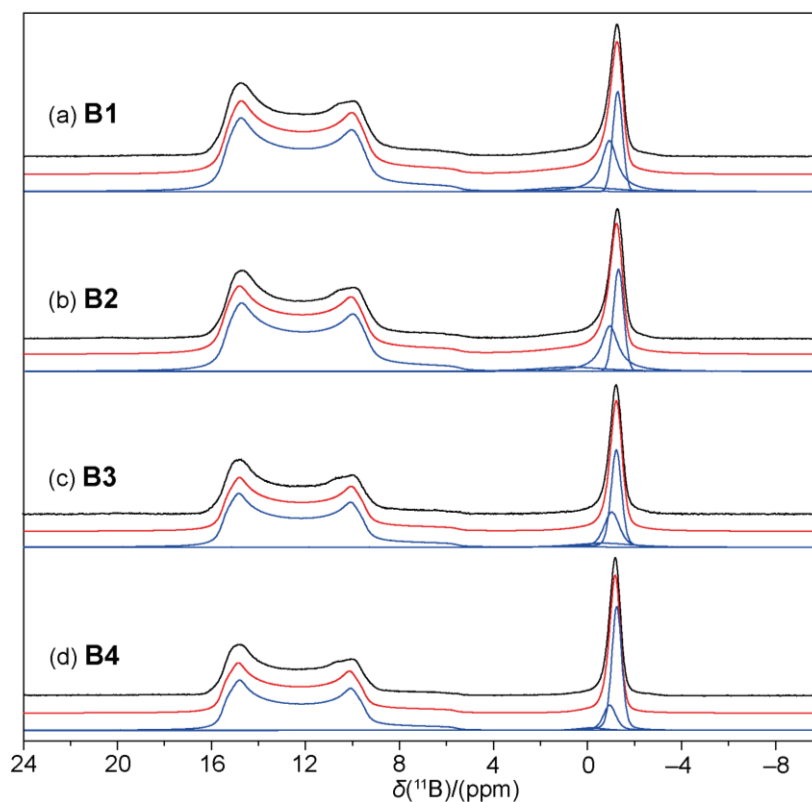
Figure 6.6 The ^{11}B MAS (12 KHz) NMR spectra at 14.1 T of series B (A2B): (a) B1, (b) B2, (c) B3 and (d) B4. The experimental spectra, the simulated lineshapes and the deconvoluted resonances are presented in black, red and blue, respectively.
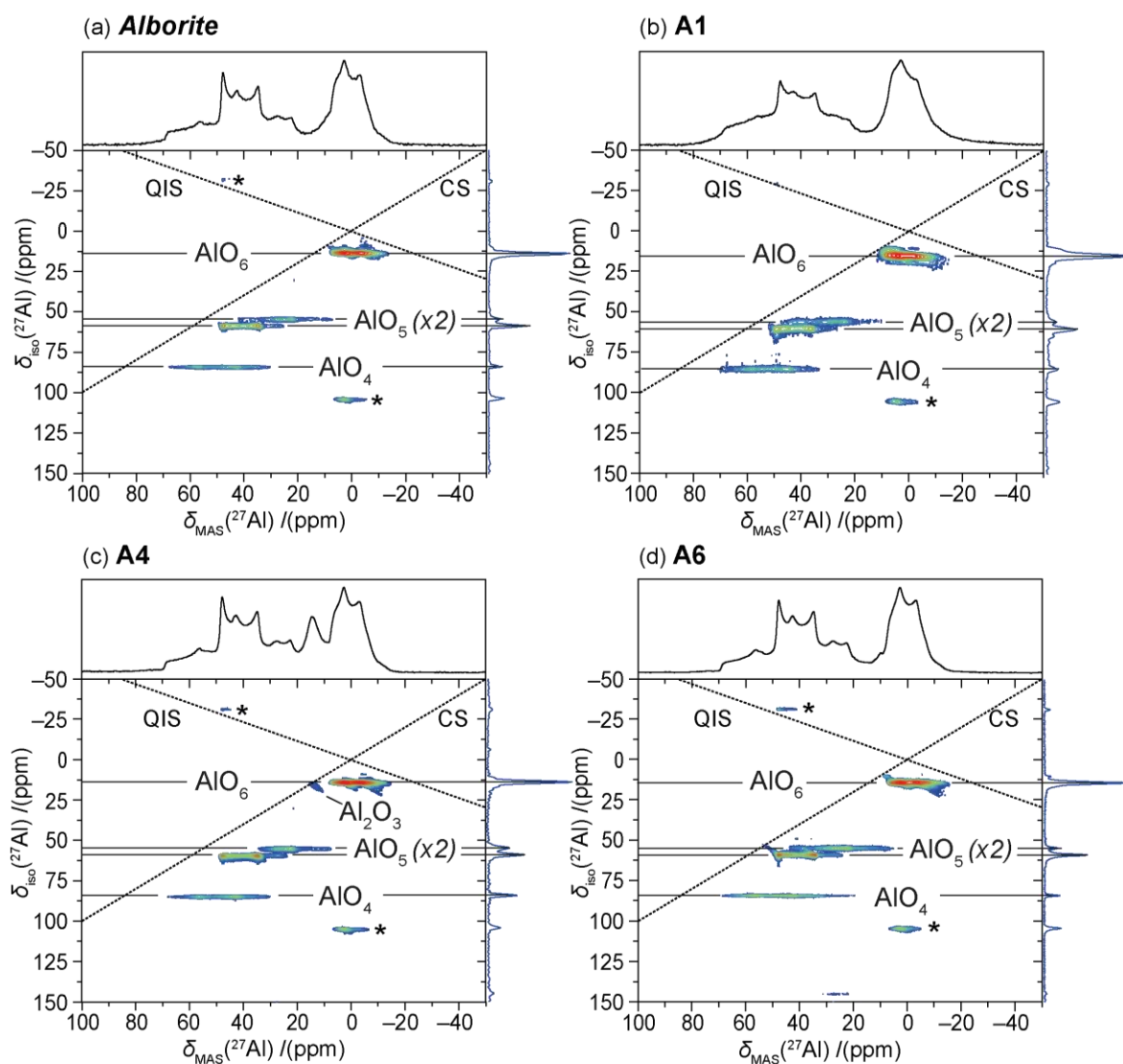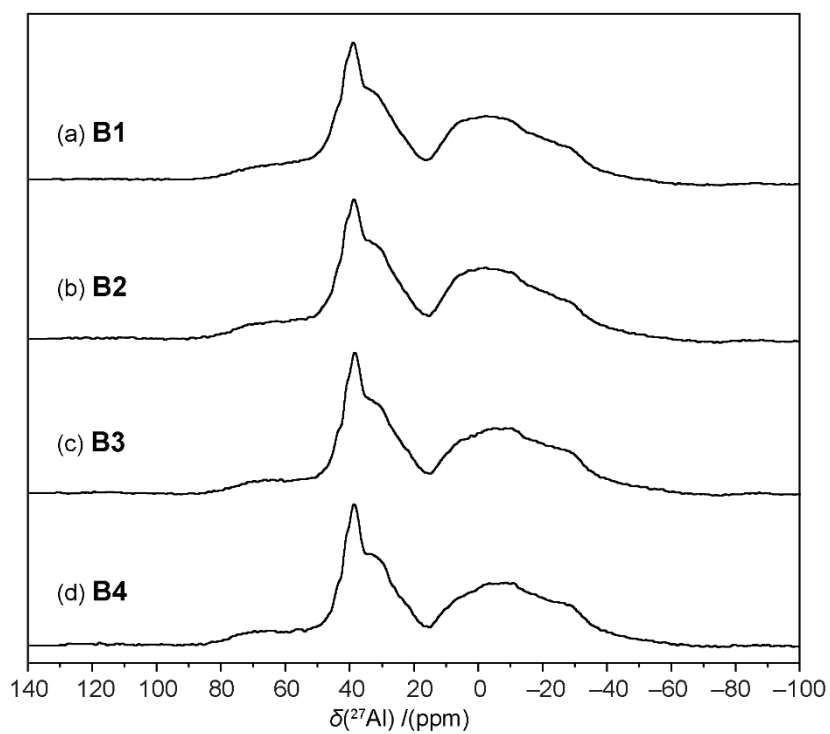

Figure 6.7 The ^{27}Al MAS (20 KHz) NMR spectra at 14.1 T of series B (A2B): (a) B1, (b) B2, (c) B3 and (d) B4.

Sample	δ_{iso} /(ppm) (± 0.5)	C_Q /(MHz) (± 0.1)	η_Q (± 0.01)	FWHM /(KHz) (± 0.05)	Species	Intensity /(%) (± 0.5)	Species Int. /(%) (± 0.5)
	16.8	2.6	0.11	-	BO_3	73.8	73.8
B1	0.5	-	-	0.72		3.1	
	−0.9	-	-	0.16	BO_4	13.2	26.2
	−1.3	-	-	0.09		9.9	
	16.8	2.6	0.11	-	BO_3	73.0	73.0
B2	1.0	-	-	0.70		2.6	
	−0.9	-	-	0.17	BO_4	12.1	27.0
	−1.3	-	-	0.10		12.3	
	16.8	2.6	0.11	-	BO_3	71.3	71.3
B3	−0.7	-	-	0.55		4.1	
	−1.1	-	-	0.15	BO_4	8.5	28.7
	−1.3	-	-	0.10		16.1	
	16.8	2.6	0.11	-	BO_3	69.1	69.1
B4	−0.1	-	-	0.23		2.4	
	−1.0	-	-	0.12	BO_4	8.1	30.9
	−1.2	-	-	0.09		20.4	

Table 6.4 The ^{11}B NMR parameters of series B (A2B) determined via simulated fitting.

The relative site occupancies of BO_4 to BO_3 determined by the ^{11}B MAS NMR results disagree with those predicted by Fischer *et al.*.[97] Their crystal structure refinements suggest a maximum relative BO_4 site occupancy of 25 %, which is at odds with the 31 % occupancy determined on sample B4. Similarly to the A9B2 phase (Chapter 6.4.1), there is an observed trend of increasing BO_4 relative site occupancy ($BO_4:BO_3$ ratio), with the increasing initial B content. Therefore, the extra BO_4 content is hypothesised to be due to the substitution of B into tetrahedral Al sites, as observed in the A9B2 phase. This substitution would result in an additional BO_4 environment in the structure. The multiple BO_4 sites observed in the [11]B

spectra (Table 6.4) lend credence to this hypothesis. Additionally, the decreased bond length of the BO_4 units, compared to AlO_4, would result in disorder at the site. Therefore, this hypothesis could also justify the disordered oxygen configuration detected via diffraction.[164]

6.4.2. ^{27}Al Solid State NMR

The ^{27}Al MAS NMR spectra of the set of A2B samples (series B) is presented in Figure 6.7. Due to the extremely convoluted nature of the lineshapes, ^{27}Al 2D 3QMAS NMR experiments, alongside additional ^{27}Al MAS NMR experiments at 9.40 T, were performed on selected samples: B1 and B4 (Figure 6.8). The deconvolutions of the 1D MAS spectra of B1 and B4 were constrained by simulating the MAS spectra at two different fields (14.1 T and 9.40 T) and by simulating the 3QMAS projections of each site. This thorough methodology provides confidence in the accurate simulation of complicated quadrupolar spectra. The NMR parameters determined via simulated fitting of the spectra for B1 and B4 are given in Table 6.5.

The spread of the contours along the QIS axis in the 2D 3QMAS data, and the long asymmetric tails of the resonances in the 1D MAS spectra, are indicative of significant distributions in the quadrupolar parameters of each component. Hence, the ^{27}Al NMR data proves that the A2B structure is characterized by significant short-range disorder, especially when compared to A9B2. The spectra of B1 and B4 can be deconvoluted into 6 distinct components assigned as four AlO_4/AlO_5 sites and two AlO_6 sites. The relative site occupancy of six-coordinated sites is ~50 % for both compounds which is in good agreement with the previous ^{27}Al data on A2B, reported by Fischer *et al.*.[97] However, the thorough ^{27}Al NMR investigation reported here, improves on the published material by clearly distinguishing four non-octahedral sites, rather than three. This provides a better match with the published refined crystal structure which details the distinct Al sites as two AlO_4, two AlO_5 and three AlO_6 environments. Two of the crystallographic AlO_6 sites are thought to be insufficiently distinct to be resolved by NMR, hence the difference in the number of six-coordinated sites observed in the NMR and the crystallographic data.

Additionally, the refined crystal structure reports two AlO_4 sites whereas the corresponding NMR resonances are assigned to one AlO_4 and one AlO_{4+1} moiety. The AlO_{4+1} moeity is a quasi-tetrahedral unit with an additional long bond to an adjacent O. This assignment is parallel to the discovery of an AlO_{4+1} moiety in aluminosilicate mullites. The moiety is
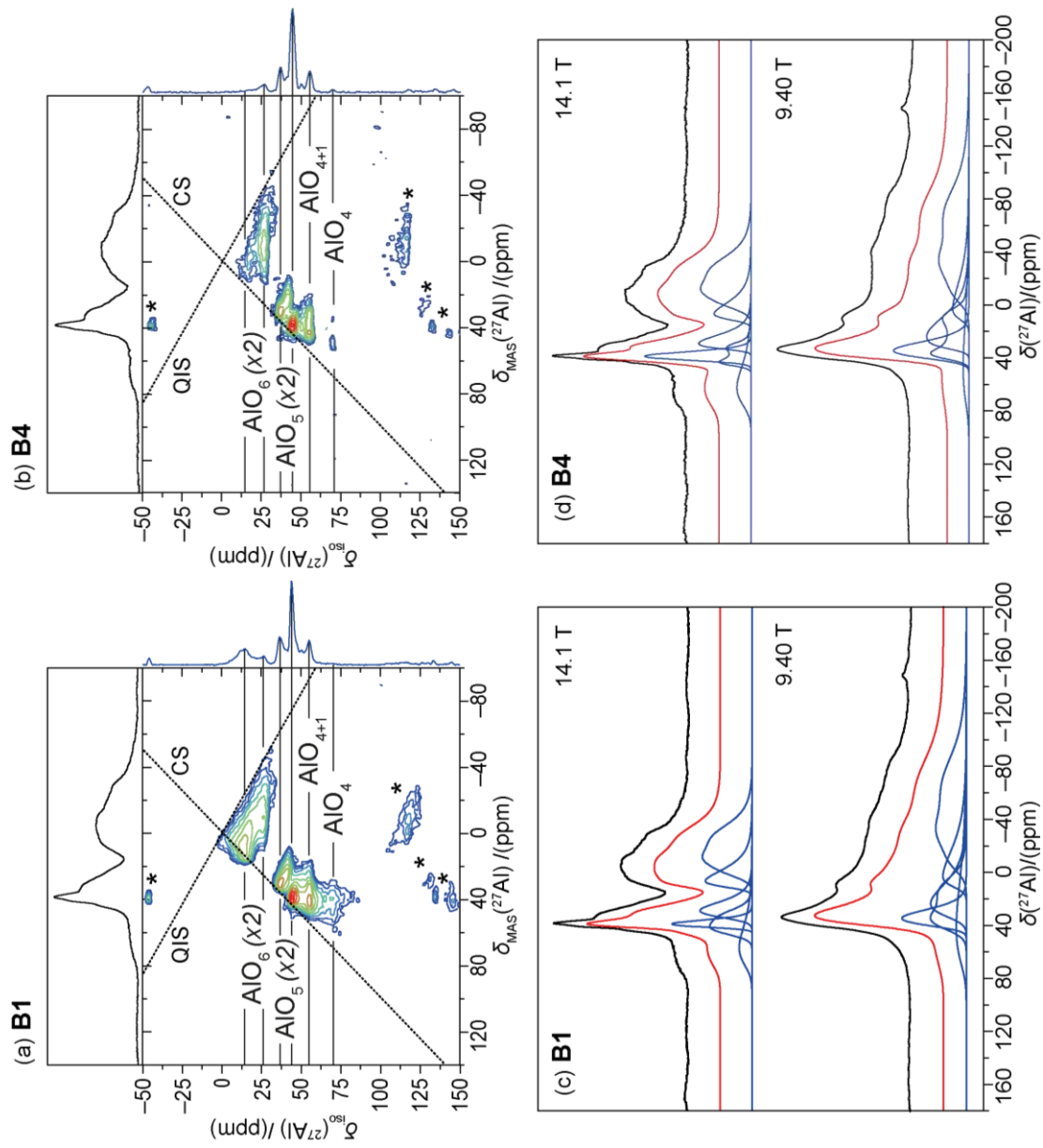
Figure 6.8 The ^{27}Al 2D 3QMAS (20 KHz) NMR spectra at 14.1 T of (a) B1 and (b) B4. The MAS spectrum is displayed above and the projected δ_{iso} spectrum on the right. Distinct resonances in the 2D spectrum are labelled with their assigned environments. The ^{27}Al MAS (20 KHz) NMR spectra at 14.1 T and 9.40 T for (c) B1 and (d) B4. The experimental spectra, the simulated lineshapes and the deconvoluted resonances are presented in black, red and blue, respectively.

Sample	δ_{iso} /(ppm) (± 1)	C_Q centre /(MHz) (± 0.1)	C_Q width /(MHz) (± 0.1)	η_Q (± 0.01)	Δ /(KHz) (± 0.1)	Species	Intensity /(%)	Species Int. /(%)
	7	10.1	2.0	0.4	1.6	AlO_6	34 ± 1	48 ± 2
	11	5.6	4.5	1.0	0.9	AlO_6	14 ± 2	
B1	34	4.9	3.3	1.0	0.7	AlO_5	15 ± 1	42 ± 2
	42	4.0	1.4	0.5	0.7	AlO_5	11 ± 1	
	49	6.9	1.1	0.0	1.5	AlO_{4+1}	16 ± 1	
	71	8.0	4.9	1.0	2.8	AlO_4	10 ± 1	10 ± 1
	6	10.1	2.0	0.4	1.6	AlO_6	36 ± 1	47 ± 2
	11	5.6	4.5	1.0	0.9	AlO_6	11 ± 2	
B4	34	4.9	3.3	1.0	0.6	AlO_5	16 ± 2	45 ± 4
	42	4.0	1.4	0.5	0.8	AlO_5	16 ± 1	
	49	7.1	0.8	0.0	1.0	AlO_{4+1}	13 ± 3	
	77	8.0	4.9	1.0	2.8	AlO_4	9 ± 2	9 ± 2

Table 6.5 The ^{27}Al NMR parameters of series B (A2B) determined via simulated fitting using a Gaussian distribution of C_Q.

represented by a component with a δ_{iso} of 49 ± 1 ppm, which is corroborated by the similar NMR parameters observed for the AlO_{4+1} site in mullite (Chapter 5.3.2).

The ^{27}Al MAS spectra of series B (Figure 6.6) do not exhibit any observable trends and the determined NMR parameters of the resonances in B1 and B4 are close to identical. Therefore, the varied BO_4 content, and the varied initial B content that precedes it (see Chapter 6.4.1), appear to have no effect on the overall structure of the A2B phase.

6.5. The Metastable $Al_{6-x}B_xO_9$ Phase

6.5.1. ^{11}B Solid State NMR

The ^{11}B MAS NMR spectra of the metastable $Al_{6-x}B_xO_9$ samples (series C) is presented in Figure 6.9. The NMR parameters determined via simulated fitting of each spectra are given in Table 6.6. The ^{11}B NMR spectra of series C are analogous to those of the A2B phase (see Figure 6.6) as both contain a trigonal BO_3 resonance ($C_Q \approx 2.6$ MHz, $\delta_{iso} \approx 16.8$ ppm and $\eta_Q \approx 0.15$), multiple BO_4 resonances (δ_{iso} values between 1.6 and −1.1 ppm), and a trend of increasing BO_4 relative site occupancy with the increasing B content. As discussed for both the stable phases, the multiple BO_4 resonances indicate some local disorder at this site.

The major differences occur in the larger range of BO_4 site occupancies that the C series contains. The site is virtually unpopulated (1 %) for sample C1 but increases up to 20% relative BO_4 site occupancy for sample C5, demonstrating a broad AlO_4/BO_4 solid solution. The structural model proposed by Mazza *et al.* for $Al_{6-x}B_xO9$, suggest that sample C5 should have 50 % BO_4, rather than the 20 % detailed in Table 6.6.[144] This demonstrates a clear preference of boron to populate a three-fold coordination and, therefore, the proposed structural model requires revaluation.

These findings are all in agreement with Mackenzie *et al.*'s ^{11}B NMR investigation of a similar series in the $Al_{6-x}B_xO_9$ phase.[145]
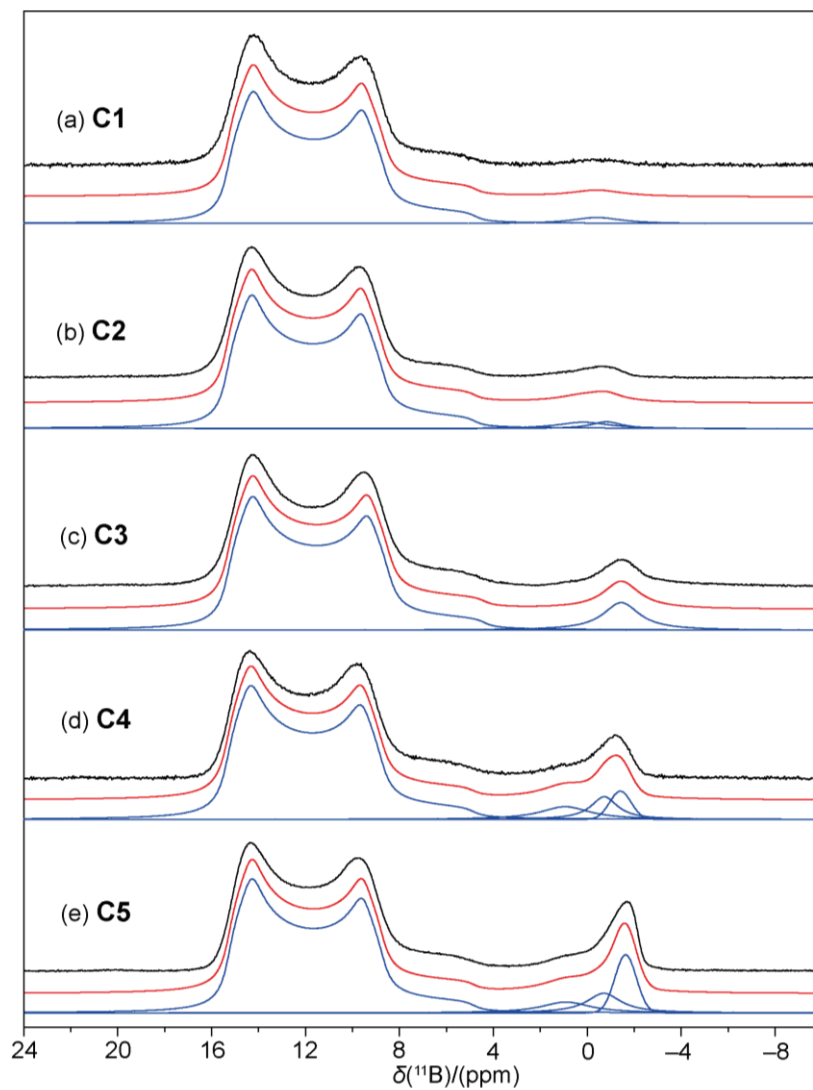
Figure 6.9 The ^{11}B MAS (12 KHz) NMR spectra at 14.1 T of series C ($Al_{6-x}B_xO_9$): (a) C1, (b) C2, (c) C3, (d) C4 and (e) C5. The experimental spectra, the simulated lineshapes and the deconvoluted resonances are presented in black, red and blue, respectively.

Sample	δ_{iso} /(ppm) (± 0.5)	C_Q /(MHz) (± 0.1)	η_Q (± 0.01)	FWHM /(KHz) (± 0.05)	Species	Intensity /(%) (± 0.5)	Species Int. /(%) (± 0.5)
C1	16.7	2.6	0.16	-	BO_3	98.7	98.7
	0.3	-	-	0.29	BO_4	1.3	1.3
C2	16.8	2.6	0.16	-	BO_3	96.2	96.2
	1.1	-	-	0.29	BO_4	1.6	3.8
	−0.1	-	-	0.22		2.2	
C3	16.8	2.6	0.15	-	BO_3	91.7	91.7
	−0.7	-	-	0.34	BO_4	8.3	8.3
C4	16.8	2.6	0.15	-	BO_3	85.5	85.5
	1.6	-	-	0.69		5.6	
	−0.2	-	-	0.24	BO_4	6.0	14.5
	−0.7	-	-	0.14		2.9	
C5	16.7	2.6	0.15	-	BO_3	80.2	80.2
	0.8	-	-	0.53		10.0	
	−0.6	-	-	0.23	BO_4	5.6	19.8
	−1.1	-	-	0.11		4.2	

Table 6.6 The ^{11}B NMR parameters of series C ($Al_{6-x}B_xO_9$) determined via simulated fitting.

6.5.2. ^{27}Al Solid State NMR

The ^{27}Al MAS NMR spectra of the $Al_{6-x}B_xO_9$ samples (series C) is presented in Figure 6.10. The ^{27}Al NMR investigation of series C was performed analogously to the investigation of series B (Chapter 6.4). Accurate deconvolution of the complex [27]Al MAS spectra for selected samples (C1, C3 and C5) was completed via the simultaneous simulation of multi-field (14.1 T and 9.40 T) MAS spectra and 3QMAS projections (Figure 6.11). The NMR parameters determined via simulated fitting of the spectra for C1, C3 and C5 are given in Table 6.7. Once again, the NMR results include significant distributions in the quadrupolar parameters

for each component, proving that the $Al_{6-x}B_xO_9$ structures are highly disordered despite longer range periodicity giving rise to measured diffraction data.[59] The 3QMAS data reveal that the structure of all three compounds consists of two AlO_6 sites, one AlO_{4+1} site, and an AlO_4 site. Samples C3 and C5 boast two additional AlO_5 sites (see Figure 6.11(c)) whereas sample C1 has an additional AlO_4 (see Figure 6.11(a)). In the ^{27}Al MAS NMR investigation of $Al_{6-x}B_xO_9$ compounds with similar initial contents as C3 and C5 performed by Mackenzie *et al.*, they could only distinguish three $AlO_{4/5}$ moieties rather than the four moieties discovered in this investigation.[145] Furthermore, the simulated fittings of the ^{27}Al data reveal the AlO_6 site occupancies to be split between a populated site and a marginally populated site, contrary to the results of Mackenzie *et al.*.[145] The highly resolved 3QMAS measurements reported here, alongside the thorough simulation methodology utilised, permit a more accurate identification of all the Al speciation, than in the previous reports.
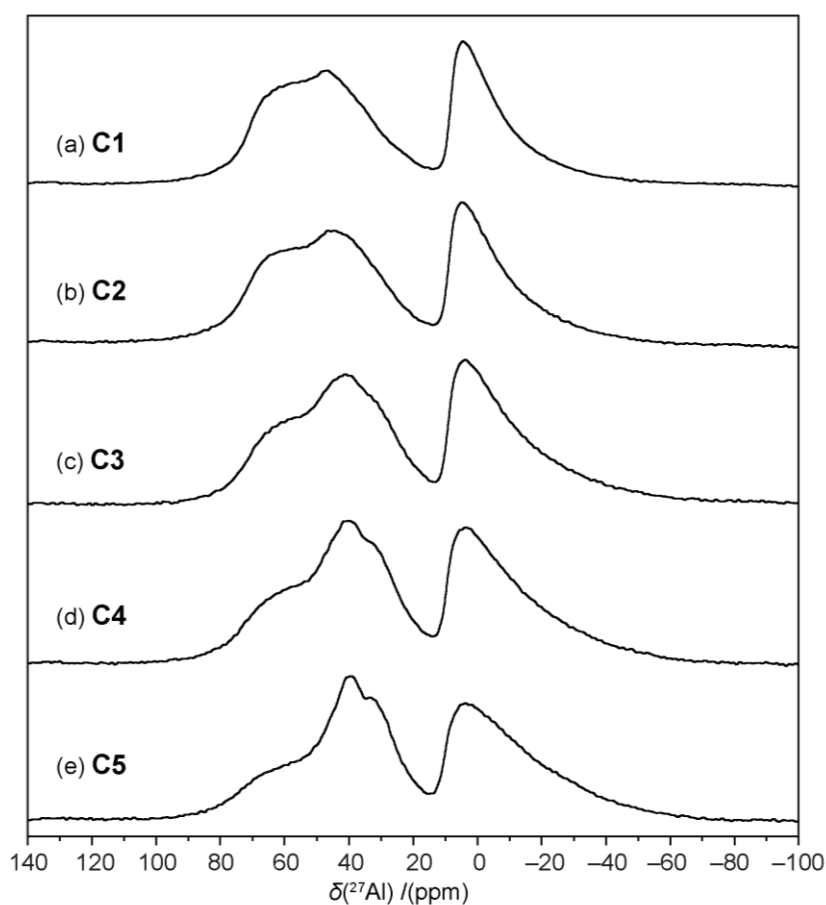
Figure 6.10 The ^{27}Al MAS (20 KHz) NMR spectra at 14.1 T of series C ($Al_{6-x}B_xO_9$): (a) C1, (b) C2, (c) C3, (d) C4 and (e) C5.
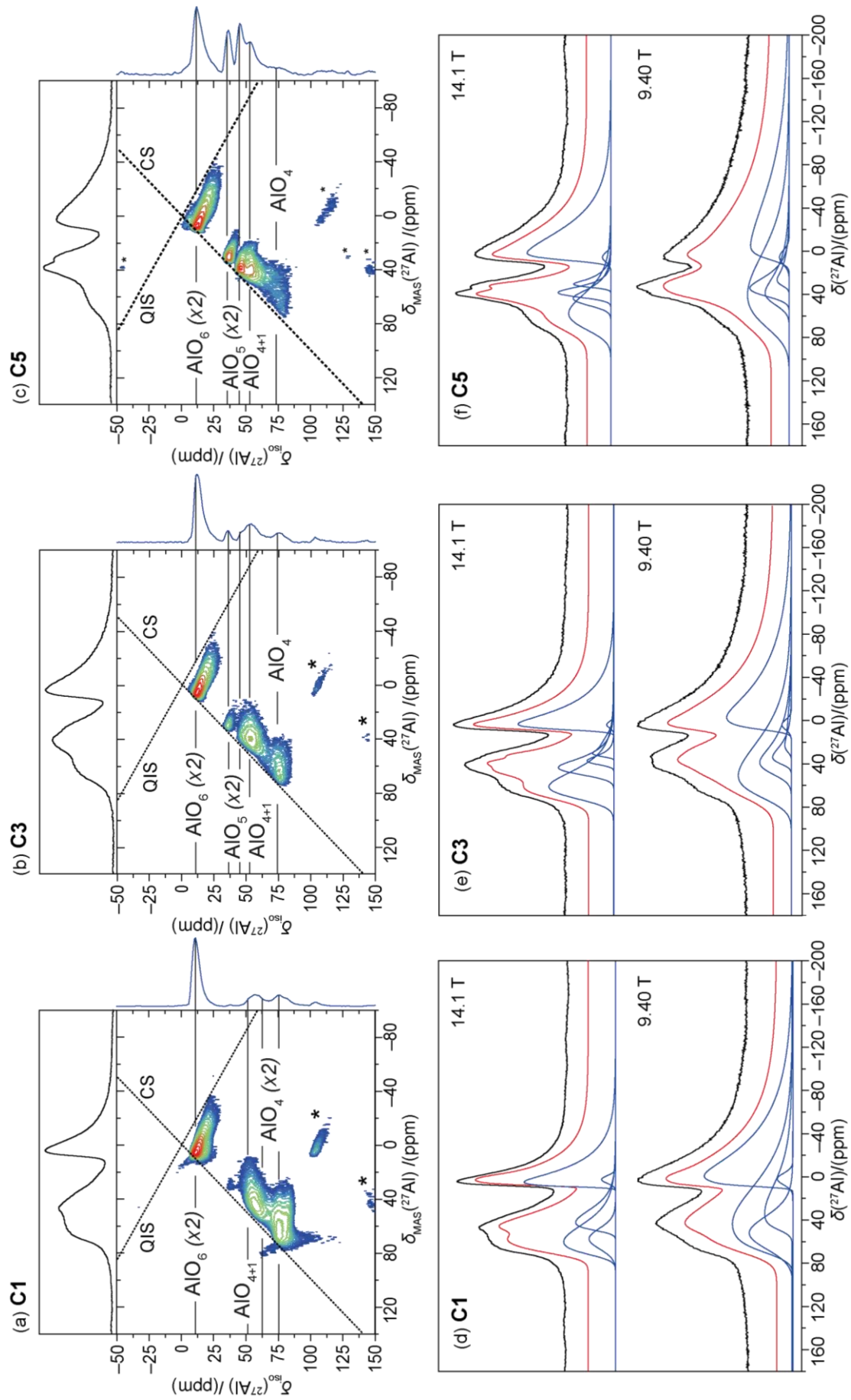
Figure 6.11 The ^{27}Al 2D 3QMAS (20 KHz) NMR spectra at 14.1 T of (a) C1, (b) C3 and (c) C5. The MAS spectrum is displayed above and the projected δ_{iso} spectrum on the right. Distinct resonances in the 2D spectrum are labelled with their assigned environments. The ^{27}Al MAS (20 KHz) NMR spectra at 14.1 T and 9.40 T for (d) C1, (e) C3 and (f) C5. The experimental spectra, the simulated lineshapes and the deconvoluted resonances are presented in black, red and blue, respectively.

Sample	δ_{iso} /(ppm) (± 1)	C_Q centre /(MHz) (± 0.1)	C_Q width /(MHz) (± 0.1)	η_Q (± 0.01)	Δ /(KHz) (± 0.1)	Species	Intensity /(%)	Species Int. /(%)
	2	0.0	0.0	0.0	1.3	AlO_6	2 ± 1	38 ± 2
	9	8.1	7.8	0.3	0.4	AlO_6	36 ± 1	
C1	50	6.8	4.7	1.0	1.1	AlO_{4+1}	17 ± 1	17 ± 1
	62	4.3	3.3	0.5	3.2	AlO_4	12 ± 1	45 ± 2
	73	8.0	5.0	1.0	1.8	AlO_4	33 ± 2	
	4	0.0	0.0	0.0	1.1	AlO_6	1 ± 1	41 ± 1
	9	8.6	8.0	0.3	0.7	AlO_6	41 ± 1	
C3	37	7.6	3.4	0.1	0.3	AlO_5	4 ± 1	24 ± 2
	41	4.7	3.3	0.5	0.9	AlO_5	5 ± 1	
	49	6.0	5.6	0.5	1.8	AlO_{4+1}	16 ± 2	
	72	7.3	5.2	1.0	2.5	AlO_4	35 ± 3	35 ± 3
	6	0.0	0.0	0.0	1.6	AlO_6	2 ± 1	43 ± 5
	9	9.9	8.2	0.5	1.0	AlO_6	41 ± 5	
C5	34	5.6	3.9	0.1	0.6	AlO_5	4 ± 1	25 ± 2
	42	4.7	3.4	0.5	1.2	AlO_5	10 ± 1	
	50	6.0	5.0	0.5	1.7	AlO_{4+1}	11 ± 1	
	74	8.4	5.0	1.0	3.3	AlO_4	32 ± 7	32 ± 7

Table 6.7 The ^{27}Al NMR parameters of series C ($Al_{6-x}B_xO_9$) determined via simulated fitting using a Gaussian distribution of C_Q.

127

Similarly to the A2B phase (Chapter 6.3), a quasi-tetrahedral AlO_{4+1} moiety is detected in the three series C compounds. Due to the observable similarities between the ^{27}Al MAS spectra of series C and aluminosilicate mullites (Figure 5.4), the presence of an AlO_{4+1} site is not surprising. The structural models proposed by Mazza *et al.* for $Al_{6-x}B_xO_9$ do not contain AlO_5 sites, and therefore may adequately describe the structure of sample C1.[144] However, the detection of two AlO_5 sites in the samples C3 and C5 via ^{27}Al NMR, alongside the results of the ^{11}B NMR investigation (Chapter 6.5.1), cast severe doubts on the veracity of these models. The detection of AlO_5 sites is assured, due to their presence in the structures of both stable aluminoborate phases and Mackenzie *et al.*'s corroborative ^{27}Al NMR results.[145]

The observed increase in the number of distinct AlO_5 sites, and with it the increase in relative AlO_5 site occupancy (Table 6.7), is a function of increasing initial B content which mirrors the concomitant increase in relative BO_4 site occupancy. Furthermore, the observed disorder in the more populated AlO_6 site also increases with increasing initial B content. These observations are compatible with an AlO_4/BO_4 solid solution, where the smaller BO_4 units induce distortion to adjacent AlO_6 units and the increased disorder favours the formation of AlO_5 moieties.

6.6. Conclusions

This study has successfully improved upon the previous ^{11}B and ^{27}Al NMR studies of the three mullite-like aluminoborate phases: A9B2, A2B and metastable $Al_{6-x}B_xO_9$. The thorough ^{27}Al NMR investigation of the three phases used 3QMAS and multi-field MAS NMR experiments, which allowed accurate assignment of the Al speciation. For the A9B2 phase, the accurate ^{27}Al NMR data detected a variety of differences in the structure of commercially, solid state and sol-gel synthesized materials. The ^{27}Al NMR results (using the knowledge gained from the mullite study in Chapter 5) discovered the quasi-tetrahedral AlO_{4+1} moiety in both the A2B and $Al_{6-x}B_xO_9$ structures, correcting the previous assignments in the literature. The improved ^{27}Al assignments in the $Al_{6-x}B_xO_9$ phase also disproved the existing structural model by confirming the presence of five-coordinate Al sites.

By studying a series of each phase with varying initial B contents this study has improved the understanding of the crystal structures. The ^{11}B NMR results determined a solid solution of tetrahedral Al and B in each series. In the A9B2 phase the narrow solid solution explained the disagreement between $Al_{18}B_4O_{33}$ and Al_5BO_9 compositions reported in the literature.

Additionally, the discovered substitution of BO_4 for AlO_4 units in the A2B phase justified the literature structural models with the NMR results.

Overall, the study has shown the utility of quadrupolar solid state NMR for structural determination. It is hoped that the improved understanding of the structures may aid in the application of these materials, especially in catalysis where small structural changes can result in large differences in function.

7
Summary

Despite the relatively disparate areas of research covered by this thesis, there is a common theme carried throughout. Namely, the structural determination of materials related to catalysis and containing local disorder, through investigation by quadrupolar solid state NMR. Each chapter approached this task with different methodologies, while investigating a diverse selection of catalytic materials.

Before an investigation into palladium catalyst materials with ^{105}Pd solid state NMR could take place in Chapter 4, the previously unexplored technique required fundamental development. This was achieved with the proposal of a standard chemical shift reference (0.33 M $H_2PdCl_{6(aq)}$) and the inaugural study of three Pd complexes (K_2PdCl_6, $(NH_4)_2PdCl_6$ and K_2PdBr_6) with direct observation ^{105}Pd solid state NMR. What began as a routine initial study into the chemical shift range instead became a key part of the research, as ^{105}Pd solid state NMR was found to be sensitive to minute structural deviations from the nominal cubic structure of the complexes. The study of Pd metal particles provided more evidence for this sensitivity, where it was shown that ^{105}Pd solid state NMR could detect defects in the metal structure and classify Pd metal nanoparticle sizes. Once these developmental studies were complete, ^{105}Pd NMR was applied to the more catalytical relevant doped Pd metal systems. At this point the limitations of ^{105}Pd solid state NMR were brought to light. In more disordered systems, the previously lauded sensitivity, in the form of both quadrupolar and Knight shift interactions, became its downfall, as the NMR resonances were often broadened beyond detection. Regardless, the study of the catalysts with ^{105}Pd solid state NMR alongside multi-nuclear solid state NMR, XRD and magnetic susceptibility measurements provided valuable structural information, specifically the interstitial location of the dopant.

The feasibility of a novel methodology for structural determination in disordered systems was explored in Chapter 5. The recently developed structure-generation program *supercell* was combined with GIPAW-DFT calculations and solid state NMR to probe the structure of the aluminosilicate, mullite. Mullite was chosen for this study due to its disordered structure, which had not yet been completely solved, and its relevance to catalysis. This methodology proved successful on 3:2 mullite, as the *supercell* led simulations allowed complete assignment of the ^{17}O, ^{27}Al and ^{29}Si solid state NMR spectra. Hence, the remaining questions

concerning mullite's structure could be answered. The application of this methodology to other mullite phases, was only limited by the synthetic challenges of making stochiometric samples.

Three mullite-like aluminoborate phases (A9B2, A2B and metastable $Al_{6-x}B_xO_9$) were investigated in Chapter 6, instead utilising the tried-and-tested method of solid state NMR in conjunction with (previously reported) diffraction results for structural determination. The ^{11}B and ^{27}Al solid state NMR study of the disordered aluminoborate phases utilised MQMAS and multiple field measurements. The thoroughness of this study, alongside the information gleaned from the mullite investigation mentioned above, allowed complete assignment of the NMR spectra for each phase, which corrected previous erroneous reports. Each of the phases were also studied for changes under varying synthesis conditions, which verified additional structural features in the aluminoborates.

It is hoped that the discovered structural information contained in this thesis may lead to improved function of the related catalysts and that the developed methodologies can be applied to studies of other disordered systems.

8
Bibliography

1. Levitt, M. H., *Spin Dynamics: Basics of Nuclear Magnetic Resonance*. Wiley and Sons Ltd.: Chichester, 2008.
2. MacKenzie, K. J. D.; Smith, M. E., *Multinuclear Solid-state NMR of Inorganic Materials*. Elsevier Science Limited: 2002.
3. Duer, M. J., *Introduction to Solid-State NMR Spectroscopy*. Blackwell Publishing Ltd.: Oxford, 2004.
4. Harris, R. K.; Becker, E. D.; Cabral de Menezes, S. M.; Granger, P.; Hoffman, R. E.; Zilm, K. W., Further conventions for NMR shielding and chemical shifts (IUPAC Recommendations 2008). In *Pure and Applied Chemistry*, 2008; Vol. 80, p 59.
5. Massiot, D.; Fayon, F.; Capron, M.; King, I.; Le Calve, S.; Alonso, B.; Durand, J. O.; Bujoli, B.; Gan, Z. H.; Hoatson, G., Modelling one- and two-dimensional solid-state NMR spectra. *Magnetic Resonance in Chemistry* **2002,** *40* (1), 70-76.
6. Apperley, D. C.; Harris, R. K.; Hodgkinson, P., *Solid State NMR: Basic Principles and Practice*. Momentum Press: New York, 2012.
7. Man, P. P., *NMR of Quadrupolar Nuclei in Solid Materials*. Wiley: Chichester, 2012.
8. Bryce, D. L.; Wasylishen, R. E., *NMR of Quadrupolar Nuclei in Solid Materials*. Wiley: Chichester, 2012.
9. Knight, W. D.; Kobayashi, S.-I., Knight Shift. In *eMagRes*, John Wiley & Sons, Ltd: 2007.
10. Carter, G. C.; Bennett, L. H.; Kahan, D. J., *Metallic Shifts in NMR*. Pergamon Press: Oxford, 1977.
11. Kittel, C., *Introduction to Solid State Physics*. 8th ed.; Wiley: 2005.
12. van der Klink, J. J.; Brom, H., *NMR in Metals, Metal Particles and Metal Cluster Compounds*. 2000; Vol. 36, p 89–201.
13. Kemp, T. F.; Smith, M. E., QuadFit—A new cross-platform computer program for simulation of NMR line shapes from solids with distributions of interaction parameters. *Solid State Nuclear Magnetic Resonance* **2009,** *35* (4), 243-252.
14. Kentgens, A. P. M., A practical guide to solid-state NMR of half-integer quadrupolar nuclei with some applications to disordered systems. *Geoderma* **1997,** *80* (3), 271-306.
15. Keeler, J., *Understanding NMR Spectroscopy*. 2 ed.; John Wiley & Sons, Ltd: Chichester, 2010.
16. Kentgens, A. P. M., *Quadrupolar Nutation Spectroscopy*. John Wiley and Sons Ltd.: Chichester, 2012.
17. Freude, D.; Haase, J., Quadrupole Effects in Solid-State Nuclear Magnetic Resonance. In *Special Applications*, Pfeifer, H.; Barker, P., Eds. Springer Berlin Heidelberg: Berlin, Heidelberg, 1993; pp 1-90.
18. Freude, D., Quadrupolar Nuclei in Solid-State Nuclear Magnetic Resonance. In *Encyclopedia of Analytical Chemistry*, John Wiley & Sons, Ltd: 2006.
19. Lippmaa, E.; Samoson, A.; Magi, M., High-resolution aluminum-27 NMR of aluminosilicates. *Journal of the American Chemical Society* **1986,** *108* (8), 1730-1735.
20. Yesinowski, J. P., Finding the true spin-lattice relaxation time for half-integral nuclei with non-zero quadrupole couplings. *J Magn Reson* **2015,** *252*, 135-44.
21. Narayanan, A.; Hartman, J. S.; Bain, A. D., Characterizing Nonexponential Spin-Lattice Relaxation in Solid-State NMR by Fitting to the Stretched Exponential. *Journal of Magnetic Resonance, Series A* **1995,** *112* (1), 58-65.

22. Bruker - Products - Magnetic Resonance - NMR. https://www.bruker.com/products/mr/nmr.html (accessed 09/2017).

23. Eroglu, S.; Gimi, B.; Roman, B.; Friedman, G.; Magin, R. L., NMR spiral surface microcoils: Design, fabrication, and imaging. *Concepts in Magnetic Resonance Part B: Magnetic Resonance Engineering* **2003,** *17B* (1), 1-10.

24. Man, P., *Numerical Analysis of Hahn Echoes in Solids*. 1995; Vol. 52, p 9418-9426.

25. MacKenzie, K. J. D.; Smith, M. E., *Multinuclear Solid State NMR of Inorganic Materials*. Pergamon Press: Oxford, 2002.

26. Frydman, L.; Harwood, J. S., Isotropic Spectra of Half-Integer Quadrupolar Spins from Bidimensional Magic-Angle Spinning NMR. *Journal of the American Chemical Society* **1995,** *117* (19), 5367-5368.

27. Schurko, R. W., Acquisition of Wideline Solid-State NMR Spectra of Quadrupolar Nuclei. In *eMagRes*, John Wiley & Sons, Ltd: 2007.

28. Egami, T.; Billinge, S., *Underneath the Bragg Peaks: Structural Analysis of Complex Materials*. Elsevier Science: Amsterdam, 2003.

29. McElfesh, M., *Fundamentals of Magnetism and Magnetic Measurements* Quantum Design: San Diego, 1994.

30. Jollie, D., *Platinum 2007*. Johnson Matthey: 2007.

31. Lox, E. S. J.; Engler, B. H., Environmental Catalysis — Mobile Sources. In *Environmental Catalysis*, Wiley-VCH Verlag GmbH: 2008; pp 1-117.

32. Ĉerveny, L., Palladium Catalysts in Hydrogentaion Reactions. *Chemical Engineering Communications* **1989,** *83* (1), 31-63.

33. Yin, L.; Liebscher, J., Carbon–Carbon Coupling Reactions Catalyzed by Heterogeneous Palladium Catalysts. *Chemical Reviews* **2007,** *107* (1), 133-173.

34. Luczak, F. J.; Sarangapani, S., Electrocatalysis of Fuel Cell Reactions. In *Fuel Cells: From Fundamentals to Applications*, Springer US: Boston, MA, 2006; pp 235-266.

35. Harris, R. K.; Becker, E. D.; Cabral de Menezes, S. M.; Goodfellow, R.; Granger, P., NMR nomenclature: nuclear spin properties and conventions for chemical shifts. IUPAC Recommendations 2001. International Union of Pure and Applied Chemistry. Physical Chemistry Division. Commission on Molecular Structure and Spectroscopy. *Magnetic Resonance in Chemistry* **2002,** *40* (7), 489-505.

36. Seitchik, J. A.; Gossard, A. C.; Jaccarino, V., Knight Shifts and Susceptibilities of Transition Metals: Palladium. *Physical Review* **1964,** *136* (4A), A1119-A1125.

37. Narath, A.; Fromhold, A. T.; Jones, E. D., Nuclear Spin Relaxation in Metals: Rhodium, Palladium, and Silver. *Physical Review* **1966,** *144* (2), 428-435.

38. Takigawa, M.; Yasukoa, H., Nuclear Magnetic Relaxation in Palladium. *Journal of the Physical Society of Japan* **1982,** *51* (3), 787-793.

39. Brill, P.; Voitländer, J., Palladium and Proton Knight Shift in Palladium Hydride. *Berichte der Bunsengesellschaft für physikalische Chemie* **1973,** *77* (12), 1097-1103.

40. Fedotov, M. A.; Likholobov, V. A., First direct observation of105Pd NMR in solution. *Bulletin of the Academy of Sciences of the USSR, Division of chemical science* **1984,** *33* (8), 1751-1751.

41. Brevard, C.; Granger, P., *Handbook of High Resolution Multinuclear NMR*. Wiley: 1981.

42. Matsuda, K.; Kohori, Y.; Kohara, T., Observation of 105Pd NMR and NQR signals in the heavy-fermion superconductor UPd2Al3. *Physical Review B* **1997,** *55* (22), 15223-15227.

43. Ruegger, H., Indirect coupling to quadrupolar nuclei: observation of 1J(105Pd,31P) in one- and two-dimensional 31P CP/MAS spectra. *Magn Reson Chem* **2004,** *42* (9), 814-8.

44. Beamish, F. E.; van Loon, J. C., *Recent advances in the analytical chemistry of the noble metals* Pergamon Press: Oxford, New York, 1972.

45. Vega, A. J., *NMR of Quadrupolar Nuclei in Solid Materials*. Wiley: Chichester, 2012.

46. Moudrakovski, I. L.; Ripmeester, J. A., 39K NMR of Solid Potassium Salts at 21 T: Effect of Quadrupolar and Chemical Shift Tensors. *The Journal of Physical Chemistry B* **2007,** *111* (3), 491-495.

47. Hayashi, S.; Hayamizu, K., Accurate Determination of NMR Chemical Shifts in Alkali Halides and Their Correlation with Structural Factors. *Bulletin of the Chemical Society of Japan* **1990,** *63* (3), 913-919.

48. Butler, A.; Eckert, H., Vanadium-51 NMR as a probe of vanadium(V) coorination to human apotransferrin. *Journal of the American Chemical Society* **1989,** *111* (8), 2802-2809.

49. Massiot, D.; Fayon, F.; Capron, M.; King, I.; Le Calvé, S.; Alonso, B.; Durand, J.-O.; Bujoli, B.; Gan, Z.; Hoatson, G., Modelling one- and two-dimensional solid-state NMR spectra. *Magnetic Resonance in Chemistry* **2002,** *40* (1), 70-76.

50. Matula, R. A., Electrical Resistivity of Copper, Gold, Palladium, and Silver. *Journal of Physical and Chemical Reference Data* **1979,** *5* (4), 1147-1298.

51. Albert, H. J.; Rubin, L. R., Magnetic Properties of the Platinum Metals and Their Alloys. In *Platinum Group Metals and Compounds*, AMERICAN CHEMICAL SOCIETY: 1971; Vol. 98, pp 1-16.

52. Clark Stewart, J.; Segall Matthew, D.; Pickard Chris, J.; Hasnip Phil, J.; Probert Matt, I. J.; Refson, K.; Payne Mike, C., First principles methods using CASTEP. In *Zeitschrift für Kristallographie - Crystalline Materials*, 2005; Vol. 220, p 567.

53. Pickard, C. J.; Mauri, F., All-electron magnetic response with pseudopotentials: NMR chemical shifts. *Physical Review B* **2001,** *63* (24), 245101.

54. Basham, M.; Filik, J.; Wharmby, M. T.; Chang, P. C. Y.; El Kassaby, B.; Gerring, M.; Aishima, J.; Levik, K.; Pulford, B. C. A.; Sikharulidze, I.; Sneddon, D.; Webber, M.; Dhesi, S. S.; Maccherozzi, F.; Svensson, O.; Brockhauser, S.; Naray, G.; Ashton, A. W., Data Analysis WorkbeNch (DAWN). *Journal of Synchrotron Radiation* **2015,** *22* (3), 853-858.

55. Soper, A. K.; Barney, E. R., Extracting the pair distribution function from white-beam X-ray total scattering data. *Journal of Applied Crystallography* **2011,** *44* (4), 714-726.

56. Coelho, A. A.; Chater, P. A.; Kern, A., Fast synthesis and refinement of the atomic pair distribution function. *Journal of Applied Crystallography* **2015,** *48* (3), 869-875.

57. Heslop, R. B.; Jones, K., *Inorganic Chemistry: A Guide to Advanced Study*. Elsevier Science: Amsterdam, 1976.

58. Hanna, J. V.; Pike, K. J.; Charpentier, T.; Kemp, T. F.; Smith, M. E.; Lucier, B. E. G.; Schurko, R. W.; Cahill, L. S., A 93Nb Solid‐State NMR and Density Functional Theory Study of Four‐ and Six‐Coordinate Niobate Systems. *Chemistry - A European Journal* **2010,** *16* (10), 3222-3239.

59. Hoffmann, K.; Hooper, T. J. N.; Murshed, M. M.; Dolotko, O.; Révay, Z.; Senyshyn, A.; Schneider, H.; Hanna, J. V.; Gesing, T. M.; Fischer, R. X., Formation, stability and crystal structure of mullite-type Al6−xBxO9. *Journal of Solid State Chemistry* **2016,** *243*, 124-135.

60. Douglas, B.; Ho, S.-M., *Structure and Chemistry of Crystalline Solids* Springer-Verlag: New York, 2006.

61. Ketblaar, J. A. A.; van Walsem, J. F., Die Krystalstruktur des Ammonium-, Kalium-, Rubidium- und Cäsiumpalladiumhexa-chlorids und -Bromids. *Recueil des Travaux Chimiques des Pays-Bas* **1938,** *57* (9), 964-966.

62. Frye, J. S.; Maciel, G. E., Setting the magic angle using a quadrupolar nuclide. *Journal of Magnetic Resonance (1969)* **1982,** *48* (1), 125-131.

63. Cookson, J., The Preparation of Palladium Nanoparticles. *Platinum Metals Review* **2012,** *56* (2), 83-98.

64. Sheldon, R. A.; van Bekkum, H., Catalytic Hydrogenation and Dehydrogenation. In *Fine Chemicals through Heterogeneous Catalysis*, Wiley-VCH Verlag GmbH: 2007; pp 351-471.

65. Zelinsky, N.; Glinka, N., Über gleichzeitige Reduktions- und Oxydationskatalyse. *Berichte der deutschen chemischen Gesellschaft* **1911,** *44* (3), 2305-2311.

66. Ellis, I. T. Interstitial Modification of Palladium for Partial Hydrogenation Reactions. Univeristy of Oxford, Oxford, 2016.

67. Burger, J. P.; Senoussi, S.; Soufache, B., Electrical and magnetic properties of palladium hydrides compared with those of pure palladium. *Journal of Less Common Metals* **1976,** *49*, 213-222.

68. Sanger, W.; Voitlander, J., On the Temperature Dependence of the Magnetic Susceptibility of Enhanced Paramagnetic Metals: Pure Palladium. *Z. Physik B* **1978,** *30*, 13-18.

69. Rees, G. J.; Orr, S. T.; Barrett, L. O.; Fisher, J. M.; Houghton, J.; Spikes, G. H.; Theobald, B. R.; Thompsett, D.; Smith, M. E.; Hanna, J. V., Characterisation of platinum-based fuel cell catalyst materials using 195Pt wideline solid state NMR. *Phys Chem Chem Phys* **2013,** *15* (40), 17195-207.

70. Graham, T., On the Absorption and Dialytic Separation of Gases by Colloid Septa. *Philosophical Transactions of the Royal Society of London* **1866,** *156*, 399-439.

71. Lewis, F. A., The Hydrides of Palladium and Palladium Alloys. *Platinum Metals Review* **1960,** *4* (4).

72. T B Flanagan, a.; Oates, W. A., The Palladium-Hydrogen System. *Annual Review of Materials Science* **1991,** *21* (1), 269-304.

73. Adams, B. D.; Chen, A., The role of palladium in a hydrogen economy. *Materials Today* **2011,** *14* (6), 282-289.

74. Gillespie, L. J.; Hall, F. P., The palladium-hydrogen equilibrium and palladium hydride. *Journal of the American Chemical Society* **1926,** *48* (5), 1207-1219.

75. Tripodi, P.; Armanet, N.; Asarisi, V.; Avveduto, A.; Marmigi, A.; Vinko, J. D.; Biberian, J.-P., The effect of hydrogenation/dehydrogenation cycles on palladium physical properties. *Physics Letters A* **2009,** *373* (35), 3101-3108.

76. Lewis, F. A., The Palladium-Hydrogen System II. *Platinum Metals Review* **1982,** *26* (2), 70-78.

77. Duggan, B.; Farr, J. P. G.; Kushner, J. B.; Wise, M., Effects of Hydrogen Absorption in Palladium and Palladium-24% Silver Foils. *Nature Physical Science* **1972,** *236* (66), 73-74.

78. Sakaki, K.; Yamada, T.; Mizuno, M.; Araki, H.; Shirai, Y., Hydrogen-Induced Vacancy Generation Phenomenon in Pure Pd. *Materials Transactions* **2002,** *43* (11).

79. Fulmer, G. R.; Miller, A. J. M.; Sherden, N. H.; Gottlieb, H. E.; Nudelman, A.; Stoltz, B. M.; Bercaw, J. E.; Goldberg, K. I., NMR Chemical Shifts of Trace Impurities: Common Laboratory Solvents, Organics, and Gases in Deuterated Solvents Relevant to the Organometallic Chemist. *Organometallics* **2010,** *29* (9), 2176-2179.

80. Hara, M.; Sakurai, J.; Akamaru, S.; Watanabe, K.; Nishimura, K.; Mori, K.; Matsuyama, M., Magnetic Properties of Palladium and Palladium–Platinum Alloy of Various Hydrogen Content. *Materials Transactions* **2006,** *47* (9), 2373-2376.

81. Jamieson, H. C.; Manchester, F. D., The magnetic susceptibility of Pd, PdH and PdD between 4 and 300 K. *J. Phys. F: Metal Phys.* **1972,** *323-336*.

82. Armbrüster, M.; Behrens, M.; Cinquini, F.; Föttinger, K.; Grin, Y.; Haghofer, A.; Klötzer, B.; Knop‐Gericke, A.; Lorenz, H.; Ota, A.; Penner, S.; Prinz, J.; Rameshan, C.; Révay, Z.; Rosenthal, D.; Rupprechter, G.; Sautet, P.; Schlögl, R.; Shao, L.; Szentmiklósi, L.; Teschner, D.; Torres, D.; Wagner, R.; Widmer, R.; Wowsnick, G., How to Control the Selectivity of Palladium‐based Catalysts in Hydrogenation Reactions: The Role of Subsurface Chemistry. *ChemCatChem* **2012,** *4* (8), 1048-1063.

83. Jones, S.; Fairclough, S. M.; Gordon-Brown, M.; Zheng, W.; Kolpin, A.; Pang, B.; Kuo, W. C. H.; Smith, J. M.; Tsang, S. C. E., Dual doping effects (site blockage and electronic promotion) imposed by adatoms on Pd nanocrystals for catalytic hydrogen production. *Chemical Communications* **2015,** *51* (1), 46-49.

84. Ziemecki, S. B., Ternary system palladium-carbon-hydrogen. *Reactivity of Solids* **1986,** *1* (2), 195-198.

85. Chan, C. W. A.; Tam, K. Y.; Cookson, J.; Bishop, P.; Tsang, S. C., Palladium with interstitial carbon atoms as a catalyst for ultraselective hydrogenation in the liquid phase. *Catalysis Science & Technology* **2011,** *1* (9), 1584-1592.

86. Bakker, H. L. M.; Jong, M. J. C. d.; Oppeneer, P. M.; Griessen, R.; Lodder, A.; Vis, R.; Brodowsky, H., Interstitial carbon in palladium: Fermi surface and electron scattering. *Journal of Physics F: Metal Physics* **1986,** *16* (6), 707.

87. Chan, C. W. A.; Xie, Y.; Cailuo, N.; Yu, K. M. K.; Cookson, J.; Bishop, P.; Tsang, S. C., New environmentally friendly catalysts containing Pd-interstitial carbon made from Pd-glucose precursors for ultraselective hydrogenations in the liquid phase. *Chemical Communications* **2011,** *47* (28), 7971-7973.

88. Seriani, N.; Mittendorfer, F.; Kresse, G., Carbon in palladium catalysts: A metastable carbide. *The Journal of Chemical Physics* **2010,** *132* (2), 024711.

89. Ellner, M.; Beck, M.; Mittemeijer, E. J., The structure of the palladium-rich boride Pd5B (Pd16B3). In *Zeitschrift für Kristallographie/International journal for structural, physical, and chemical aspects of crystalline materials*, 2001; Vol. 216, p 591.

90. Kobayashi, K.; Kobayashi, H.; Maesato, M.; Hayashi, M.; Yamamoto, T.; Yoshioka, S.; Matsumura, S.; Sugiyama, T.; Kawaguchi, S.; Kubota, Y.; Nakanishi, H.; Kitagawa, H., Discovery of Hexagonal Structured Pd–B Nanocrystals. *Angewandte Chemie International Edition* **2017,** *56* (23), 6578-6582.

91. Chan, C. W. A.; Mahadi, A. H.; Li, M. M.-J.; Corbos, E. C.; Tang, C.; Jones, G.; Kuo, W. C. H.; Cookson, J.; Brown, C. M.; Bishop, P. T.; Tsang, S. C. E., Interstitial modification of palladium nanoparticles with boron atoms as a green catalyst for selective hydrogenation. *Nature Communications* **2014,** *5*, 5787.

92. Wang, J.-Y.; Kang, Y.-Y.; Yang, H.; Cai, W.-B., Boron-Doped Palladium Nanoparticles on Carbon Black as a Superior Catalyst for Formic Acid Electro-oxidation. *The Journal of Physical Chemistry C* **2009,** *113* (19), 8366-8372.

93. Ellis, I. T.; Wolf, E. H.; Jones, G.; Lo, B.; Meng-Jung Li, M.; York, A. P. E.; Edman Tsang, S. C., Lithium and boron as interstitial palladium dopants for catalytic partial hydrogenation of acetylene. *Chemical Communications* **2017,** *53* (3), 601-604.

94. van der Klink, J. J.; Brom, H. B., NMR in metals, metal particles and metal cluster compounds. *Progress in Nuclear Magnetic Resonance Spectroscopy* **2000,** *36* (2), 89-201.

95. Pavarini, E.; Baek, S. H.; Suh, B. J.; Borsa, F.; Bud'ko, S. L.; Canfield, P. C., NMR relaxation rates and Knight shifts in MgB 2 and AlB 2 : theory versus experiments. *Superconductor Science and Technology* **2003,** *16* (2), 147.

96. Schneider, H.; Komarneni, S., *Mullite*. Wiley-VCH ; Chichester : John Wiley [distributor]: Weinheim, 2005; p xxii, 487 p.

97. Fischer, R. X.; Kahlenberg, V.; Voll, D.; MacKenzie, K. J. D.; Smith, M. E.; Schnetger, B.; Brumsack, H. J.; Schneider, H., Crystal structure of synthetic Al4B2O9: A member of the mullite family closely related to boralsilite. *American Mineralogist* **2008,** *93* (5-6), 918-927.

98. Zhao, X.; Cong, Y.; Lv, F.; Li, L.; Wang, X.; Zhang, T., Mullite-supported Rh catalyst: a promising catalyst for the decomposition of N2O propellant. *Chemical Communications* **2010,** *46* (17), 3028-3030.

99. Bing-Xiong, L.; Wan-Jing, Z.; Qing-Xin, Y.; Zuo-Hua, P.; Lin-Lin, G.; You-Chi, T., The Significance Of The Mullite Phase In A Silver Catalyst For The Oxidation Of Ethylene Into Ethylene Oxide. *Studies in Surface Science and Catalysis* **1983,** *16*, 563-569.

100. Liguras, D. K.; Goundani, K.; Verykios, X. E., Production of hydrogen for fuel cells by catalytic partial oxidation of ethanol over structured Ni catalysts. *Journal of Power Sources* **2004,** *130* (1), 30-37.

101. Schimmoeller, B.; Schulz, H.; Pratsinis, S. E.; Bareiss, A.; Reitzmann, A.; Kraushaar-Czarnetzki, B., Ceramic foams directly-coated with flame-made V2O5/TiO2 for synthesis of phthalic anhydride. *Journal of Catalysis* **2006,** *243* (1), 82-92.

102. de Lathouder, K. M.; Bakker, J.; Kreutzer, M. T.; Kapteijn, F.; Moulijn, J. A.; Wallin, S. A., Structured reactors for enzyme immobilization: advantages of tuning the wall morphology. *Chemical Engineering Science* **2004,** *59* (22), 5027-5033.

103. Wang, W.; McCool, G.; Kapur, N.; Yuan, G.; Shan, B.; Nguyen, M.; Graham, U. M.; Davis, B. H.; Jacobs, G.; Cho, K.; Hao, X., Mixed-Phase Oxide Catalyst Based on Mn-Mullite (Sm, Gd)Mn$_2$O$_5$ for NO Oxidation in Diesel Exhaust. *Science* **2012,** *337* (6096), 832-835.

104. Burnham Charles, W., Refinement of the crystal structure of sillimanite. In *Zeitschrift für Kristallographie - Crystalline Materials*, 1963; Vol. 118, p 127.

105. Angel, R. J.; McMullan, R. K.; Prewitt, C. T., Substructure and superstructure of mullite by neutron-diffraction. *American Mineralogist* **1991,** *76* (3-4), 332-342.

106. Luhrs, H. The Influence of Boron on the Crystal Structure and Properties of Mullite. Universitat Bremen, Bremen 2013.

107. Loewenstein, W., The Distribution of Aluiminum in the Tetrahedra of Silicates and Aluminates. *American Mineralogist* **1954,** *39*, 92-96.

108. Schneider, H.; Schreuer, J.; Hildmann, B., Structure and properties of mullite - A review. *Journal of the European Ceramic Society* **2008,** *28* (2), 329-344.

109. Fischer, R. X.; Schneider, H.; Voll, D., Formation of aluminum rich 9:1 mullite and its transformation to low alumina mullite upon heating. *Journal of the European Ceramic Society* **1996,** *16* (2), 109-113.

110. Ban, T.; Okada, K., Analysis of local cation arrangement in mullite using si-29 magic-angle-spinning nuclear-magnetic-resonance spectra. *Journal of the American Ceramic Society* **1993,** *76* (10), 2491-2496.

111. Jaymes, I.; Douy, A.; Massiot, D.; Coutures, J. P., Evolution of the Si environment in mullite solid solution by Si-29 MAS-NMR spectroscopy. *Journal of Non-Crystalline Solids* **1996,** *204* (2), 125-134.

112. Epicier, T.; Okeefe, M. A.; Thomas, G., ATOMIC IMAGING OF 3-2 MULLITE. *Acta Crystallographica Section A* **1990,** *46*, 948-962.

113. Freimann, S.; Rahman, S., Refinement of the real structures of 2:1 and 3:2 mullite. *Journal of the European Ceramic Society* **2001,** *21* (14), 2453-2461.

114. Bodart, P. R.; Parmentier, J.; Harris, R. K.; Thompson, D. P., Aluminium environments in mullite and an amorphous sol–gel precursor examined by 27Al triple-quantum MAS NMR. *Journal of Physics and Chemistry of Solids* **1999,** *60* (2), 223-228.

115. Jaymes, I.; Douy, A.; Massiot, D.; Coutures, J. P., Characterization of mono- and diphasic mullite precursor powders prepared by aqueous routes. Al-27 and Si-29 MAS-NMR spectroscopy investigations. *Journal of Materials Science* **1996,** *31* (17), 4581-4589.

116. Kunathfandrei, G.; Rehak, P.; Steuernagel, S.; Schneider, H.; Jager, C., Quantitative structural-analysis of mullite by al-27 nuclear-magnetic-resonance satellite transition spectroscopy. *Solid State Nuclear Magnetic Resonance* **1994,** *3* (5), 241-248.

117. Schmucker, M.; Schneider, H.; MacKenzie, K.; Smith, M.; Carroll, D., AlO4/SiO4 distribution in tetrahedral double chains of mullite. *Journal of the American Ceramic Society* **2005,** *88* (10), 2935-2937.

118. Paulmann, C., Study of oxygen vacancy ordering in mullite at high temperatures. *Phase Transitions* **1996,** *59* (1-3), 77-90.

119. Merwin, L. H.; Sebald, A.; Rager, H.; Schneider, H., Si-29 and Al-27 MAS NMR-spectroscopy of mullite. *Physics and Chemistry of Minerals* **1991,** *18* (1), 47-52.

120. King, S. P. Development of Solid State NMR on Disordered Systems, from Bioactive glasses to Mullites. University of Warwick, 2014.

121. Griesser, K. J.; Beran, A.; Voll, D.; Schneider, H., Boron incorporation into mullite. *Mineralogy and Petrology* **2008,** *92* (3-4), 309-320.

122. Zhang, G.; Fu, Z.; Wang, Y.; Wang, H.; Wang, W.; Zhang, J.; Lee, S. W.; Niihara, K., Boron-doped mullite derived from single-phase gels. *Journal of the European Ceramic Society* **2010,** *30* (12), 2435-2441.

123. Fischer, R. X.; Schneider, H., Crystal chemistry of borates and borosilicates with mullite-type structures: a review. *European Journal of Mineralogy* **2008,** *20* (5), 917-933.

124. Lührs, H.; Fischer, R. X.; Schneider, H., Boron mullite: Formation and basic characterization. *Materials Research Bulletin* **2012,** *47* (12), 4031-4042.

125. Lührs, H.; Senyshyn, A.; King Scott, P.; Hanna John, V.; Schneider, H.; Fischer Reinhard, X., Neutron diffraction and 11B solid state NMR studies of the crystal structure of B-doped mullite. In *Zeitschrift für Kristallographie - Crystalline Materials*, 2013; Vol. 228, p 457.

126. Lührs, H.; Soellradl, S.; King, S. P.; Hanna, J. V.; Konzett, J.; Fischer, R. X.; Schneider, H., Ambient and high-pressure synthesis, composition, and crystal structure of B-mullites. *Crystal Research and Technology* **2014,** *49* (1), 21-31.

127. Guse, W.; Mateika, D., Growth of mullite single crystals (2Al2O3 · SiO2) by the Czochralski method. *Journal of Crystal Growth* **1974,** *22* (3), 237-240.

128. Okhotnikov, K.; Charpentier, T.; Cadars, S., Supercell program: a combinatorial structure-generation approach for the local-level modeling of atomic substitutions and partial occupancies in crystals. *J Cheminform* **2016,** *8*, 17.

129. Balzar, D.; Ledbetter, H., Crystal structure and compressibility of 3:2 mullite. *American Mineralogist* **1993,** *78* (11-12), 1192-1196.

130. Kresse, G.; Joubert, D., From ultrasoft pseudopotentials to the projector augmented-wave method. *Physical Review B* **1999,** *59* (3), 1758-1775.

131. Kelsey, K. E.; Stebbins, J. F.; Du, L.-S.; Hankins, B., Constraining ^{17}O and ^{27}Al NMR spectra of high-pressure crystals and glasses: New data for jadeite, pyrope, grossular, and mullite. *American Mineralogist* **2007,** *92* (1), 210-216.

132. Medek, A.; Harwood, J. S.; Frydman, L., Multiple-Quantum Magic-Angle Spinning NMR: A New Method for the Study of Quadrupolar Nuclei in Solids. *Journal of the American Chemical Society* **1995,** *117* (51), 12779-12787.

133. Wu, G.; Rovnyak, D.; Griffin, R. G., Quantitative Multiple-Quantum Magic-Angle-Spinning NMR Spectroscopy of Quadrupolar Nuclei in Solids. *Journal of the American Chemical Society* **1996,** *118* (39), 9326-9332.

134. Werding, G.; Schreyer, W., Experimental studies on borosilicates and selected borates. *Reviews in Mineralogy and Geochemistry* **1996,** *33* (1), 117-163.

135. Gielisse, P. J. M.; Foster, W. R., The System Al2O3-B2O3. *Nature* **1962,** *195* (4836), 69-70.

136. Fisch, M.; Armbruster, T.; Rentsch, D.; Libowitzky, E.; Pettke, T., Crystal-chemistry of mullite-type aluminoborates Al18B4O33 and Al5BO9: A stoichiometry puzzle. *Journal of Solid State Chemistry* **2011,** *184* (1), 70-80.

137. Scholze, H., Über Aluminiumborate. *Zeitschrift für anorganische und allgemeine Chemie* **1956,** *284* (4-6), 272-277.

138. Hung, I.; Howes, A. P.; Anupõld, T.; Samoson, A.; Massiot, D.; Smith, M. E.; Brown, S. P.; Dupree, R., 27Al double rotation two-dimensional spin diffusion NMR: Complete unambiguous assignment of aluminium sites in 9Al2O3·2B2O3. *Chemical Physics Letters* **2006,** *432* (1-3), 152-156.

139. Gan, Z.; Gor'kov, P.; Cross, T. A.; Samoson, A.; Massiot, D., Seeking Higher Resolution and Sensitivity for NMR of Quadrupolar Nuclei at Ultrahigh Magnetic Fields. *Journal of the American Chemical Society* **2002,** *124* (20), 5634-5635.

140. Kunath, G.; Losso, P.; Steuernagel, S.; Schneider, H.; Jäger, C., 27Al satellite transition spectroscopy (SATRAS) of polycrystalline aluminium borate 9Al2O3 · 2B2O3. *Solid State Nuclear Magnetic Resonance* **1992,** *1* (5), 261-266.

141. Ihara, M.; Imai, K.; Fukunaga, J.; Yoshida, N., Crystal Structure of Boroaluminate, $9Al_2O_3 \cdot 2B_2O_3$. *Journal of the Ceramic Association, Japan* **1980,** *88* (1014), 77-84.

142. Sokolova, Y. V.; Azizov, A. V.; Simonov, M. A.; Leonyuk, N. I.; Belov, N. V., *Dokl. Akad. Nauk SSSR* **1978,** *243* (3), 655-658.

143. Garsche, M.; Tillmanns, E.; Almen, H.; Schneider, H.; Kupcik, V., Incorporation of chromium into aluminium borate $9Al_2O_3 . 2B_2O_3$ (A_9B_2). *European Journal of Mineralogy* **1991,** *3* (5), 793-808.

144. Mazza, D.; Vallino, M.; Busca, G., Mullite-Type Structures in the Systems Al2O3–Me2O (Me = Na, K) and Al2O3–B2O3. *Journal of the American Ceramic Society* **1992,** *75* (7), 1929-1934.

145. MacKenzie, K. J. D.; Smith, M. E.; Kemp, T. F.; Voll, D., Crystalline Aluminium Borates with the Mullite Structure: A 11B and 27Al Solid-State NMR Study. *Applied Magnetic Resonance* **2007,** *32* (4), 647-662.

146. Zhang, J.; Lin, J.; Song, H. S.; Elssfah, E. M.; Liu, S. J.; Luo, J. J.; Ding, X. X.; Tang, C.; Qi, S. R., Bulk-quantity fast production of Al4B2O9/Al18B4O33 single-crystal nanorods by a novel technique. *Materials Letters* **2006,** *60* (27), 3292-3295.

147. Hernández, M. F.; Suárez, G.; Cipollone, M.; Conconi, M. S.; Aglietti, E. F.; Rendtorff, N. M., Formation, microstructure and properties of aluminum borate ceramics obtained from alumina and boric acid. *Ceramics International* **2017,** *43* (2), 2188-2195.

148. Ray, S. P., Preparation and Characterization of Aluminum Borate. *Journal of the American Ceramic Society* **1992,** *75* (9), 2605-2609.

149. An, D.; Zhang, M.; Li, D.; Pan, S.; Chen, H.; Yang, Z.; Zhu, Y.; Sun, Y.; Zhang, H.; Li, Y., Linear and nonlinear optical properties of aluminum borate crystal Al5BO9: Experiment and calculation. *Journal of Materials Research* **2015,** *30* (15), 2319-2326.

150. Sueyoshi, H.; Eguchi, T.; Hayashi, C.; Nakamura, Y., Friction and Wear of Composite Materials Composed of Aluminum, Aluminum Borate Whisker and Solid Lubricant. *Journal of the Japan Society of Powder and Powder Metallurgy* **1994,** *41* (8), 939-944.

151. Hu, Z. S. S., Y.G.; Wang, L. G.; Peng, Y.; Chen, G. X.; Dong, J. X., Study on Antiwear and Reducing Friction Additive of Nanometer Aluminum Borate. *Lubrication Engineering* **2001,** *57* (3), 23-27.

152. Zhang, J.; Elsanousi, A.; Lin, J.; Huang, Y.; Elssfah, E. M.; Chen, D.; Gao, J.; Huang, Z.; Ding, X.; Tang, C., Aerosol-Assisted Self-Assembly of Aluminum Borate (Al18B4O33) Nanowires into Three Dimensional Hollow Spherical Architectures. *Crystal Growth & Design* **2007,** *7* (12), 2764-2767.

153. Wang, G.; Wang, K.; Hou, J.; Xu, Y., The Controllable Preparation of Aluminum Borate Nano-materials. *Advanced Materials Research* **2011,** *236-238*, 3056-3060.

154. Wang, Y.; Feng, J.; Wang, Z.; Song, X.; Cao, J., Joining of Al2O3 by epitaxial growth of aluminum borate whiskers for high-temperature applications. *Materials Letters* **2016,** *163*, 231-235.

155. Yoshida, M.; Takeuchi, S.; Pan, J.; Sasaki, G.; Fuyama, N.; Fuj, T.; Fukunaga, H., Preparation and characterization of aluminum borate whisker reinforced magnesium alloy composites by semi-solid process. *Advanced Composite Materials* **1999,** *8* (3), 259-268.

156. Liang, G.; Hu, X., Preparation and performance of aluminum borate whisker–reinforced epoxy composites. I. Effect of whiskers on processing, reactivity, and mechanical properties. *Journal of Applied Polymer Science* **2004,** *92* (3), 1950-1954.

157. Suganuma, K.; Fujita, T.; Sasaki, G.; Suzuki, N., Evaluation of strength and heat-resistance for aluminum-borate whisker reinforced AC8A aluminum alloy composite. *Journal of Japan Institute of Light Metals* **1991,** *41* (4), 270-275.

158. El-Hakam, S. A.; El-Sharkawy, E. A., Structural characterization and catalytic properties of aluminum borates–alumina catalysts. *Materials Letters* **1998,** *36* (1), 167-173.

159. Peil, K. P.; Galya, L. G.; Marcelin, G., Acid and catalytic properties of nonstoichiometric aluminum borates. *Journal of Catalysis* **1989,** *115* (2), 441-451.

160. Wang, W.-J.; Chen, Y.-W., Alumina-aluminum borates as solid acid catalysts. *Catalysis Letters* **1991,** *10* (3), 297-304.

161. Li, C.; Chen, Y. W.; Yang, S. J.; Wu, J. C., Hydrodesulfurization reactions of atmospheric gas oil over cobalt-molybdenum/alumina-aluminum borate catalysts. *Industrial & Engineering Chemistry Research* **1993,** *32* (8), 1573-1578.

162. Huang, T.-C.; Kang, B.-C., The thioresistance of platinum/aluminum borate catalysts in aromatic hydrogenation. *Journal of Molecular Catalysis A: Chemical* **1995,** *103* (3), 163-174.

163. Abbas-Ghaleb, R.; Garbowski, E.; Kaddouri, A.; Gelin, P., Al18B4O33 aluminium borate: A new efficient support for palladium in the high temperature catalytic combustion of methane. *Catalysis Today* **2006,** *117* (4), 514-517.

164. Hoffmann, K.; Hooper, T. J. N.; Zhao, H.; Kolb, U.; Murshed, M. M.; Fischer, M.; Lührs, H.; Nénert, G.; Kudějová, P.; Senyshyn, A.; Schneider, H.; Hanna, J. V.; Gesing, T. M.; Fischer, R. X., Crystal chemical characterization of mullite-type aluminum borate compounds. *Journal of Solid State Chemistry* **2017,** *247*, 173-187.

165. Narita, K.; Umeda, J. i.; Kusumoto, H., Nuclear Magnetic Resonance Powder Patterns of the Second‐Order Nuclear Quadrupole Interaction in Solids with Asymmetric Field Gradient. *The Journal of Chemical Physics* **1966,** *44* (7), 2719-2723.

166. Massiot, D.; Müller, D.; Hübert, T.; Schneider, M.; Kentgens, A. P. M.; Coté, B.; Coutures, J. P.; Gessner, W., Double rotation and magic-angle spinning nuclear magnetic resonance study of 27Al: reexamination of the aluminium borate 9Al2O3 · 2B2O3. *Solid State Nuclear Magnetic Resonance* **1995,** *5* (2), 175-180.